

**HIGH DOSE-RATE BRACHYTHERAPY OPTIMIZATION FOR BREAST CANCER
USING DIFFUSION THEORY**

by

Jason Michael Holzmann

A thesis submitted in partial fulfillment of
the requirements for the degree of

Master of Science

(Nuclear Engineering & Engineering Physics)

at the

UNIVERSITY OF WISCONSIN-MADISON

14 August 2010

© Copyright by Jason Michael Holzmann 14 August 2010

All Rights Reserved

To music, my family, and friends

ACKNOWLEDGMENTS

Thank you to my advisor Professor Douglass L. Henderson along with Professor Bruce Thomadsen both whom greatly supported my research efforts and taught me a great deal of concepts pertaining to radiotherapy. Thanks to the department of Nuclear Engineering & Engineering Physics and to the Department Chair, Professor Michael Corradini, for allowing me to pursue my Master's degree.

I would also like to thank my family for moral and financial support. I would especially like to thank my soulmate Naomi Thoman for her kind heart and sound advice for the last six years and many more to come. Thanks to the National Academy for Nuclear Training (NANT) for granting me their fellowship for graduate school. Because of the fellowship, I required less student loans and now have less debt to pay back. I would also like to thank the James P. Elko Memorial Scholarship for aiding in my undergraduate tuition.

Finally, I am thankful for all of the teachers and professors who have helped me throughout my high school and college education. My high school physics teacher was actually the first to point me in the direction of nuclear engineering. After I was accepted at UW-Madison, I looked further into the nuclear engineering curriculum and decided to give it a try. The rest is history. I was accepted into the department, then the dual-degree program, and with the completion of this thesis I am prepared to graduate.

I want to thank TomoTherapy for deciding to hire me into my first professional position as a physicist support specialist. When I first began taking courses in the department of Medical Physics, I learned of the company started by the UW alum and professor, Thomas Rockwell Mackie. After learning more about their innovative technique for external beam radiotherapy, I

became very interested and set a goal of beginning my professional career with TomoTherapy. After a great deal of hard work in courses and research, I was able to accomplish this goal.

DISCARD THIS PAGE

TABLE OF CONTENTS

	Page
LIST OF TABLES	vi
LIST OF FIGURES	vii
ABSTRACT	x
1 Introduction to Brachytherapy	1
1.1 Motivation	2
1.2 Problem Definition	2
2 Multi-Catheter HDRBT Procedure	4
2.1 Preoperative Procedure	4
2.2 Varification of Set-up and Dose	6
2.3 The ^{192}Ir Source	6
3 The Diffusion Approximation and Green's Function for Dose	9
3.1 Green's Function Solution	10
3.1.1 Boundary Conditions on the Helmholtz Equation	11
3.2 Charged Particle Equilibrium	12
3.3 Calculation of the Diffusion Coefficient	13
4 The Two-Dimensional Green's Function Solution	15
4.1 2-D Dirichlet Boundary Condition	15
4.1.1 2-D Dirichlet Green's Function	17
4.1.2 Dose Distribuion for 2-D Dirichlet Solution	23
4.2 2-D Neumann Boundary Condition	25
4.2.1 2-D Neumann Green's Function	26
4.2.2 Dose Distribution for the 2-D Neumann Solution	28
4.3 2-D Robin (Current Density) Boundary Condition	28

	Page
4.3.1 2-D Current Density Green's Function	30
4.3.2 Dose Distribution for the 2-D Current Density Condition	32
4.4 Concluding Remarks on the 2-D Green's Function	32
5 Two-Dimensional Dose Optimization	35
5.1 Optimization Modeling using GAMS	35
5.1.1 MATLAB / GAMS Interface	36
5.1.2 GAMS Data Exchange	36
5.1.3 Linear Programming in GAMS	36
5.1.4 The Simplex Method	37
5.2 2-D Dose Optimization for the Current Density Condition: Centered PTV	37
5.2.1 Geometry Definition: Centered PTV	38
5.2.2 Unoptimized Dose	39
5.2.3 A Note on Optimization Routine Duration	41
5.2.4 Linear Program #1	42
5.2.5 Linear Program #2	45
5.2.6 Linear Program #3	48
5.2.7 Linear Program #4	50
5.3 Comparison to the Transport Equation via MCNP	54
5.4 2-D Dose Optimization for the Current Density Condition: Offset PTV	57
5.4.1 Unoptimized Dose Distribution: Offset PTV	57
5.4.2 LP#1: Offset PTV	60
5.4.3 LP#2: Offset PTV	60
5.4.4 LP#3: Offset PTV	60
5.4.5 LP#4: Offset PTV	63
5.4.6 Concluding Remarks on the Offset and Centered PTV Optimization	63
6 Conclusions	69
6.1 PTV Centered at the Origin	69
6.2 PTV Offset from the Origin	71
6.3 Future Work	71
LIST OF REFERENCES	74
APPENDICES	
Appendix A: Green's Functions Derivation	76
Appendix B: Matlab Code	80

DISCARD THIS PAGE

LIST OF TABLES

Table	Page
2.1 ¹⁹² Ir Important Properties in Water	8
5.1 Optimized Dwell Times for each Linear Program: Centered PTV	46
5.2 Centered PTV: GAMS Execution Time for each Linear Program	47
5.3 Optimized Dwell Times for each Linear Program: Offset PTV	65
5.4 Offset PTV: GAMS Execution Time for each Linear Program	68

DISCARD THIS PAGE

LIST OF FIGURES

Figure	Page
2.1 Breast Brachytherapy Jig Template	5
2.2 Brachytherapy Seeds on a Coin	7
4.1 Coordinate System that Defines the 2-D Green's Function	18
4.2 Single Source Dose Distribution from the Dirichlet Solution	24
4.3 Single Source IsoDose Plot from the Dirichlet Solution	24
4.4 Single Source Dose Distribution for the Neumann Solution	29
4.5 Single Source Isodose Plot for the Neumann Solution	29
4.6 Single Source Dose Distribution for the Current Density Solution	33
4.7 Single Source Isodose Plot for the Current Density Solution	33
4.8 Green's Function Solution Expanded to $N = 15, 30, 100$, and 200 Terms	34
5.1 Five-Plane Triangular Geometry for PTV Centered at the Origin with Nineteen Catheters	39
5.2 Unoptimized Dose Distribution for Nineteen 10-curie Infinite Catheters in 2-D	40
5.3 Unoptimized Isodose for Nineteen 10-curie Infinite Catheters in 2-D	40
5.4 Dose Distribution from LP1 for Nineteen 10-curie Infinite Catheters in 2-D	43
5.5 Isodose Plot from LP1 for Nineteen 10-curie Infinite Catheters in 2-D	43
5.6 Symmetrical Dwell Time Pattern seen by the SSDS	44
5.7 Percent Depth Dose Plot for Ir-192 and the Geometry of the Seed	47

Figure	Page
5.8 Dose Distribution from LP2 for Nineteen 10-curie Infinite Catheters in 2-D	49
5.9 Isodose Plot from LP2 for Nineteen 10-curie Infinite Catheters in 2-D	49
5.10 Dose Distribution from LP3 for Nineteen 10-curie Infinite Catheters in 2-D	51
5.11 Isodose Plot from LP3 for Nineteen 10-curie Infinite Catheters in 2-D	51
5.12 Dose Distribution from LP4 for Nineteen 10-curie Infinite Catheters in 2-D	53
5.13 Isodose Plot from LP4 for Nineteen 10-curie Infinite Catheters in 2-D	53
5.14 Isodose Plots for all Four Linear Programs	54
5.15 MCNP Dose Distribution from the LP4 Optimized Dwell Times	56
5.16 Five-Plane Triangular Geometry for Offset PTV	58
5.17 Unoptimized Dose Distribution for the Offset PTV in 5-Plane Geometry	59
5.18 Unoptimized Isodose Plot for the Offset PTV in 5-Plane Geometry	59
5.19 LP1 Dose Distribution for the Offset PTV in 5-Plane Geometry	61
5.20 LP1 Isodose Plot for the Offset PTV in 5-Plane Geometry	61
5.21 LP2 Dose Distribution for the Offset PTV in 5-Plane Geometry	62
5.22 LP2 Isodose Plot for the Offset PTV in 5-Plane Geometry	62
5.23 LP3 Dose Distribution for the Offset PTV in 5-Plane Geometry	64
5.24 LP3 Isodose Plot for the Offset PTV in 5-Plane Geometry	64
5.25 LP4 Dose Distribution for the Offset PTV in 5-Plane Geometry	66
5.26 LP4 Isodose Plot for the Offset PTV in 5-Plane Geometry	66
5.27 Isodose Plot of all 4 Linear Programs for the Offset PTV in 5-Plane Geometry . .	67

HIGH DOSE-RATE BRACHYTHERAPY OPTIMIZATION FOR BREAST CANCER USING DIFFUSION THEORY

Jason Michael Holzmann

Under the supervision of Professor Douglass L. Henderson

At the University of Wisconsin-Madison

The purpose of this research was to create a new treatment planning optimization routine that would minimize non-uniformity of the dose distribution for high-dose rate (HDR) breast brachytherapy using the diffusion approximation to the radiation transport equation. Current treatment planning systems use dose kernels, transport theory, and geometric modeling to predict the dose distribution from a treatment plan, but a comparison to the diffusion approximation has never been explored for this application. For multi-catheter HDR brachytherapy, the goal of the treatment plan is to optimize the seed dwell times at certain dwell positions along each catheter in order to deliver a prescribed dose to the planned target volume (PTV), while sparing dose to the surrounding cancer-free tissue. With the aid of advanced visualization tools and optimization modeling programs, the new technique hopes to achieve similar results to conventional treatment planning systems. The time-independent diffusion equation has been solved via the Green's function technique for several types of boundary conditions. Performed in two dimensions, an optimization routine using several sets of objective functions and constraints has been applied to the dose matrices of each dwell position, allowing for output of optimal dwell times. An interface between MATLAB and GAMS has been made use of in order to complete this task.

For a geometry with a planned target volume centered at the origin of an eight centimeter in radius circle, a five-plane, triangular setup consisting of nineteen catheters yields our source distribution of dwell positions. Four different linear programs were used to optimize dose distribution within the PTV, which was modeled by a circle with a radius of 2.5 centimeters.

With an objective function of minimizing the maximum deviation from the prescribed dose in the PTV, the forth linear model was deemed most effective at achieving both dose uniformity and conformity for a PTV centered at the origin of a circular boundary. However since in most cases the PTV will not be centered within a volume, a geometry was explored for a PTV offset in the y-direction by four centimeters. Again the same four linear programs were applied to the geometry to seek the the most optimal model. Although it had the best uniformity in the PTV, this time the forth linear program allowed too much dose to the normal tissue region, namely on the boundary the where the skin would exist. With an objective function that minimized the dose to the normal tissue, good dose conformity and fair uniformity essentially deemed the third linear program the best model for a PTV near a boundary. Although the validity of the optimization for the two-dimensional Green's function dose kernels proved poor by comparison to MCNP simulation, the results here showed that optimization routines can be applied using diffusion theory. The usage of GAMS for the linear optimization also proved very efficient, which would make it competitive with today's software. However in order to make a more accurate comparison between the diffusion and transport equation results, a three-dimensional, multi-energy group Green's function solution would need to be developed and optimized for a given geometry.

ABSTRACT

The purpose of this research was to create a new treatment planning optimization routine that would minimize non-uniformity of the dose distribution for high-dose rate (HDR) breast brachytherapy using the diffusion approximation to the radiation transport equation. Current treatment planning systems use dose kernels, transport theory, and geometric modeling to predict the dose distribution from a treatment plan, but a comparison to the diffusion approximation has never been explored for this application. For multi-catheter HDR brachytherapy, the goal of the treatment plan is to optimize the seed dwell times at certain dwell positions along each catheter in order to deliver a prescribed dose to the planned target volume (PTV), while sparing dose to the surrounding cancer-free tissue. With the aid of advanced visualization tools and optimization modeling programs, the new technique hopes to achieve similar results to conventional treatment planning systems. The time-independent diffusion equation has been solved via the Green's function technique for several types of boundary conditions. Performed in two dimensions, an optimization routine using several sets of objective functions and constraints has been applied to the dose matrices of each dwell position, allowing for output of optimal dwell times. An interface between MATLAB and GAMS has been made use of in order to complete this task.

For a geometry with a planned target volume centered at the origin of an eight centimeter in radius circle, a five-plane, triangular setup consisting of nineteen catheters yields our source distribution of dwell positions. Four different linear programs were used to optimize dose distribution within the PTV, which was modeled by a circle with a radius of 2.5 centimeters. With an objective function of minimizing the maximum deviation from the prescribed dose in the PTV, the forth linear model was deemed most effective at achieving both dose uniformity

and conformity for a PTV centered at the origin of a circular boundary. However since in most cases the PTV will not be centered within a volume, a geometry was explored for a PTV offset in the y-direction by four centimeters. Again the same four linear programs were applied to the geometry to seek the the most optimal model. Although it had the best uniformity in the PTV, this time the forth linear program allowed too much dose to the normal tissue region, namely on the boundary the where the skin would exist. With an objective function that minimized the dose to the normal tissue, good dose conformity and fair uniformity essentially deemed the third linear program the best model for a PTV near a boundary. Although the validity of the optimization for the two-dimensional Green's function dose kernels proved poor by comparison to MCNP simulation, the results here showed that optimization routines can be applied using diffusion theory. The usage of GAMS for the linear optimization also proved very efficient, which would make it competitive with today's software. However in order to make a more accurate comparison between the diffusion and transport equation results, a three-dimensional, multi-energy group Green's function solution would need to be developed and optimized for a given geometry.

Chapter 1

Introduction to Brachytherapy

Brachytherapy, a cancer treatment involving the implantation of radioactive sources within or near the tumor, was first proposed around the turn of the century by Alexander Graham Bell. The radioactive sources used in brachytherapy are sometimes called seeds and are about the size of a grain of rice. With the prefix *brachy* meaning “short range,” brachytherapy seeds emit radiation only a short distance when placed within (interstitial) or near (intracavitary) the tumor, allowing low doses to nearby organs [1]. Early brachytherapy experiments used radium as the source, but it was soon deemed unsafe due to the containment seed leaking radioactivity. Today the major isotopes yielding the best results in low dose-rate brachytherapy are Iodine-125 and Palladium-103. Unfortunately, only five percent of human cancers are treatable by these low dose rate implants [1]. However, high dose-rate implants, such as Iridium-192 and Cesium-137, offer an advantage over low-dose rate of speeding up the treatment duration.

High-dose rate brachytherapy (HDRBT) drastically decreases the amount of time that a patient must devote to scheduled treatments. A typical low dose-rate treatment requires on average seven weeks of dedication, while HDRBT accelerates the treatment time to only one week for the total treatment. For this reason as well as the radiobiological advantages to an accelerated treatment schedule, HDRBT is an increasingly popular method.

1.1 Motivation

Treatment planning for brachytherapy is conventionally executed several weeks before the first treatment is administered. Since treatment planning systems (TPS) utilize computed tomography (CT) images of a patient, brachytherapy may be performed on a very different target volume than what was expected by the TPS several weeks prior [2, 3]. For example, changes in treatment planning volumes can be due to adjuvant therapies, anesthesia, and weight loss. The ability to generate an optimal treatment plan in a more efficient manner presents many advantages to the therapeutic outcome. Clearly, if the development of a brachytherapy plan is developed shortly before implementation, then the plan will likely agree with what the physician encounters during operation. Therefore, minimizing the time gap between treatment planning and administration can lead to more accurate dose delivery and a greater survival probability for the patient.

Current treatment planning systems use dose kernels, transport theory, or geometric modeling to predict the dose distribution from a treatment plan, but at this time a comparison of results to the diffusion approximation has never been explored. For multi-catheter HDR brachytherapy, the goal of the treatment plan is to optimize the seed dwell times at certain dwell positions along each catheter that will deliver the prescribed dose to the treatment planning volume (TPV), while sparing dose to the surrounding cancer-free tissue [2, 4, 5]. The dwell times can be optimized using a specific objective function bounded by a set of constraints. The type of algorithm used for optimization depends on whether a linear, nonlinear, or mixed-integer program is explored [6]. In this work, several types of objective functions are explored in order to determine which program yields the best optimized dose distribution.

1.2 Problem Definition

The experimental data presented in this work is based on implementation of multi-catheter HDRBT for stage I or II breast cancer using a ^{192}Ir source. Due to the small-scale of HDRBT

seeds, the ^{192}Ir sources have been approximated as isotropically-emitting dwell positions. Conveniently, solving the time-independent diffusion equation by the method of Green's functions permits the use of one solution for an arbitrarily placed source distribution. This powerful method allows the arbitrary point kernel to be replaced by a specific source distribution (i.e. a set of dwell positions) and generate a solution to the diffusion equation. In this work, the solution to the diffusion equation is known as the particle flux. It is of great interest to have knowledge of the flux distribution because the dose is directly proportional to it; that is if charged particle equilibrium (CPE) exists. In most applications of HDRBT, the energy of the source is low enough that CPE can be assumed.

After the dose distribution is known from each dwell position, the information can be input into an optimization software that obeys an objective function and a set of constraints. Performed in two dimensions, an optimization routine using several sets of objective functions and constraints has been applied to the dose matrices of each dwell position, allowing for output of optimal dwell times at each dwell position. An interface between MATLAB and GAMS has been made use of in order to complete this task. The diffusion approximation results have been compared to the dose predicted from the radiation transport equation by generating the same source distribution in a Monte Carlo N-Particle transport code. Note the work in this research has been performed for only one energy group, ignoring the effect of photon down-scattering before absorption.

New brachytherapy TPS strive to maximize the efficiency of its optimization algorithms to achieve a plan within minutes of operation. Hence efficiency is a key aspect when developing an algorithm that works. If an algorithm cannot reach its solution within a matter of minutes, then competing codes will render it useless. Hence, the efficiency of the HDR optimization algorithm developed in this research is paramount to its feasibility in practice. For this reason, the duration of each optimization routine was noted.

Chapter 2

Multi-Catheter HDRBT Procedure

Outlining the HDRBT procedure is fitting in order to understand the common orientation of catheters as well as the preparation that goes into the treatment. In order for the administration of radiotherapy to mirror that of the optimized treatment plan, it is important that the physician is accurate with needle placement. Below is a brief overview of guidelines that physicians use to prepare and administer treatment. Afterwards, a description of the high-dose rate ^{192}Ir brachytherapy source is provided.

2.1 Preoperative Procedure

Preoperative procedure begins with the use of ultrasound to sketch the lumpectomy cavity position on the skin of the patient. The sketch is used to help the physician visualize catheter placement. Catheter placement is typically in two or three planes and within the sagittal plane. Maintaining the needles within the sagittal plane allows for 3-D reconstruction of the catheters by the treatment planning code. A grid is marked on the patients skin, selecting the pattern of the intended entrance and exit points for each needle catheter [4].

In some cases the catheters enter the breast medially and exit laterally. Other times the implants enter from the inframammary direction and exit toward the cephalad, or direction of the head, beginning with the deepest plane. When positioning these needles, a minimum of 1 cm below cavity is maintained. However, care is taken to remain superficial to the pectoral muscle (chest wall) via fluoroscopic imaging. The placement of the subsequent needles is based on the position of the deep-plane needles [4].

Figure 2.1: Breast Brachytherapy Jig Template



A jig based on the PTV (often 2 or 3-planes) is assembled about the deep needles, which provides a template for the needles in the superior plane(s). For reference, see Figure 2.1 for an image of a jig used for breast brachytherapy¹. The jig template allows for silicon tubing to be punctured in the catheter positions, which remain in place after the jig is removed. These tubes mark the row spacing and guidance for each needle to be inserted during treatments. The physician can then be confident that the catheter needle will not incidentally puncture the pleural region (lung/chest wall) [4].

On average 26 needles are used for HDR breast brachytherapy². After insertion, the steel brachytherapy needles are replaced by plastic button-ended catheters. Assuming an inframammary insertion, the inferior end is held in place by silicon tubing with a 0.5 to 1 cm distance

¹Courtesy of www.nucletron.com

²According to Professor Bruce Thomadsen, PhD, a radiation oncologist at the UW-Hospital

between the tubing and skin maintained to account for postoperative swelling. The closed off button ends face cephalad, allowing HDR seed loading from the inframammary direction [4].

2.2 Varification of Set-up and Dose

Each catheter has its precise length measured using a dummy source. The patient is then allowed to recover from the catheter operation for several days. After recovery, the patient is CT scanned, usually in 5-millimeter slices. These CT DICOMS are transferred to the treatment planning software (TPS), for optimization. Several structures are contoured in the TPS, including the planned target volume (PTV), lung, and skin. The PTVs are typically defined with a 5-millimeter margin from the catheter axis in the transverse plane. A 10-millimeter margin was maintained in the sagittal plane. In order to limit skin dose and prevent fat necrosis. 10 mm is also maintained between the first dwell position and the skin contour. The same gap is required for the last dwell position. For dwell positions within the PTV, all must be further than 15 mm from the skin contour [4].

In most TPS, 5-millimeter intervals are maintained between dwell positions. The dwell times for each position are optimized by the TPS via an algorithm that meets dose homogeneity index (DHI) requirements. The optimization must be adjusted if $DHI < 0.8$. From the DHI, the TPS generates a dose-volume histogram (DVH) that summarizes the dose to the target and critical organs. The target will receive a typical prescribed dose of 34 Gy in ten fractions. Hence the patient is treated twice daily with at least a six-hour interfractional interval [2, 3, 4, 7].

2.3 The ^{192}Ir Source

^{192}Ir is a high dose-rate source when it emits a dose rate of greater than 12 gray-per-hour. The energy range of ^{192}Ir is between 136 and 1060 keV, with an average energy of 380 keV [1]. Its half-life is 74.2 days and the activity, or source strength, of the HDR seed is usually between 5 and 10 curies [1, 3].



Figure 2.2: Comparison of Brachytherapy Seeds to a Coin.

Figure 2.2 depicts an image comparing the size of brachytherapy seeds to a US dollar coin³. The image provides the reader with an idea of the small-scale of the radioactive seeds. Clearly from the image above, the brachytherapy seeds are quite small even compared to a coin. The cylindrical high dose-rate ^{192}Ir seeds have outer dimensions of about 0.117 cm in diameter by 0.51 cm in length. The radioactive dimensions within the encapsulation shell are about 0.065 cm in diameter by 0.35 cm in length [7]. In addition to the physical properties of the HDR seed, it is also important to note the properties of the 380 keV source in water.

Since the human body consists of between 60 and 70% water, it is common in radiotherapy applications to approximate human tissue as water [1]. This is of course inaccurate when presented with a region of the body that includes a great deal of heterogeneity, but for the breast it is a fairly good approximation. Therefore, it is important to understand the characteristics of the HDR source within water. Table 2.1 lists several properties of ^{192}Ir in water [8]. Noted in the table are the average energy (\bar{E}), energy absorption coefficient (μ_{en}), linear energy-transfer

³Courtesy of www.coreoncology.com

Table 2.1: ^{192}Ir Important Properties in Water.

Property	^{192}Ir
\bar{E} [keV]	380
μ_{en} [cm^{-1}]	0.0326
μ_{tr} [cm^{-1}]	0.0326
μ_T [cm^{-1}]	0.1086
σ_C [cm^{-1}]	0.1068
$\bar{\mu}_0$	0.25892
D [cm]	4.139
L [cm]	11.267

coefficient (μ_{tr}), total attenuation coefficient (μ_T), Compton scattering coefficient (σ_C), average cosine of the scattering angle ($\bar{\mu}_0$), diffusion coefficient (D), and diffusion length (L).

Chapter 3

The Diffusion Approximation and Green's Function for Dose

Often times approximations to models or equations are made in order to simplify calculations and also to provide an adequate description of a systems behavior. In nuclear engineering, a common approximation to the radiation transport equation is called diffusion theory, in which the angular dependence of the transport equation is expanded linearly to its first moment. Under diffusion theory, sources emit particles isotropically, or with equal probability in all directions, and scattering is treated linear, anisotropically [9]. Diffusion theory also assumes that the probability of a particle being scattered in a medium is much greater than being absorbed. The simplified diffusion theory provides a fairly good approximation to the actual physics of a system. Furthermore, the time-independent diffusion equation reduces to a convenient form of a modified Helmholtz equation, as shown below with respect to a right circular, cylindrical coordinate system (r, θ, z) [9]:

$$-D\nabla^2\Phi(r, \theta, z) + \mu_{en}\Phi(r, \theta, z) = \frac{S_0}{r}\delta(r - r_0, \theta - \theta_0, z - z_0). \quad (3.1)$$

Here D is the diffusion coefficient [cm], $\Phi(r, \theta, z)$ is the particle flux [$\frac{\text{particles}}{\text{cm}^2\text{s}}$], μ_{en} is the energy absorption coefficient [cm^{-1}], S_0 is the source strength [$\frac{\text{particles}}{\text{s}}$], and $\delta(r - r_0, \theta - \theta_0, z - z_0)$ is the Dirac delta function for a point source located at cylindrical coordinates (r_0, θ_0, z_0) . Cylindrical coordinates are fitting for the geometry of breast radiotherapy used in this simulation, which models the breast as a cylinder.

3.1 Green's Function Solution

Although brachytherapy seeds are not infinitely small — they are actually about the size of a grain of rice — modeling a seed by an isotropic source position is a fair approximation. In fact, a point source approximation is often performed for geometric optimization [5]. Although, note that a two-dimensional solution to the modified Helmholtz equation actually models each seed as an infinite line source [10]. Modeling each dwell position as a source presents a useful technique for solving the modified Helmholtz equation by the generation of a Green's Function Kernel. The goal of the Green's function is to obtain the flux distribution due to each specific source location.

It is typical to set up a Green's function problem as listed below in Equations 3.2 and 3.3. Here the vector \vec{x} represents a position in three-space, while $\Phi(\vec{x})$ is the flux, k is a constant, $S(\vec{x})$ is the source distribution, $G(\vec{x}; \vec{x}')$ is the Green's function, and $\delta(\vec{x} - \vec{x}')$ is the Dirac delta function that specifies a point source at the location \vec{x}' :

$$\nabla^2 \Phi(\vec{x}) - k^2 \Phi(\vec{x}) = S(\vec{x}), \quad (3.2)$$

$$\nabla^2 G(\vec{x}; \vec{x}') - k^2 G(\vec{x}; \vec{x}') = \delta(\vec{x} - \vec{x}'). \quad (3.3)$$

To generate the Green's Function solution for $\Phi(\vec{x})$, it is typical to subtract Equation 3.3 from Equation 3.2, after multiplying Equation 3.2 by $G(\vec{x}; \vec{x}')$ and Equation 3.3 by $\Phi(\vec{x}')$. Note that for this manipulation, \vec{x}' has replaced \vec{x} in Equation 3.2. Then both sides are integrated over all point space (V') to result in the following equation [11]:

$$\begin{aligned} \int_{V'} \left[G(\vec{x}; \vec{x}') \nabla^2 \Phi(\vec{x}') - \Phi(\vec{x}') \nabla^2 G(\vec{x}; \vec{x}') \right] d\vec{x}' &= \\ \int_{V'} G(\vec{x}; \vec{x}') S(\vec{x}') d\vec{x}' - \int_{V'} \Phi(\vec{x}') \delta(\vec{x} - \vec{x}') d\vec{x}' &. \end{aligned} \quad (3.4)$$

Using the divergence theorem and the definition of the Dirac delta function results in the general expression for the Green's function solution [11]:

$$\Phi(\vec{x}) = \int_{V'} G(\vec{x}; \vec{x}') S(\vec{x}') d\vec{x}'^3 + \oint_{S'} [\Phi(\vec{x}') \vec{\nabla}' G(\vec{x}; \vec{x}') - G(\vec{x}; \vec{x}') \vec{\nabla}' \Phi(\vec{x}')] \cdot \vec{n} dS'. \quad (3.5)$$

The flux distribution is achieved by integrating over the product of the source and Green's function within the volume and also adding the contribution of the boundary terms. In certain cases, the contribution from the boundary terms in Equation 3.5 vanish. This is true specifically for the Dirichlet, Neumann, and Robin boundary conditions.

3.1.1 Boundary Conditions on the Helmholtz Equation

Three types of boundary conditions are typically explored that eliminate the source terms in the Green's Function solution; they are called the Dirichlet, Neumann, and Robin boundary conditions [11, 12, 13]. The first of these, the Dirichlet condition, specifies that the solution (i.e. flux) must take on a specific value (i.e. f) on the boundary (\mathcal{B}). In math terms this is shown below in Equation 3.6:

$$\Phi(\vec{x}) = f, \quad \forall \vec{x} \in \mathcal{B}. \quad (3.6)$$

The Dirichlet problem poses perhaps the most simple solution to a partial differential equation. The Neumann condition specifies the value that the derivative of the solution must take on the boundary. This derivative is with respect to the surface normal, as given in Equation 3.7:

$$\frac{\partial \Phi(\vec{x})}{\partial n} = f, \quad \forall \vec{x} \in \mathcal{B}. \quad (3.7)$$

The Robin boundary condition (sometimes called impedance boundary condition) is a weighted linear combination of the Dirichlet and Neumann conditions. This is shown below in Equation 3.8, where α and β are constants. The solution to the Robin boundary condition can be of much greater complexity than those of the Dirichlet and Neumann conditions:

$$\alpha \Phi(\vec{x}) + \beta \frac{\partial \Phi(\vec{x})}{\partial n} = f, \quad \forall \vec{x} \in \mathcal{B}. \quad (3.8)$$

Of particular interest to the field of nuclear engineering is the case of the Robin boundary condition that specifies the radiation current density on the boundary. According to Fick's Law of diffusion, the current density is given by $\vec{J} = -D \vec{\nabla} \Phi(\vec{x})$, where \vec{J} is the current density and D is the diffusion coefficient [9]. When Fick's Law is divided between an into-the-boundary (J_-) and out-of-the-boundary (J_+) current density, it takes on the form of the Robin condition [9, 14]:

$$J_- = \frac{\Phi(\vec{x})}{4} + \frac{D}{2} \frac{\partial \Phi(\vec{x})}{\partial n}, \quad (3.9)$$

$$J_+ = \frac{\Phi(\vec{x})}{4} - \frac{D}{2} \frac{\partial \Phi(\vec{x})}{\partial n}. \quad (3.10)$$

If any of the above boundary conditions are used, then the Green's function solution reduces to Equation 3.11 [11, 12]:

$$\Phi(\vec{x}) = \int_{V'} G(\vec{x}; \vec{x}') S(\vec{x}') d\vec{x}'^3. \quad (3.11)$$

Once the flux distribution is known, the dose at each point in a volume or surface can be calculated, assuming charged particle equilibrium exists.

3.2 Charged Particle Equilibrium

The flux distribution is of interest because it can be used to calculate the dose allocation under certain conditions. Since the source energy of ^{192}Ir is considered fairly low, the electrons that are set in motion by the low energy photons will also be of low energy. Hence electrons set in motion will not travel a large distance in the medium before they dispense all of their energy. We can therefore assume that the dose is equal to the kinetic energy released per unit mass (KERMA). The condition where dose is equivalent to KERMA is known as charged particle equilibrium and invokes the following relationship between dose and flux [8]:

$$D_n(r, \theta, z) = E \Phi(r, \theta, z) \frac{\mu_{en}}{\rho} T_n. \quad (3.12)$$

Here, $D_n(r, \theta, z)$ is the dose to point (r, θ, z) from seed n [Gy], E is the energy of the absorbed photon [keV], $\frac{\mu_{en}}{\rho}$ is the mass energy absorption coefficient [$\frac{\text{cm}^2}{\text{g}}$], and T_n is the dwell time for seed n in seconds. A dose matrix can be generated for each brachytherapy source position by inserting the respective flux matrix into the above dose formula. Once all dose matrices are known from each source location, the total dose distribution to the geometry is found by simply summing the dose distributions over all source positions.

An important note to make is that all of the constants in the dose and flux equations are known or available in texts, except for one important constant—the diffusion coefficient. Therefore the following section will provide the definition and expression for the diffusion coefficient. Finally, the diffusion coefficient will be calculated for the average photon energy of ^{192}Ir .

3.3 Calculation of the Diffusion Coefficient

The diffusion coefficient D can be calculated by determining the average cosine of the scattering angle for a photon denoted by $\bar{\mu}_0$. The formal definition of the diffusion coefficient arising from Fick's Law is given in Equation 3.13 [14, 9]:

$$D = \frac{1}{3 \mu_{tr}} = \frac{1}{3 \cdot (\mu_T - \bar{\mu}_0 \sigma_c)} . \quad (3.13)$$

Here μ_{tr} is the energy transfer coefficient, μ_T is the total interaction coefficient, and σ_c is the Compton scattering coefficient for photons of a specific energy traversing a certain medium. Hence in order to calculate the diffusion coefficient correctly, the expression for $\bar{\mu}_0$ needs to be derived. This is simply performed as the mean of the scattering angle, when a Compton scattering event occurs. The average scattering angle for a Compton Scattering event is defined by $\bar{\mu}_0 = \cos \theta$ or $\bar{\mu}_0 = \hat{\Omega} \cdot \hat{\Omega}$. The formal expression for $\bar{\mu}_0$ is as follows [9]:

$$\bar{\mu}_0 = \frac{\int_{4\pi} \frac{d_e \sigma_c}{d\hat{\Omega}} \cos \theta d\hat{\Omega}}{\int_{4\pi} \frac{d_e \sigma_c}{d\hat{\Omega}}} , \quad (3.14)$$

where

$$d\hat{\Omega} = \sin \theta d\theta d\phi . \quad (3.15)$$

The Klein-Nishina cross-section, $\frac{d_e\sigma_c}{d\hat{\Omega}}$, is the differential angular elastic scattering cross section of the photon with an electron [15]. It takes the form given by Equation 3.16, where $\alpha = E_\gamma/m_e c^2$ and $r_o = e^2/m_e c^2$:

$$\frac{d_e\sigma_c}{d\hat{\Omega}} = r_0^2 \left(\frac{1 + \cos^2 \theta}{2} \right) \left[\frac{1}{1 + \alpha (1 - \cos \theta)} \right]^2 \left\{ 1 + \frac{\alpha^2 (1 - \cos \theta)^2}{(1 + \cos^2 \theta)[1 + \alpha (1 - \cos \theta)]} \right\} . \quad (3.16)$$

Integration of the Klein-Nishina cross-section yields the interaction probability per electron of an incident photon to undergo a Compton scattering event. It has the units of $\left[\frac{\text{cm}^2}{\text{steradian-electron}} \right]$ and when integrated over a solid angle $d\hat{\Omega}$ yields the Compton scattering cross-section per electron, $e\sigma_c$, with units of $\frac{\text{cm}^2}{\text{electron}}$. Note that $\sigma_c = Z e\sigma_c$, where Z is the atomic number of an atom.

The result after performing the integration of Equation 3.14 is listed below:

$$\bar{\mu}_0 = \frac{-6\alpha^5 + 16\alpha^4 + 46\alpha^3 + 30\alpha^2 + 6\alpha + \ln(1 + 2\alpha)[4\alpha^5 - 27\alpha^3 - 37\alpha^2 - 18\alpha - 3]}{\alpha(2\alpha^4 + 18\alpha^3 + 16\alpha^2 + 4\alpha + \ln(1 + 2\alpha)[4\alpha^4 - 4\alpha^3 - 15\alpha^2 - 10\alpha - 2])} . \quad (3.17)$$

From this result, the diffusion coefficient can be calculated for a photon of any incident energy. In the case of ^{192}Ir , which yields photons of average energy equal to 380 keV, $\alpha = \frac{380 \text{ keV}}{511 \text{ keV}}$ and plugging this into Equation 3.17 gives $\bar{\mu}_0 = 0.25892$ and a resulting average angle of about $\theta = 75^\circ$. With $\mu_T = 0.1086 \text{ cm}^{-1}$ and $\sigma_c = 0.1084 \text{ cm}^{-1}$ [8], the corresponding value for the diffusion coefficient of ^{192}Ir is 4.139 centimeters. D will be used in future calculations and is hidden in the constant term (k) of the modified Helmholtz equation, where $k^2 = \frac{1}{L^2} = \frac{\mu_{en}}{D}$.

Now that a detailed background of diffusion theory has been presented, the two dimensional Green's function can be generated and then the flux distribution can be converted into a dose matrix. Finally, an optimization routine can be performed on a chosen geometry of brachytherapy source positions and the resulting dose distribution can be analyzed.

Chapter 4

The Two-Dimensional Green's Function Solution

A two-dimensional Green's function has been generated for the time-independent diffusion equation. In polar coordinates, a Green's function kernel has been solved for cases of the Dirichlet, Neumann, and Robin boundary conditions. For each case the Green's function was used to determine the particle flux due to a point source and then converted to dose by assumption of charged-particle equilibrium.

The dose profile for each point was output from MATLAB into the optimization modeling program called GAMS in order to determine optimal dwell times. The cases were solved using several sets of objective functions and constraints in order to study which optimization model yielded the best dose uniformity and conformity to the PTV. The first of the boundary conditions studied is a case of the Dirichlet condition.

4.1 2-D Dirichlet Boundary Condition

Listed below are the time-independent diffusion equation and the Dirichlet boundary condition that specifies a zero flux at the boundary of radius R . These equations are specified in polar coordinates. Also displayed is the corresponding equation that satisfies the Green's function [13]:

$$\nabla^2 \Phi(r, \theta) - k^2 \Phi(r, \theta) = S(r, \theta), \quad (4.1)$$

$$\Phi(R, \theta) = 0, \quad (4.2)$$

$$\nabla^2 G(r, \theta; r', \theta') - k^2 G(r, \theta; r', \theta') = \frac{1}{r} \delta(r - r', \theta - \theta'). \quad (4.3)$$

In the term $k^2 = \frac{1}{L^2}$, L is the diffusion length in centimeters given by $\frac{1}{L} = \sqrt{\frac{\mu_{en}}{D}}$. L essentially quantifies the root-mean-square distance that a photon emitted from a source will travel before absorption [9, 14]. The diffusion coefficient D and energy absorption coefficient μ_{en} are defined in the previous chapter on diffusion theory.

Before diving into the solution to the Green's function, the general solution to the homogeneous modified Helmholtz equation will be derived using the separation of variables technique:

$$\nabla^2 \phi(r, \theta) - k^2 \phi(r, \theta) = 0 ,$$

$$\text{let } \phi(r, \theta) = R(r) \Theta(\theta) ,$$

$$\frac{1}{r} \frac{\partial}{\partial r} \left(r \frac{\partial R(r) \Theta(\theta)}{\partial r} \right) + \frac{1}{r^2} \frac{\partial^2 R(r) \Theta(\theta)}{\partial \theta^2} - k^2 R(r) \Theta(\theta) = 0 ,$$

$$\frac{1}{r} \left[\frac{dR(r)}{dr} \Theta(\theta) + r \frac{d^2 R(r)}{dr^2} \Theta(\theta) \right] + \frac{1}{r^2} \frac{d^2 \Theta(\theta)}{d\theta^2} R(r) - k^2 R(r) \Theta(\theta) = 0 ,$$

$$\frac{r^2}{R(r) \Theta(\theta)} \left[\frac{d^2 R(r)}{dr^2} \Theta(\theta) + \frac{1}{r} \frac{dR(r)}{dr} \Theta(\theta) + \frac{1}{r^2} \frac{d^2 \Theta(\theta)}{d\theta^2} R(r) - k^2 R(r) \Theta(\theta) \right] = 0 ,$$

$$r^2 \frac{R''(r)}{R(r)} + r \frac{R'(r)}{R(r)} + \frac{\Theta''(\theta)}{\Theta(\theta)} - r^2 k^2 = 0 ,$$

$$r^2 \frac{R''(r)}{R(r)} + r \frac{R'(r)}{R(r)} - r^2 k^2 = -\frac{\Theta''(\theta)}{\Theta(\theta)} = n^2 ,$$

where n is the separation constant. The equation for the angular component, $\Theta(\theta)$, is:

$$\Theta''(\theta) + n^2 \Theta(\theta) = 0 ,$$

and its general solution is:

$$\Theta(\theta) = A_n \cos n\theta + B_n \sin n\theta , \quad n = 1, 2, \dots, \infty . \quad (4.4)$$

The equation for the radial component $R(r)$ is:

$$R''(r) + \frac{1}{r} R'(r) - \left(\frac{n^2}{r^2} + k^2 \right) R(r) = 0 .$$

This is the modified Bessel Equation that takes on the following solution involving the modified Bessel Functions of the first (I_n) and second (K_n) kind:

$$R(r) = C_n I_n(kr) + D_n K_n(kr), \quad n = 1, 2, \dots, \infty. \quad (4.5)$$

Finally, the general solution is given by the product of the two results:

$$\phi(r, \theta) = \sum_{n=0}^{\infty} [A_n \cos n\theta + B_n \sin n\theta] \cdot [C_n I_n(kr) + D_n K_n(kr)]. \quad (4.6)$$

The above solution will be called upon in the derivation of the Green's function. At this point a Green's function solution to Equation 4.3 can be derived for a point source located at (r', θ') . It is first important to note the characteristics of a Green's function.

4.1.1 2-D Dirichlet Green's Function

Equation 4.3 is solved in this section and the constraints of the solution are listed below [11, 12, 13]. Here the domain \mathcal{D} is the area inside of the boundary \mathcal{B} :

$$\begin{aligned} \nabla^2 G(r, \theta; r', \theta') - k^2 G(r, \theta; r', \theta') &= \frac{1}{r} \delta(r - r', \theta - \theta') \quad \text{in } \mathcal{D}, \\ G = 0 \quad &\text{on } \mathcal{B}. \end{aligned} \quad (4.7)$$

Next some properties of the Green's function are defined. First, the reciprocity theorem holds for G (i.e. it is symmetric) [13, 16]:

$$G(r, \theta; r', \theta') = G(r', \theta'; r, \theta). \quad (4.8)$$

Second, the continuity of G holds for all r, θ, r', θ' ; however the derivative of G with respect to the outward normal n to the boundary is discontinuous at the point (r', θ') which is shown below in Equation 4.9 [9]:

$$\lim_{\rho \rightarrow 0} \int_{C_\rho} \vec{e}_s \cdot \vec{J}_s \, ds = 1,$$

$$\lim_{\rho \rightarrow 0} \int_{C_\rho} \vec{e}_s \cdot (-D \vec{\nabla} G) \, ds = 1,$$

$$\lim_{\rho \rightarrow 0} \int_{C_\rho} -D \frac{\partial G}{\partial n} ds = 1 . \quad (4.9)$$

Here \vec{e}_s is the interface surface normal and \vec{J}_s is the current density in the direction of the outward normal. In two-dimensions, n is normal to the circle of radius ρ defined below:

$$\rho^2 = (x - x')^2 + (y - y')^2 .$$

To fully define the polar coordinates with respect to the circle defined above, the translation from Cartesian to polar coordinates is defined in Equation 4.10 and plotted in Figure 4.1:

$$\begin{aligned} x &= r \cos \theta , & x' &= r' \cos \theta' , \\ y &= r \sin \theta , & y' &= r' \sin \theta' . \end{aligned} \quad (4.10)$$

Note that the boundary of this geometry is defined by the radius where $r = R$. These characteristics of a Green's function will be used to generate the solution for the Dirichlet boundary

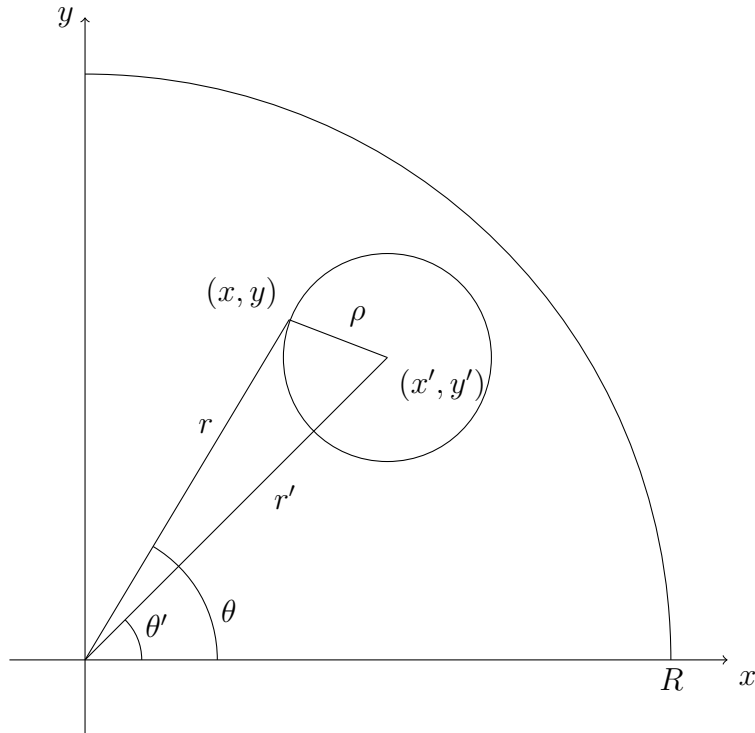


Figure 4.1: Coordinate System that Defines the 2-D Green's Function

condition. The first step is to break the Green's function into a linear combination of the homogeneous and particular solution [13]. As seen below, $g(r, \theta; r', \theta')$ is the homogeneous solution and $F(r, \theta; r', \theta')$ is the free-space, or particular solution [13]:

$$G(r, \theta; r', \theta') = g(r, \theta; r', \theta') + F(r, \theta; r', \theta') , \quad (4.11)$$

$$\nabla^2 F(r, \theta; r', \theta') - k^2 F(r, \theta; r', \theta') = \frac{1}{r} \delta(r - r', \theta - \theta') \quad \text{in } \mathcal{D}, \quad (4.12)$$

$$\nabla^2 g(r, \theta; r', \theta') - k^2 g(r, \theta; r', \theta') = 0 \quad \text{in } \mathcal{D}. \quad (4.13)$$

First, the free space solution will be generated, which will also be applicable to the other boundary conditions. For everywhere outside the point $x = x'$ and $y = y'$, $\rho = \sqrt{(x - x')^2 + (y - y')^2} > 0$ and hence $\nabla^2 F(r, \theta; r', \theta') - k^2 F(r, \theta; r', \theta') = 0$ [13]. The solution for the free space equation for $r > 0$ reduces to a modified Bessel's equation and takes the form shown in Equation 4.14:

$$F(\rho) = A I_0(k\rho) + B K_0(k\rho) . \quad (4.14)$$

Since we are looking for a solution with a discontinuity in the derivative, we eliminate the I_0 term because for small ρ it is not singular. Hence we choose $A = 0$ and are left with the modified Bessel function of the second kind, and of order zero [11, 17, 18, 19] :

$$F(\rho) = B K_0(k\rho) . \quad (4.15)$$

We then note that for very small ρ [20]:

$$K_0(k\rho) \longrightarrow -[\ln \rho - 0.11593] \sim -\ln \rho . \quad (4.16)$$

Now we can apply the jump condition to the free space solution given by Equation 4.9. Note the D below is the diffusion coefficient and that ρ is the radius of a circle defined by polar coordinates to be at the point (r', θ') . Using the law of cosines $\rho = \sqrt{r^2 + r'^2 - 2rr' \cos(\theta - \theta')}$,

ρ can be considered a function of r , r' , θ , and θ' (i.e. $\rho(r, \theta; r', \theta')$). This definition for a circle C_ρ allows the singular point to be translated to (r', θ') :

$$\begin{aligned} \lim_{\rho \rightarrow 0} \int_{C_\rho} -D \frac{\partial F}{\partial n} ds &= 1, \\ \lim_{\rho \rightarrow 0} \int_{C_\rho} -D B \frac{dK_0(k\rho)}{d\rho} ds &= 1, \\ \lim_{\rho \rightarrow 0} \int_{C_\rho} -D B \frac{d(-\ln \rho)}{d\rho} ds &= 1, \\ - \left[-D B \frac{1}{\rho} (2\pi\rho) \right] &= 1, \\ B &= \frac{1}{2\pi D}, \\ F(\rho) &= \frac{1}{2\pi D} K_0(k\rho), \\ F(r, \theta; r', \theta') &= \frac{1}{2\pi D} K_0(k\sqrt{r^2 + r'^2 - 2rr' \cos(\theta - \theta')}). \end{aligned} \quad (4.17)$$

Now the boundary condition can be applied in order to find the value of the homogeneous solution on the boundary. Since on the boundary, \mathcal{B} , $G = g + F = 0$ to satisfy this specific Dirichlet condition, we can make the following conclusion on the boundary [13]:

$$\begin{aligned} g &= -F \quad \text{on } \mathcal{B}, \\ g(R, \theta, r', \theta') &= -\frac{1}{2\pi D} K_0(k\rho(R, \theta, r', \theta')) \quad \text{on } \mathcal{B}. \end{aligned} \quad (4.18)$$

The general solution for g within the boundary in the domain takes on the general solution to the homogeneous case as shown in Equation 4.6. However, the modified Bessel function of the second kind must be eliminated from the solution because it contains a singularity, for which the particular equation already accounts. The resulting homogeneous solution is shown below

in Equation 4.19:

$$g(r, \theta; r', \theta') = \sum_{n=0}^{\infty} [A_n \cos n\theta + B_n \sin n\theta] \cdot I_n(kr) . \quad (4.19)$$

The r' and θ' terms in Equation 4.19 will manifest themselves after the coefficients are solved. Generating the coefficients is the next step in the Green's function solution.

The coefficients for the homogeneous solution must be determined based on Dirichlet boundary condition. Orthogonality of the sine and cosine functions will be the key technique used to isolate the terms. Note that the $n = 0$ term yields only a result for the A_0 term since the $\sin(0)$ eliminates the B_0 term. Let us pursue the result for the A_0 term via the following derivation:

$$\begin{aligned} g(R, \theta; r', \theta') &= -\frac{1}{2\pi D} K_0(k\rho(R, \theta, r', \theta')) = A_0 I_0(kR) , \\ \int_0^{2\pi} -\frac{1}{2\pi D} K_0(k\rho(R, \theta, r', \theta')) d\theta &= \int_0^{2\pi} A_0 I_0(kR) d\theta , \\ \int_0^{2\pi} -\frac{1}{2\pi D} K_0(k\rho(R, \theta, r', \theta')) d\theta &= 2\pi A_0 I_0(kR) , \\ A_0 &= -\frac{1}{4\pi^2 D I_0(kR)} \int_0^{2\pi} K_0 \left[k\sqrt{R^2 + r'^2 - 2Rr' \cos(\theta - \theta')} \right] d\theta . \end{aligned} \quad (4.20)$$

Note the use of the law of cosines in the A_0 term, where on the boundary $\rho(R, \theta; r', \theta') = \sqrt{R^2 + r'^2 - 2Rr' \cos(\theta - \theta')}$, to meet the boundary radius $r = R$.

The next step in the solution is to solve for the rest of the A_n terms by the use of orthogonality of the sine and cosine functions. This process is outlined below:

for $n = 1, 2, \dots, \infty$,

$$g(R, \theta; r', \theta') = -\frac{1}{2\pi D} K_0(k\rho(R, \theta; r', \theta')) = I_n(kR) \cdot [A_n \cos n\theta + B_n \sin n\theta] ,$$

then we multiply both sides by $\cos m\theta$ and integrate from 0 to 2π :

$$\int_0^{2\pi} -\frac{1}{2\pi D} K_0(k\rho(R, \theta; r', \theta')) \cos m\theta d\theta = \int_0^{2\pi} I_n(kR) \cdot [A_n \cos n\theta + B_n \sin n\theta] \cos m\theta d\theta ,$$

the above integral $\neq 0$ iff $m = n$,

$$\begin{aligned} \int_0^{2\pi} -\frac{1}{2\pi D} K_0(k\rho(R, \theta; r', \theta')) \cos m\theta d\theta &= A_m I_m(kR) \int_0^{2\pi} \cos^2 m\theta d\theta , \\ \int_0^{2\pi} -\frac{1}{2\pi D} K_0(k\rho(R, \theta; r', \theta')) \cos m\theta d\theta &= A_m I_m(kR) \frac{1}{2} \int_0^{2\pi} [1 + \cos(2m\theta)] d\theta , \\ \int_0^{2\pi} -\frac{1}{2\pi D} K_0(k\rho(R, \theta; r', \theta')) \cos m\theta d\theta &= A_m I_m(kR) \frac{1}{2} \left[\theta + \frac{1}{2m} \sin(2m\theta) \right]_0^{2\pi} , \\ \int_0^{2\pi} -\frac{1}{2\pi D} K_0(k\rho(R, \theta; r', \theta')) \cos m\theta d\theta &= A_m I_m(kR) \frac{1}{2} (2\pi) , \\ A_n &= -\frac{1}{2\pi^2 D I_n(kR)} \int_0^{2\pi} K_0 \left[k\sqrt{R^2 + r'^2 - 2Rr' \cos(\theta - \theta')} \right] \cos n\theta d\theta , \end{aligned} \quad (4.21)$$

for all $n = 1, 2, \dots, \infty$.

A similar approach is used for the extraction of the B_n coefficient, again using orthogonality for the sine function:

$$\begin{aligned} g(R, \theta; r', \theta') &= -\frac{1}{2\pi D} K_0(k\rho) = I_n(kR) \cdot [A_n \cos n\theta + B_n \sin n\theta] , \\ \text{for } n &= 1, 2, \dots, \infty , \end{aligned}$$

$$\int_0^{2\pi} -\frac{1}{2\pi D} K_0(k\rho(R, \theta; r', \theta')) \sin m\theta d\theta = \int_0^{2\pi} I_n(kR) \cdot [A_n \cos n\theta + B_n \sin n\theta] \sin m\theta d\theta .$$

As before the above integral $\neq 0$ iff $m = n$, and reduces to:

$$\begin{aligned} B_n &= -\frac{1}{2\pi^2 D I_n(kR)} \int_0^{2\pi} K_0 \left[k\sqrt{R^2 + r'^2 - 2Rr' \cos(\theta - \theta')} \right] \sin n\theta d\theta , \end{aligned} \quad (4.22)$$

for all $n = 1, 2, \dots, \infty$.

Finally it is possible to display the entire solution consisting of a linear combination of the homogeneous and particular terms of the Green's function. We also remember that the solution

for the flux was given in the diffusion chapter by Equation 3.11. At this point the entire solution will be displayed for completeness:

$$\begin{aligned} G(r, \theta; r', \theta') &= \frac{1}{2\pi D} K_0(k\sqrt{r^2 + r'^2 - 2rr' \cos(\theta - \theta')}) \\ &+ A_0 I_0(kr) + \sum_{n=1}^{\infty} I_n(kr) [A_n \cos n\theta + B_n \sin n\theta] , \end{aligned} \quad (4.23)$$

$$A_0 = -\frac{1}{4\pi^2 D I_0(kR)} \int_0^{2\pi} K_0 \left[k\sqrt{R^2 + r'^2 - 2Rr' \cos(\theta - \theta')} \right] d\theta , \quad (4.24)$$

$$A_n = -\frac{1}{2\pi^2 D I_n(kR)} \int_0^{2\pi} K_0 \left[k\sqrt{R^2 + r'^2 - 2Rr' \cos(\theta - \theta')} \right] \cos n\theta d\theta , \quad (4.25)$$

$$B_n = -\frac{1}{2\pi^2 D I_n(kR)} \int_0^{2\pi} K_0 \left[k\sqrt{R^2 + r'^2 - 2Rr' \cos(\theta - \theta')} \right] \sin n\theta d\theta , \quad (4.26)$$

$$\Phi(r, \theta) = \int_0^{2\pi} \int_0^R S(r', \theta') G(r, \theta; r', \theta') r' dr' d\theta' . \quad (4.27)$$

For a point source of uniform strength S_0 located at point (r_0, θ_0) , the source term takes on the form of $S(r, \theta) = S_0 \frac{1}{r} \delta(r - r_0) \delta(\theta - \theta_0)$. Of course then when this source distribution is plugged into Equation 4.27, r must be replaced by r' and θ replaced by θ' , thus integrating over the correct source variables.

4.1.2 Dose Distribution for 2-D Dirichlet Solution

As discussed in the diffusion chapter in the section on charged particle equilibrium, a simple relationship can be assumed between the flux and dose. The conversion involves multiplying the flux by several constants to result in the conventional dose units of gray. Since this solution is for only one energy group (i.e. it does not account for absorption of down-scattered photons) the energy used in the dose calculation will be for the average energy of ^{192}Ir , 380 keV. Also included in the dose conversion of the flux is $\frac{\mu_{en}}{\rho}$, or the mass energy absorption coefficient, which has a value of 0.0326 $\frac{\text{cm}^2}{\text{g}}$. For the remaining terms, the flux matrix is generated from the

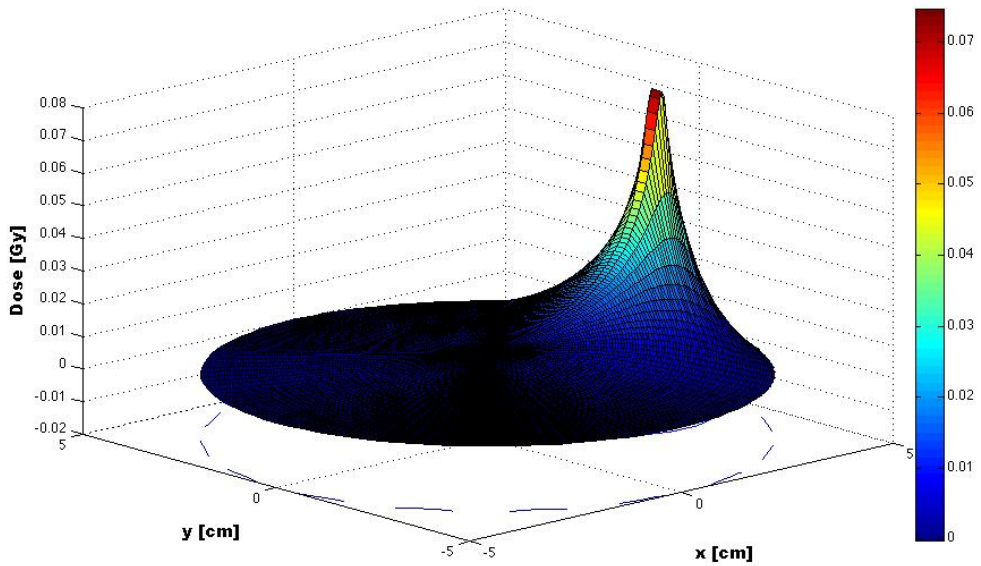


Figure 4.2: Single source dose distribution for the Dirichlet solution of a 10-Ci point source at $r = 4$ cm and $\theta = 0$ radians.

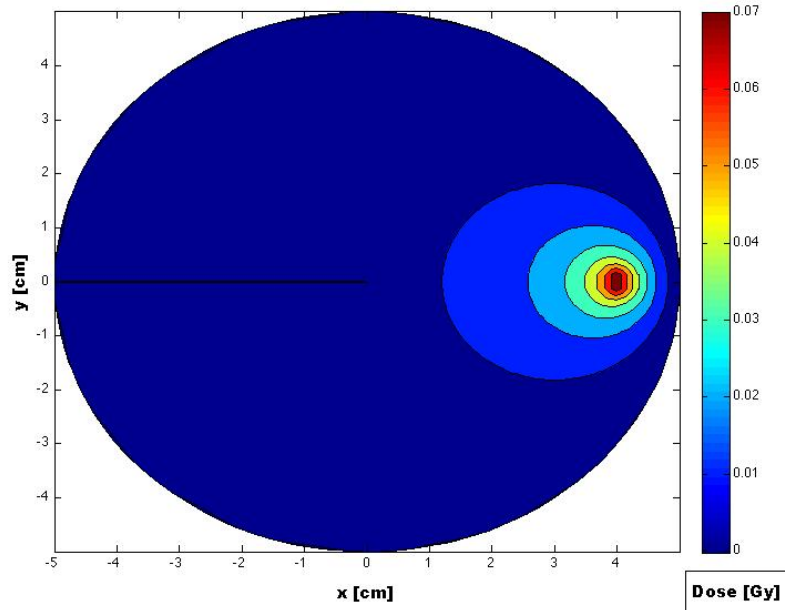


Figure 4.3: Single Source isodose plot for the Dirichlet Solution of a 10-Ci Point Source at $r = 4$ cm and $\theta = 0$ radians.

above Green's function, while the dwell time is the variable to be solved for in an optimization routine. Note that in order to convert the dose terms into the correct units of gray, where $1 \text{ Gy} = 1 \frac{\text{J}}{\text{kg}}$, it must be multiplied by $1.6022 \times 10^{-13} \frac{\text{Gy}}{\text{keV}}$ [8]. In addition, the source strength used for the simulations was 10 curies and the Green's function solution was expanded to 15 terms of the infinite series. The reasons for expanding the solution to only fifteen terms will be explained later in the chapter.

It is fitting to show the resulting dose distribution that results from one seed with a unit dwell time of one second. The results from the Green's function solution require numerical integration in order to be solved; that is, it is not possible to analytically integrate the variables buried within the Bessel functions. In order to perform this task, MATLAB has been called upon due to its ability to manipulate large matrices and generate advanced plots.

In Figure 4.2 the dose distribution resulting from the Dirichlet boundary condition has been plotted using MATLAB. The dose distribution in gray [Gy] is displayed for a 10-Ci point source placed at the position $r = 4 \text{ cm}$ and $\theta = 0$ radians. The spike in dose at this point indicates its position. Clearly the Dirichlet boundary condition was met as the dose falls off to zero on the boundary, a radius of 5 cm.

A cross-sectional view of the dose distribution is shown in Figure 4.3 and is known as an isodose plot. The source location is easily confirmed with this cross sectional slice of the dose distribution. Isodose plots are commonly used in the field of radiation oncology in order to identify the dose value to specific regions of treatment, such as the planned target volume or organs at risk.

4.2 2-D Neumann Boundary Condition

The diffusion equation solved in this section will be subject to a Neumann boundary condition where the radius $r = R$. To reiterate, the value of the derivative is specified on the boundary for a Neumann condition. In this case, we specify the value of the derivative of the flux to be zero on the boundary. The Green's function will be generated for the following set

of equations:

$$\begin{aligned}\nabla^2\Phi(r, \theta) - k^2\Phi(r, \theta) &= S(r, \theta), \\ \frac{\partial\Phi(R, \theta)}{\partial n} &= 0 \quad \text{on } \mathcal{B}.\end{aligned}\tag{4.28}$$

Here n is the outward normal and is in the direction of r for the homogeneous solution and in the direction of ρ for the particular solution to the Green's function.

4.2.1 2-D Neumann Green's Function

The Green's function to be solved for the Neumann condition is specified below:

$$\begin{aligned}\nabla^2G(r, \theta; r', \theta') - k^2G(r, \theta; r', \theta') &= \frac{1}{r} \delta(r - r', \theta - \theta') \quad \text{in } \mathcal{D}, \\ \frac{\partial G(R, \theta; r', \theta')}{\partial n} &= 0 \quad \text{on } \mathcal{B}.\end{aligned}\tag{4.29}$$

Again the Green's function will be broken up into the particular (free-space) and homogeneous solution. The linear combination of the two will create our Green's function. Fortunately, the free-space solution for the Neumann condition does not change from that presented for the Dirichlet condition. Therefore, we can jump directly into solving the homogeneous case. In the general solution, only the coefficients will change for the Neumann condition because nothing else in the solution is effected by the boundary condition. In addition, we can anticipate the following relationship on the boundary:

$$\begin{aligned}\frac{\partial G(R, \theta; r', \theta')}{\partial n} &= 0, \\ \frac{\partial(g(R, \theta; r', \theta') + F(R, \theta; r', \theta'))}{\partial n} &= 0, \\ \frac{dg}{dr} &= -\frac{dF}{d\rho} \quad \text{on } \mathcal{B}.\end{aligned}\tag{4.30}$$

The relationship in Equation 4.30 exists because the outward normal to g is r , where as the outward normal to F is ρ . Knowing that the derivative of the K_0 function is $\frac{dK_0(k\rho)}{d\rho} =$

$-k K_1(k\rho)$ and recalling the free-space solution is $F = \frac{1}{2\pi D} K_0(k\rho)$, we can draw the following conclusion on the boundary [20]:

$$\begin{aligned}\frac{dg}{dr} &= -\frac{dF}{d\rho}, \\ \frac{dg}{dr}|_{r=R} &= \frac{k}{2\pi D} K_1(k\rho(R, \theta; r', \theta')) .\end{aligned}\quad (4.31)$$

The relationship shown in Equation 4.31 can be used to evaluate the coefficients on the boundary by taking the derivative of the general solution for g . The derivation of the coefficients will not be explicitly shown in this section as it was for the Dirichlet boundary condition; however, the two-dimensional Neumann coefficients are explicitly derived in Appendix A.

Performing the extraction of the coefficients results in the Green's function solution for the Neumann condition. The solution is displayed below:

$$\begin{aligned}G(r, \theta; r', \theta') &= \frac{1}{2\pi D} K_0(k\sqrt{r^2 + r'^2 - 2rr' \cos(\theta - \theta')}) \\ &\quad + A_0 I_0(kr) + \sum_{n=1}^{\infty} I_n(kr) [A_n \cos n\theta + B_n \sin n\theta] ,\end{aligned}$$

where

$$A_0 = \frac{1}{4\pi^2 D I_1(kR)} \int_0^{2\pi} K_1(k\sqrt{R^2 + r'^2 - 2Rr' \cos(\theta - \theta')}) d\theta , \quad (4.32)$$

$$A_n = \frac{1}{\pi^2 D [I_{n-1}(kR) + I_{n+1}(kR)]} \int_0^{2\pi} K_1(k\sqrt{R^2 + r'^2 - 2Rr' \cos(\theta - \theta')}) \cos n\theta d\theta , \quad (4.33)$$

$$B_n = \frac{1}{\pi^2 D [I_{n-1}(kR) + I_{n+1}(kR)]} \int_0^{2\pi} K_1(k\sqrt{R^2 + r'^2 - 2Rr' \cos(\theta - \theta')}) \sin n\theta d\theta . \quad (4.34)$$

Then the resulting flux and dose distributions are:

$$\Phi(r, \theta) = \int_0^{2\pi} \int_0^R S(r', \theta') G(r, \theta; r', \theta') r' dr' d\theta' , \quad (4.35)$$

$$D_m(r, \theta) = E \Phi(r, \theta) \frac{\mu_{en}}{\rho} T_m \quad [Gy]. \quad (4.36)$$

The dose equation above yields a dose matrix to all of the domain in (r, θ) from the source position m , where T_m is the dwell time for that specific dwell position.

4.2.2 Dose Distribution for the 2-D Neumann Solution

Figure 4.4 shows the dose distribution for a single point source that results from the Green's function subject to the Neumann boundary condition. The dose distribution in gray [Gy] is displayed for a 10-curie point source placed at the position $r = 2$ cm and $\theta = \frac{\pi}{3}$ radians. The spike in dose at this point indicates its position. It is apparent that the Neumann boundary condition was met as the derivative of the dose falls off to zero on the boundary, a radius of 5 cm. In contrast to the plot for the Dirichlet solution, the value of the dose is not forced to zero on the boundary in Figure 4.4. The isodose plot of Figure 4.5 reiterates the previous statement and verifies the location of the dwell position.

The dose distribution for a single point source has been shown for the Dirichlet and Neumann boundary conditions. Developing these two solutions has presented us with an idea of what to expect from a weighted linear combination of the two, or the Robin condition. In the following section, a special case of a Robin boundary condition called the partial current density boundary condition — in this case the inward current density (J_-) — has been applied to generate a Green's function solution.

4.3 2-D Robin (Current Density) Boundary Condition

The form of the Robin boundary condition solved in this section forces the inward current, that is current into the boundary from outside, to zero by $J_-(R, \theta) = 0$. This means that a weighted linear combination of the Dirichlet and Neumann conditions is forced to zero on the

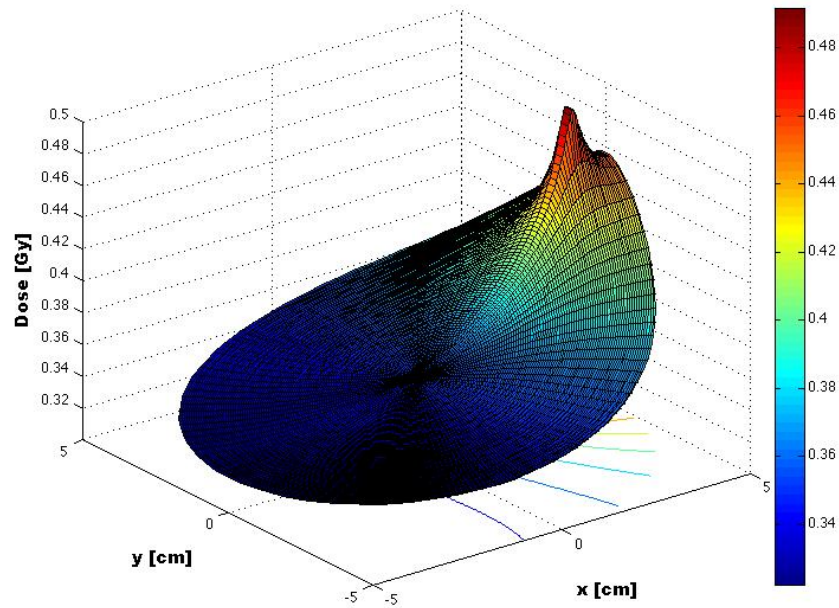


Figure 4.4: Single source dose distribution for the Neumann solution with a 10-Ci point source located at $r = 4$ cm and $\theta = 0$ radians.

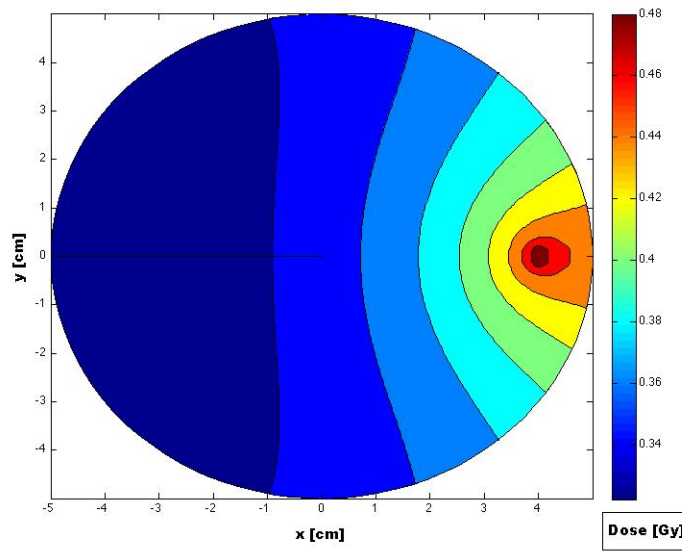


Figure 4.5: Single source isodose plot for the Neumann solution with a 10-Ci point source located at $r = 4$ cm and $\theta = 0$ radians.

boundary. The solution we are looking for is specified by the following equations:

$$\begin{aligned} \nabla^2 \Phi(r, \theta) - k^2 \Phi(r, \theta) &= S(r, \theta), \\ J_-(R, \theta) &= \frac{\Phi(R, \theta)}{4} + \frac{D}{2} \frac{\partial \Phi(R, \theta)}{\partial n} = 0. \end{aligned} \quad (4.37)$$

As with the previous solutions, the above set of equations will be solved via Green's function method.

4.3.1 2-D Current Density Green's Function

The general solution to the Green's function takes on the same form as with the Dirichlet and Neumann conditions. The free-space solution also takes on the same form as previously discussed and its value on the boundary will be used to evaluate the coefficients of the homogeneous solution. The Green's function to be solved for the J_- condition is specified below:

$$\begin{aligned} \nabla^2 G(r, \theta; r', \theta') - k^2 G(r, \theta; r', \theta') &= \frac{1}{r} \delta(r - r', \theta - \theta') \quad \text{in } \mathcal{D}, \\ J_-(R, \theta) &= \frac{G}{4} + \frac{D}{2} \frac{\partial G}{\partial n} = 0 \quad \text{on } \mathcal{B}. \end{aligned} \quad (4.38)$$

The inward current density boundary condition yields the coefficients to the Green's function solution by using the following relationship:

$$\begin{aligned} \frac{G}{4} + \frac{D}{2} \frac{\partial G}{\partial n} &= 0 \quad \text{on } \mathcal{B}, \\ \frac{(g + F)}{4} + \frac{D}{2} \frac{\partial(g + F)}{\partial n} &= 0, \\ g + 2 D \frac{\partial g}{\partial n} &= - \left(F + 2 D \frac{\partial F}{\partial n} \right), \\ g + 2 D \frac{\partial g}{\partial r} &= - \left(F + 2 D \frac{\partial F}{\partial \rho} \right), \\ g + 2 D \frac{\partial g}{\partial r} &= - \frac{1}{2\pi D} [K_0(k\rho(R, \theta; r', \theta')) - 2Dk K_1(k\rho(R, \theta; r', \theta'))], \end{aligned}$$

$$g + 2 D \frac{\partial g}{\partial r} = \frac{1}{2\pi D} [2Dk K_1(k\rho(R, \theta; r', \theta')) - K_0(k\rho(R, \theta; r', \theta'))] . \quad (4.39)$$

Equation 4.39 will be used to evaluate the coefficients and finalize the Green's function for the current density solution. As with the previous Green's functions, these coefficients have been extracted using the orthogonality relationship of trigonometric functions and are derived explicitly in Appendix A. The final solution for the current density condition is listed below:

$$\begin{aligned} G(r, \theta; r', \theta') &= \frac{1}{2\pi D} K_0(k\sqrt{r^2 + r'^2 - 2rr' \cos(\theta - \theta')}) \\ &+ A_0 I_0(kr) + \sum_{n=1}^{\infty} I_n(kr) [A_n \cos n\theta + B_n \sin n\theta] , \end{aligned}$$

where

$$\begin{aligned} A_0 &= \frac{1}{4\pi^2 D [I_0(kR) + k I_1(kR)]} \times \\ &\int_0^{2\pi} [2Dk K_1(k\sqrt{R^2 + r'^2 - 2Rr' \cos(\theta - \theta')}) \\ &+ K_0(k\sqrt{R^2 + r'^2 - 2Rr' \cos(\theta - \theta')})] d\theta , \end{aligned} \quad (4.40)$$

$$\begin{aligned} A_n &= \frac{1}{2\pi^2 D \{I_n(kR) + \frac{k}{2} [I_{n-1}(kR) + I_{n+1}(kR)]\}} \times \\ &\int_0^{2\pi} [2Dk K_1(k\sqrt{R^2 + r'^2 - 2Rr' \cos(\theta - \theta')}) \\ &+ K_0(k\sqrt{R^2 + r'^2 - 2Rr' \cos(\theta - \theta')})] \cos n\theta d\theta , \end{aligned} \quad (4.41)$$

$$\begin{aligned} B_n &= \frac{1}{2\pi^2 D \{I_n(kR) + \frac{k}{2} [I_{n-1}(kR) + I_{n+1}(kR)]\}} \times \\ &\int_0^{2\pi} [2Dk K_1(k\sqrt{R^2 + r'^2 - 2Rr' \cos(\theta - \theta')}) \\ &+ K_0(k\sqrt{R^2 + r'^2 - 2Rr' \cos(\theta - \theta')})] \sin n\theta d\theta . \end{aligned} \quad (4.42)$$

4.3.2 Dose Distribution for the 2-D Current Density Condition

The dose distribution for a point source located at $r = 4$ cm and $\theta = 0$ radians has been plotted in Figure 4.6. Again the source strength is 10 curies and the dwell time for this position is for one second. By comparison, the dose field for the current density solution sits somewhere in between that of the Dirichlet and Neumann. Clearly indicated in the plot, it is apparent that the Neumann boundary condition is weighted greater than the Dirichlet, since the derivative of the dose is nearly zero on \mathcal{B} .

Notice in Figure 4.6 that the dose values are greater than those of the Dirichlet solution, yet less than those of the Neumann solution. The dose distribution shape for the current density solution resembles that of the Neumann solution, but when comparing the isodose plots of Figures 4.7 and 4.5 it is clear that the dose contours are not equivalent.

4.4 Concluding Remarks on the 2-D Green's Function

For each of the solutions shown above, the Green's function solution was expanded to 15 terms in its infinite series. This was deemed sufficient as the higher-order terms contributed little to the solution. Figure 4.8 shows that when generating solutions that expanded the terms to $N = 15, 30, 100$, and 200 , there was no apparent difference between the results. Therefore, to save on computer time, the smallest of the these ($N = 15$ terms) was used to generate the results for the previous boundary conditions as well as those optimized in the next chapter.

The two-dimensional Green's function solution subject to the current density boundary condition is the solution of interest. It essentially allows a current of radiation to leave the boundary of tissue being treated without the possibility of re-entering. Since all of the source positions are within the geometry, we are assuming with the current density boundary condition that photons escaping the boundary will not scatter in air and return to contribute to the dose. Because the Compton scattering cross section in air is very low for 380 keV photons, it is reasonable to assume that the into-the-boundary current density is zero. It will therefore be considered our final two-dimensional Green's function solution.

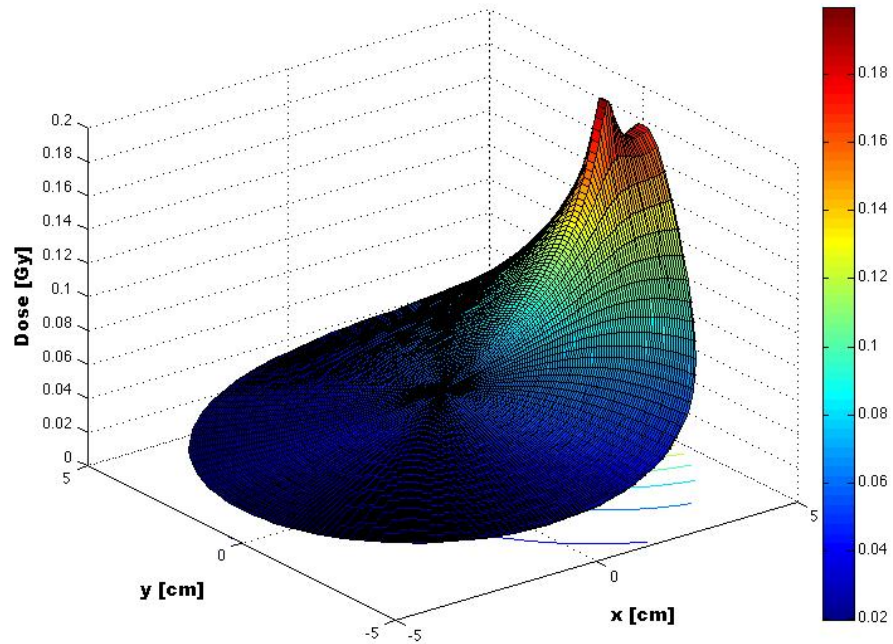


Figure 4.6: Single source dose distribution for the current density solution with a 10-Ci Point Source located at $r = 4$ cm and $\theta = 0$ radians.

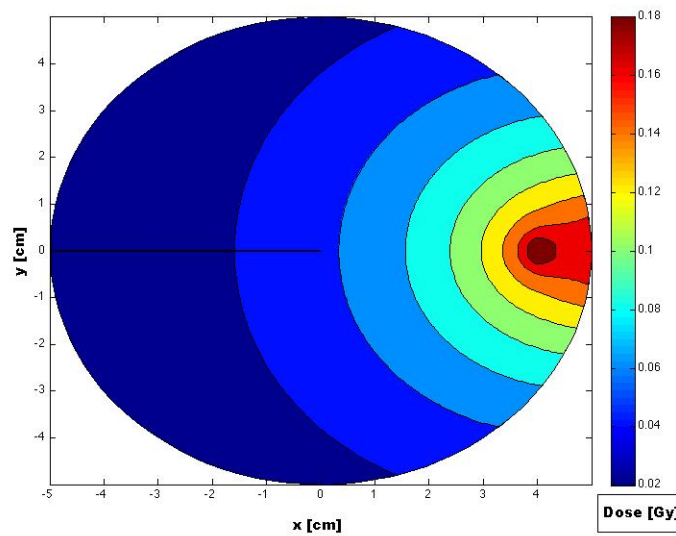


Figure 4.7: Single source isodose plot for the current density solution with a 10-Ci Point Source located at $r = 4$ cm and $\theta = 0$ radians.

Now that the 2-D analytical expression has been derived for the Green's function solution subject to the current density boundary condition, we can pursue with creating a field of source positions. In the following chapter, a field of point sources will represent several catheters that distribute a dose to a given geometry. Because this is for two dimensions, the catheters are considered infinite in the z-direction. The distribution will be displayed for the unoptimized dwell times (dwell times of unity) and later compared to those optimized with several linear programs.

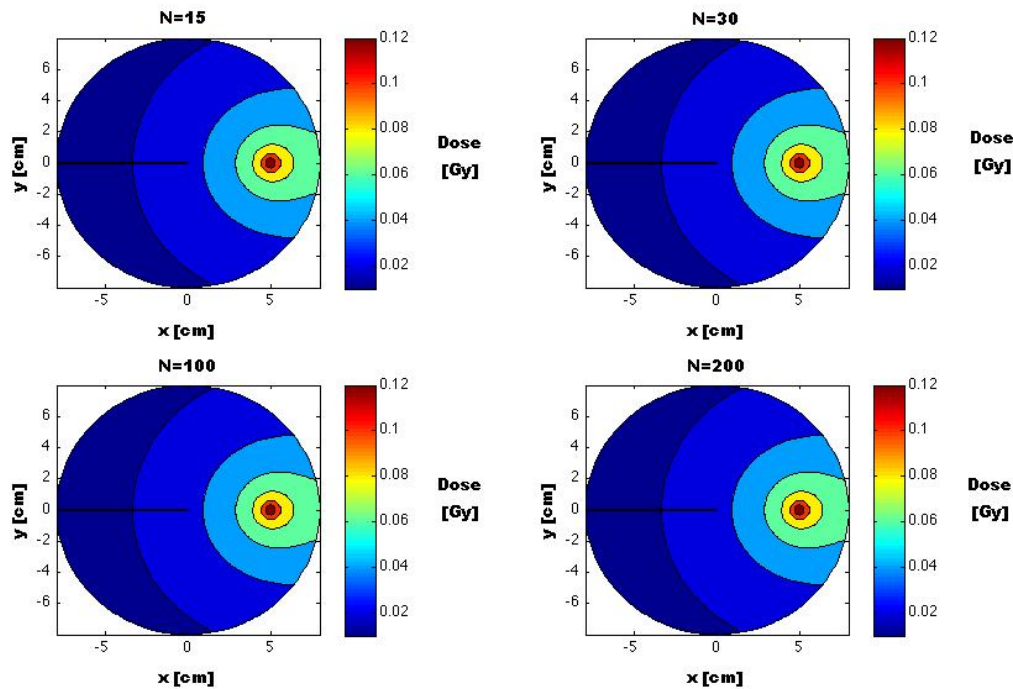


Figure 4.8: Green's Function Solution Expanded to $N = 15, 30, 100$, and 200 Terms

Chapter 5

Two-Dimensional Dose Optimization

The two-dimensional Green's functions solved in the last chapter led up to our desired solution, requiring the condition of zero particle current directed into the boundary. This solution has allowed us to generate a matrix for the particle flux and hence, by a simple conversion, a solution to the dose. By creating a geometry of source positions, or dwell positions, each with a corresponding dose matrix, the dwell times at each location can be optimized in order to achieve a uniform dose that conforms to the planned target volume.

In this chapter, optimization routines have been developed and applied to an arbitrary geometry of normal tissue and target volume. Several objective functions and constraints were explored to determine the linear model resulting in the most uniform dose distribution and hence optimal dwell times. The optimization models were developed in a sophisticated software called GAMS. In the following sections we will first outline the method used by GAMS for solving linear programs. Next, the Paris Dosimetry System is discussed, which determines catheter geometry based on the size of the target volume. Finally, four linear programs will be developed and used to optimize the dwell times for a geometry with a PTV centered at the origin within a boundary and then with it offset from the origin.

5.1 Optimization Modeling using GAMS

GAMS, the general algebraic modeling system, is useful because it provides highly efficient optimization for linear, nonlinear, and mixed integer programs. An even more appealing aspect of GAMS is that it can interface with MATLAB (matrix laboratory), which allows for

plotting results using advanced visualization tools. Since the Green's Function solution to the Helmholtz equation requires numerical integration of an infinite series, MATLAB was used because of its computational abilities.

5.1.1 MATLAB / GAMS Interface

Once several dose matrices are developed from the flux kernels of individual source positions, the MATLAB-GAMS interface is summoned. Requiring some background, courtesy of a paper by University of Wisconsin-Madison Professor Michael Ferris, and a few extra lines of code in each script, the MATLAB-GAMS interface makes it possible for a MATLAB script to be executed and have matrices output into a GAMS model [21]. The GAMS model was then solved for optimal dwell times and the values were sent back to MATLAB. Finally, the results are plotted using the visualization tools of MATLAB for analysis.

5.1.2 GAMS Data Exchange

In order to communicate between the two programs, the creation of a GDX (GAMS Data eXchange) file from MATLAB is essential. The matrices generated by MATLAB can be placed into a GDX file by executing a GDX-write function, written by Professor Michael Ferris [21]. In the case for the dwell time optimization model, each GDX file contains parameters of the dose matrix from each of the source positions. The GAMS model for the problem calls the GDX by loading the files containing the dose matrices into the model. The model is then solved based on an objective function and a set of constraints, and the dwell-time solution is relayed back to MATLAB for further analysis.

5.1.3 Linear Programming in GAMS

There are several solver packages offered by GAMS and one of the most popular is called Cplex. Solving complex linear, quadratically constrained and mixed integer programs in an efficient manner was the sole purpose for the creation of Cplex optimizers. In this work, Cplex version 12 will be utilized. Several algorithms can be called upon by Cplex solvers, but the

majority of linear programming problems are solved with Cplex's notorious dual simplex algorithm [22].

5.1.4 The Simplex Method

The simplex method is a numerical algorithm used for solving linear programs. The simplex concept makes use of a polytope of dimension N and hence $N + 1$ vertices. The polytope is a line segment in one dimension (variable), triangle in two, tetrahedron in three and hence, in many dimensions it is known as an arbitrary polytope [23].

With N dimensions, a polytope is defined by N system of inequalities that yield a feasible region for the solution to a linear program. By starting at a vertex, the simplex method works its way to the optimal solution by moving along the edges of the polytope in the direction of the next feasible solution, where a more optimal solution to the objective function occurs. Obviously, if the objective is to minimize, then the solution moves to the vertex with the smaller objective function, and vice versa for a maximization linear program. The simplex process is repeated over several iterations until the optimal value is determined [23].

5.2 2-D Dose Optimization for the Current Density Condition: Centered PTV

The Paris Dosimetry System (PDS) was originally designed for low dose rate implants, wires or strings but has been applied to high dose rate brachytherapy using dwell positions with equal time. However, this requires that the active length of the catheters (i.e. the region along which the source dwells) to extend beyond the the target volume. An extension and modification of the PDS, called the Stepping Source Dosimetry System (SSDS), is a system that seeks to optimize the dwell times of the HDR stepping source in order to maintain active lengths within the target volume [5]. The SSDS results in longer dwell times at ends of the catheters and decreased dwell times in the center in order to achieve dose uniformity across the PTV.

Clearly, the goal of dwell time optimization in this research requires the model of the SSDS. There are several rules by which the catheter placement and active lengths are given. Using an arbitrary geometry for the PTV and normal tissue, the SSDS has been applied to our model and used to optimize dwell times. Of course since at this point we only have a 2-D solution, the dwell times will model the time for our infinite catheters.

5.2.1 Geometry Definition: Centered PTV

The arbitrary geometry explored for the dose optimization is shown in Figure 5.1. The boundary radius is $R = 8$ cm and the PTV is centered at the origin with a radius of 2.5 centimeters. This is considered a large target volume and therefore by PDS rules will require multi-plane catheters.

The catheter spacing, S , required for a PTV this size is 1.3 centimeters according to the rules of the SSDS [5]. Since a multi-plane geometry is needed to cover the PTV, the catheter spacing allows a five-plane geometry to maintain the catheters inside the target volume. The five-plane geometry will be organized in triangular spacing as shown in Figure 5.1. The most distal plane, or the furthest from the body, will be specified as the upper plane and contains three catheters. Moving to the four next proximal planes, the number of catheters in each plane are four, five, four, and three, respectively, where the most proximal plane will be called the lower plane. Using this triangular geometry for the catheters makes each neighboring catheter in a neighboring plane offset by half the catheter spacing. The triangular, five-plane catheter setup with three, four, five, four, and three catheters in respective planes yields the most optimal organization to conform to a circular target volume. Figure 5.1 shows the five-plane geometry and each individual catheter location designated by the green x's. Additionally, they are numbered one through nineteen, beginning with the upper plane, leftmost catheter [5]. Labeling each catheter will make it easier to explain the dwell time for each position after optimization is performed.

5.2.2 Unoptimized Dose

The geometry described above is displayed as a dose distribution in Figure 5.2 and as an isodose plot in Figure 5.3. Note the symmetry of the result. Here, the dwell times for all dwell positions (nineteen catheters) have been set to one second. From the isodose, contour plot, the location of some of the catheters are apparent, especially toward the center of the geometry. The dose is greater from sources near the center of the PTV because photons emitted there have a lower chance of escaping the geometry, since they will have to travel through more tissue than photons emitted closer to the boundary. Therefore, inner dwell positions and catheters have a

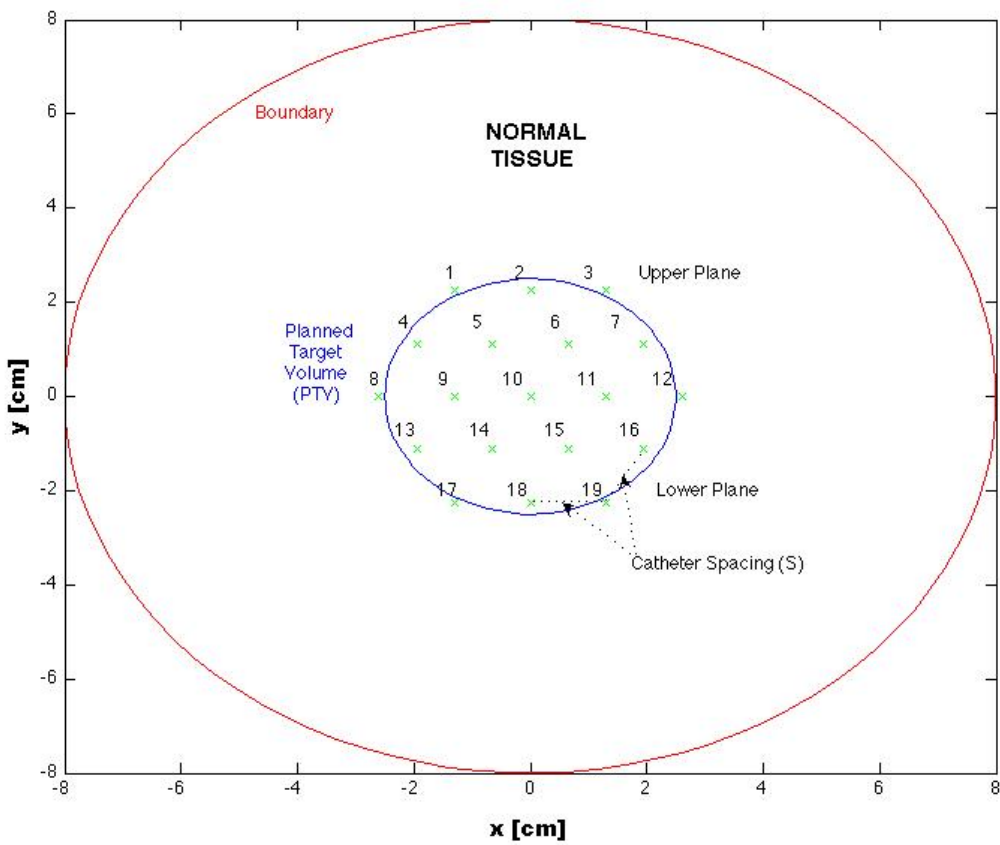


Figure 5.1: Five-Plane Triangular Geometry for PTV Centered at the Origin with Nineteen Catheters

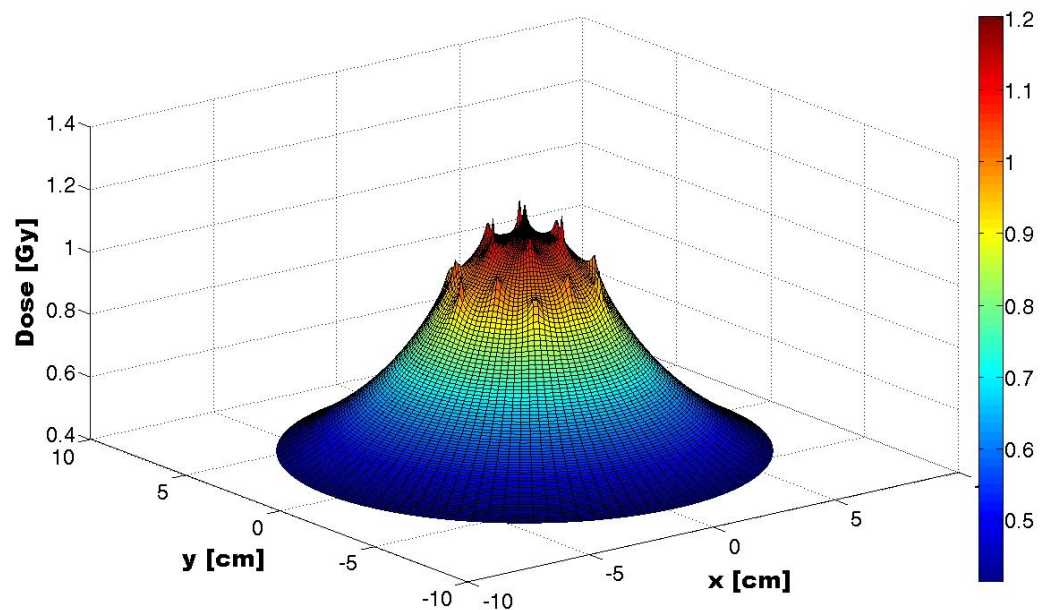


Figure 5.2: Unoptimized Dose Distribution for Nineteen 10-curie Infinite Catheters in 2-D

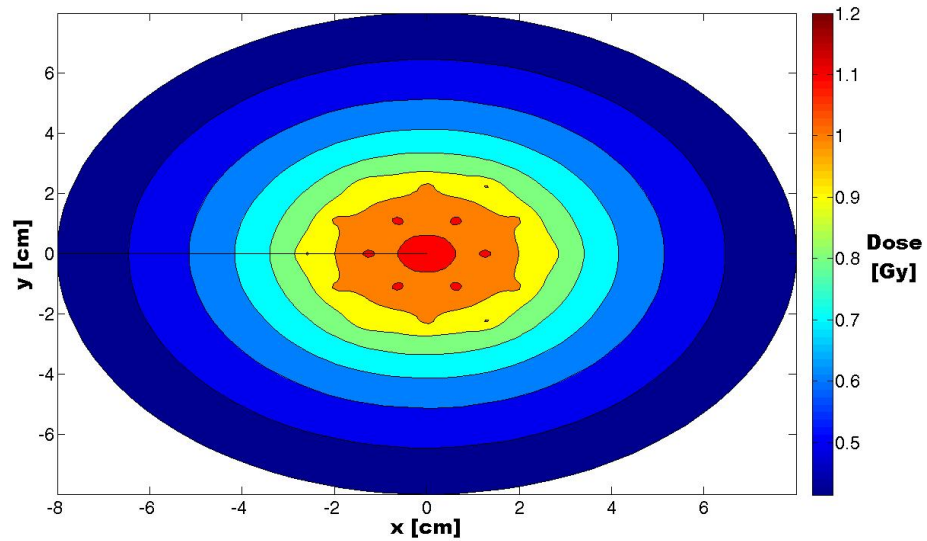


Figure 5.3: Unoptimized Isodose for Nineteen 10-curie Infinite Catheters in 2-D

greater probability of setting electrons in motion, which deposit their energy in the volume as they slow down. The energy deposition per unit mass is the measurement of dose that is seen in these plots. Our goal now is to optimize the dwell time for each dwell position to achieve a uniform or nearly uniform dose that conforms to the PTV.

5.2.3 A Note on Optimization Routine Duration

As aforementioned, it is important for a treatment planning optimization routine to develop optimal dwell times for a given catheter setup in a very efficient manner. If the Green's function method for developing dose kernels were ever used to create a treatment planning system, the optimization time would be considered separate from the time to generate the dose kernels. For instance, the dose kernels for an n -plane setup could be stored in a data base for all boundary sizes and possible dwell positions. This would be important to the efficiency of a treatment planning software because generating the dose kernels via the Green's function method can be quite time consuming. In fact, depending on the type of numerical integration used, the number of terms to which the infinite series is expanded, and the speed of a computer, a dose kernel could take tens of minutes to generate.

Due to the nontrivial time required to generate dose kernels, the efficiency of the optimization algorithms will not be based off of the generation of the dose kernels, but strictly on the time it takes to solve the optimization model. As mentioned above, GAMS uses highly advanced simplex algorithms to generate its solutions to linear programs. This makes GAMS a very efficient software for solving complex models, even when they are very large. Although the models presented below will not be solved for a large number of variables (i.e. dwell times), they are very capable of doing so. Hence in the case that a three-dimensional dose kernel is developed, where hundreds of variables will need to be manipulated, GAMS may still be utilized. For the two-dimensional routines developed below with a small number of variables, the linear programs are solved very quickly and the completion time for each is noted.

5.2.4 Linear Program #1

There are several possible linear programming models that are applied to dose optimization in radiation therapy [6]. The first linear program (LP1) explored for this work uses an objective function that minimizes the integral dose to the entire breast region. The function was subject to the constraint of a lower bound on the dose to the tumor region. The model formulation is as follows in Equation 5.1:

$$\begin{aligned}
 \min \quad & \sum_{x,y} D_{xy}, \\
 \text{subject to} \quad & D_{xy} = \sum_{n=1}^N T_n \dot{D}_{xy}^n \quad \forall(x,y), \\
 & D_p \leq D_{kl} \quad \forall(k,l) \in PTV, \\
 & T_n \geq 0 \quad \forall n.
 \end{aligned} \tag{5.1}$$

Here, k and l are a subset of x and y , respectively, that include the planned target volume region. The constraints also require the minimum dose to the PTV to be set as the prescribed dose, where $D_p = 3.4$ Gy, and all dwell times, T_n , be non-negative. Note that N is the total number of dwell positions and \dot{D}_{xy}^n is the dose rate from a dwell position n in gray-per-second.

Inputting the dose matrices from the nineteen-catheter setup aligned in a centered planned target volume, the LP1 GAMS model optimizes the dwell times according to the objective function and constraints of Equation 5.1. The results were relayed back into MATLAB and plotted in a dose distribution, Figure 5.4, and isodose plot in Figure 5.5. In the isodose plot, the PTV is outlined by a white circle, designating the 2.5 centimeter radius centered at the origin of the geometry. It is clear from the isodose plot that the regions of hot spots within the PTV are large and that the dose is quite nonuniform. However, the conformity of the prescribed dose iso-contour to the circular PTV is fairly good with this linear program.

The optimal dwell times for LP1 as well as the other linear programs (to be defined) are displayed in Table 5.1. The routine came up with a common pattern seen in high dose rate

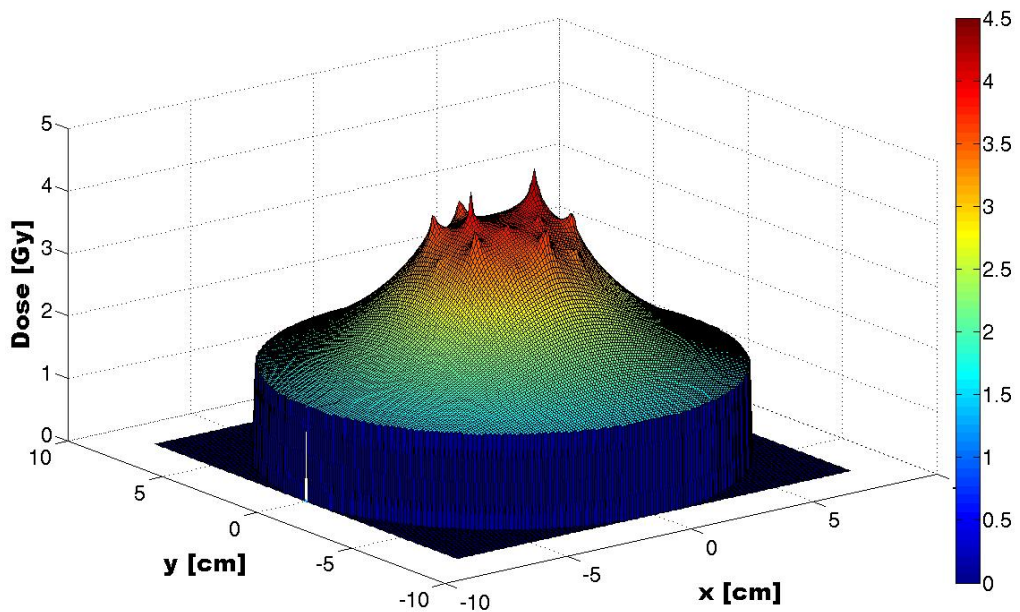


Figure 5.4: Dose Distribution from LP1 for Nineteen 10-curiel Infinite Catheters in 2-D

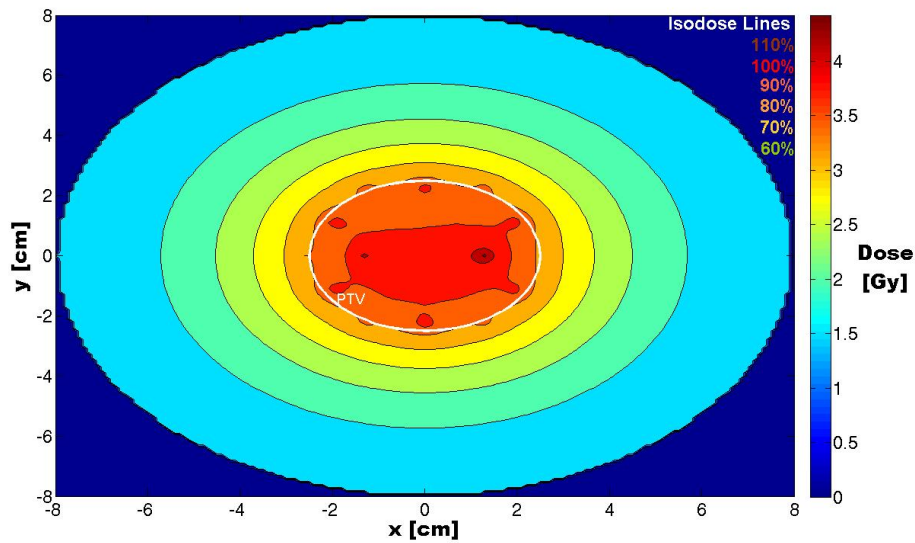


Figure 5.5: Isodose Plot from LP1 for Nineteen 10-curiel Infinite Catheters in 2-D

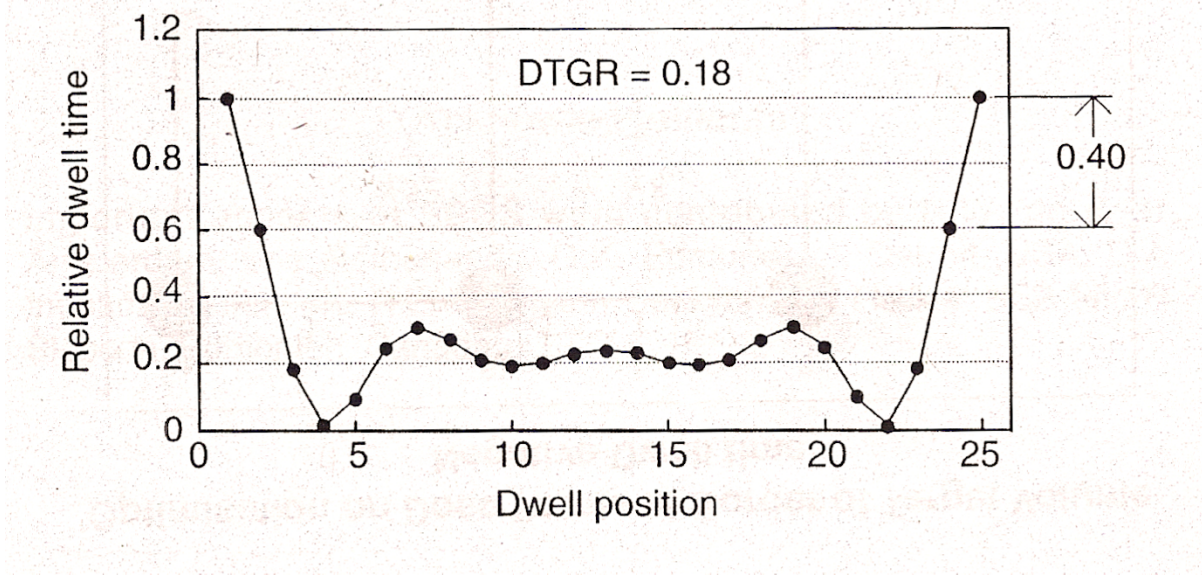


Figure 5.6: Symmetrical Dwell Time Pattern seen by the SSDS

brachytherapy optimization using the SSDS. This pattern is to have longer dwell times near the boundary of the target volume and shorter dwell times near the center, as seen in Figure 5.6 [5]. In this figure, the twenty-six dwell times have been normalized to the longest time, which is seen on the outermost position. Note that Figure 5.6 shows symmetry across the middle dwell position number thirteen. The DTGR in the figure stands for dwell time gradient restriction and simply reduces the difference between successive dwell times [5].

In comparison to the dwell time plot¹, LP1 decided to set the very central dwell position to zero to account for all other dose contributions to that point from other dwell positions. This symmetry is also apparent in the plane below the most upper plane for dwell positions four through seven. Positions four and seven near the edge of the PTV (refer to Figure 5.1), have dwell times of about 6.5 seconds, while positions of five and six have dwell times of around a quarter of a second.

The longest dwell time computed by LP1 was for dwell position 11, where the source dwells for 8.86 seconds. A dwell time of this length created a small hot spot at the location surrounding the dwell position as seen in Figure 5.5. Within this red region, the dose reaches

¹Courtesy of Nucletron International

4.42 Gy, and a smaller hot spot mirrors this position across the y-axis. One final note to make for LP1 is that the model took GAMS version 23.3 an execution time of 0.437 seconds on a Windows XP with an Intel Xenon CPU 5140 @ 2.33 GHz and 2 GB of RAM (see Table 5.2).

5.2.5 Linear Program #2

For a clinically acceptable treatment plan, the dose distribution must be of greater uniformity than the dose yielded by LP1. One option to help reduce hot spots and increase the dose uniformity is offered by a second linear program (LP2). As opposed to LP1, the second linear program shown in Equation 5.2 minimizes the integral dose to the normal tissue as the objective function. It also places a lower, α_L , and upper, α_U , bound on the dose to the PTV, which were set to 3.4 and 3.8 Gy, respectively:

$$\begin{aligned} \min \quad & \sum_{i,j} D_{ij} \quad \forall (i, j) \in Normal, \\ \text{subject to} \quad & D_{xy} = \sum_{n=1}^N T_n \dot{D}_{xy}^n \quad \forall (x, y), \\ & \alpha_L \leq D_{kl} \leq \alpha_U \quad \forall (k, l) \in PTV, \\ & T_n \geq 0 \quad \forall n. \end{aligned} \tag{5.2}$$

In the LP2 model, i and j are a subset of x and y , respectively, that include only the normal tissue. As mentioned before, this model seeks to remove the hot spots seen in the distribution of LP1. By placing an upper bound on the dose of 3.8 Gy, the dose uniformity can be narrowed to reduce the hot spots within the target volume that were apparent in the dose distribution of LP1. LP2 tries to smooth out the dose distribution to yield the prescribed dose everywhere in the target volume. Although we have placed an upper limit on the dose in the PTV, it is apparent by Figures 5.8 and 5.9 that the resulting dwell times do still have small regions of hot spots. However, the size of hot spot regions can be reduced, as will be shown in the succeeding plans.

Table 5.1: Optimized Dwell Times for each Linear Program: Centered PTV

Dwell Position	Dwell Time [seconds]			
	LP1	LP2	LP3	LP4
1	3.03	4.01	4.28	5.13
2	6.49	5.48	5.09	5.04
3	2.90	3.91	4.40	5.13
4	6.80	5.37	5.09	4.80
5	0.36	2.08	2.12	1.68
6	0.19	1.80	1.84	1.42
7	6.30	5.73	5.09	4.91
8	1.21	4.60	4.88	5.13
9	4.99	1.22	1.24	1.05
10	0.00	0.79	0.81	0.66
11	8.86	1.90	1.95	1.51
12	0.00	3.74	4.34	5.13
13	6.50	5.34	5.01	4.80
14	2.25	2.05	2.09	1.70
15	1.87	1.53	1.58	1.25
16	5.98	5.67	5.03	4.94
17	2.16	3.99	4.51	5.13
18	6.73	5.77	5.09	5.07
19	2.12	4.07	4.66	5.13

Table 5.2: Centered PTV: GAMS Execution Time for each Linear Program

Linear Program	Execution Time [seconds]
LP1	0.437
LP2	0.438
LP3	0.454
LP4	0.453

It is important to note that hot spots near source locations are unavoidable because of the depth-dose distribution curve, which peaks at, or very close to the source position (see Figure 5.7) [24]. Here, the percent depth dose (PDD) is plotted as a function of the y-axis of the brachytherapy seed, shown figure to the right of the plot. PDD is defined by the ratio of the dose at a given position to the maximum dose. Hence, when PDD is 100% the maximum dose is reached. Although the plot in Figure 5.7 does not show the PPD at $Y = 0$, the PDD would reach a plateau of 100% near the center of the source. In this case, the D_{max} , or 100% reference dose was measured at $X = 1.5$ mm and $Y = 0$, which is just under 1 mm outside the seed on the x-axis. The entire length of the seed shown in Figure 5.7b is 5 mm along the y-axis and

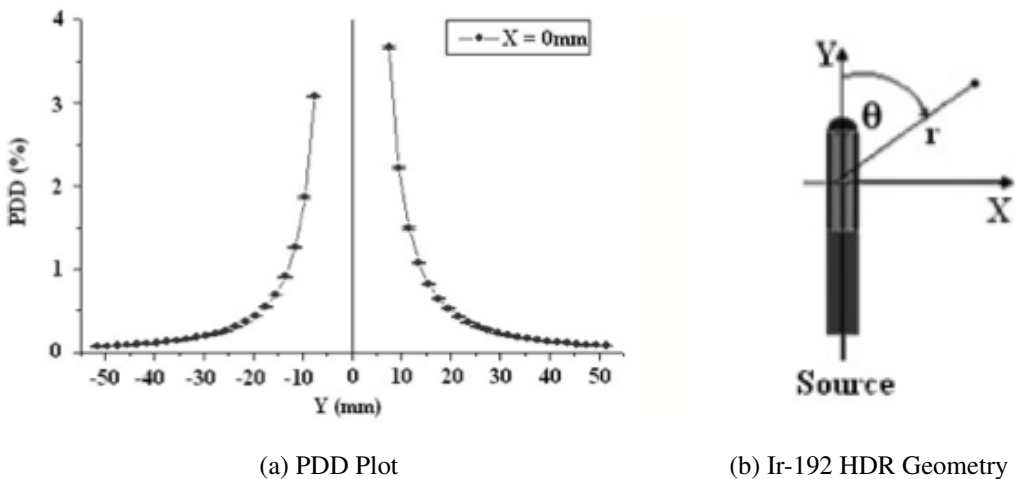


Figure 5.7: Percent Depth Dose Plot for Ir-192 and the Geometry of the Seed

the width is 1.1 mm along the x-axis [24]. The point of showing this figure is that very close to the source the dose reaches a maximum, and in order for a source position to contribute the correct dose distribution, it must dwell for a given amount of time causing its maximum dose region to create a hot spot.

For LP2 also note that the isodose plot of Figure 5.9 has a different dose color bar and percent isodose lines than does the isodose plot for LP1. This is simply due to automatic scaling by MATLAB. Since LP1 had no upper bound, the dose scale went larger and that is why the large hot spot regions occurred. In LP2 the hot spots still exist, but on a much smaller scale, extending only into the 110% range (3.74 Gy) and over small areas where the dwell positions reside.

Table 5.2 shows the dwell times for all dwell positions for LP2. An interesting pattern seen in the table is that the dwell times in each plane are fairly symmetric. For instance, dwell positions one through three have a dwell time of about 4 seconds for positions one and three and about 5.5 seconds at position two. This pattern is also notable in the next lower plane, where positions four and seven have a time of about 5.5 seconds and positions five and six have a time of about 2 seconds. This is a pattern that is typical with the stepping source dosimetry system [5]. Note the execution time for LP2 was 0.438 of a second.

5.2.6 Linear Program #3

As seen by the previous dose distributions, models LP1 and LP2 can lead to high local dose values (i.e. hot spots) because they tend to place the largest amount of dwell time on the positions that deposit a large percent of their integral dose in the tumor. The results became problematic in LP1 because few non-zero dwell positions were selected and their times were somewhat large. Although LP2's dose distribution is more uniform than LP1, it did still result in hot spot regions. Therefore, the next two linear programs seek to remove these hot regions to increase uniformity.

A solution for this dilemma proposed in Shepard *et al.* is to place an upper limit on the ratio between the maximum dwell time and the average dwell time as shown in Figure 5.3 [6]. β

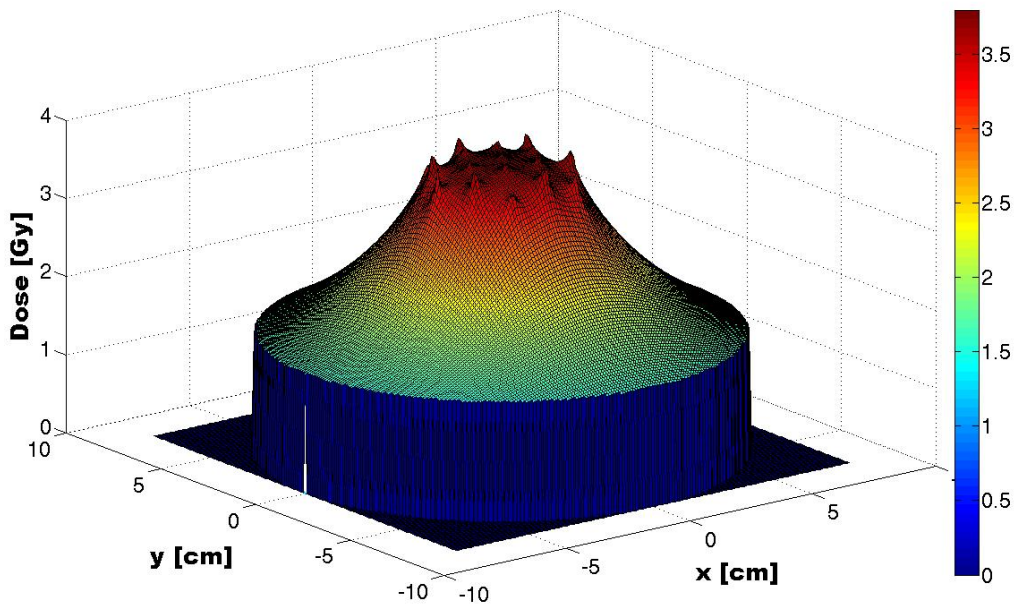


Figure 5.8: Dose Distribution from LP2 for Nineteen 10-curie Infinite Catheters in 2-D

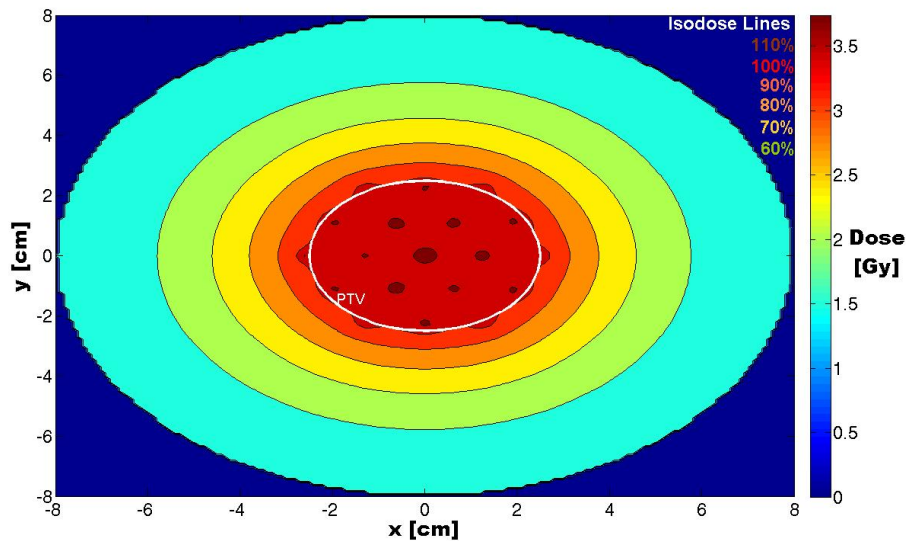


Figure 5.9: Isodose Plot from LP2 for Nineteen 10-curie Infinite Catheters in 2-D

is the factor greater than the average dwell time that places an upper bound on all dwell times and was set as 1.4. Here positions p and q are aliased:

$$\begin{aligned}
 \min \quad & \sum_{i,j} D_{ij} \quad \forall (i,j) \in Normal , \\
 \text{subject to} \quad & D_{xy} = \sum_{n=1}^N T_n \dot{D}_{xy}^n \quad \forall (x,y) , \\
 & \alpha_L \leq D_{kl} \leq \alpha_U \quad \forall (k,l) \in PTV , \\
 & T_p \leq \frac{\beta}{N} \sum_{n=1}^N T_n \quad q = 1, 2, \dots, N , \\
 & T_n \geq 0 \quad \forall n .
 \end{aligned} \tag{5.3}$$

As seen in Figure 5.11, the dwell-time upper bound decreases the hot spot region of LP2 in the outer edges of the PTV. However the hot spots in center of the target volume still remain. The symmetric dwell time pattern in each plane is even more apparent in this linear program, as shown in the LP3 column of Table 5.2. That is, symmetric dwell positions have very similar dwell times, such as with positions two and eighteen with a dwell time of 5.09 seconds.

Although the solution of LP3 is quite uniform and conforms to the PTV fairly well, we will seek greater perfection by exploring another linear program. Again, the goal is to reduce the hot spots in the dose distribution of LP3 by modifying our linear model. As a final note on LP3, the execution time to optimize the dwell times was 0.454 of a second.

5.2.7 Linear Program #4

Since in the last attempt an additional constraint did not reduce all of the hot spot regions, the next linear model will modify the objective function of LP3. The final linear model, LP4, displayed in Equation 5.4 is a mini-max model that minimizes the maximum deviation from the prescribed dose in the PTV. The same constraints are used as in the third linear program. The LP4 model in its entirety is as follows:

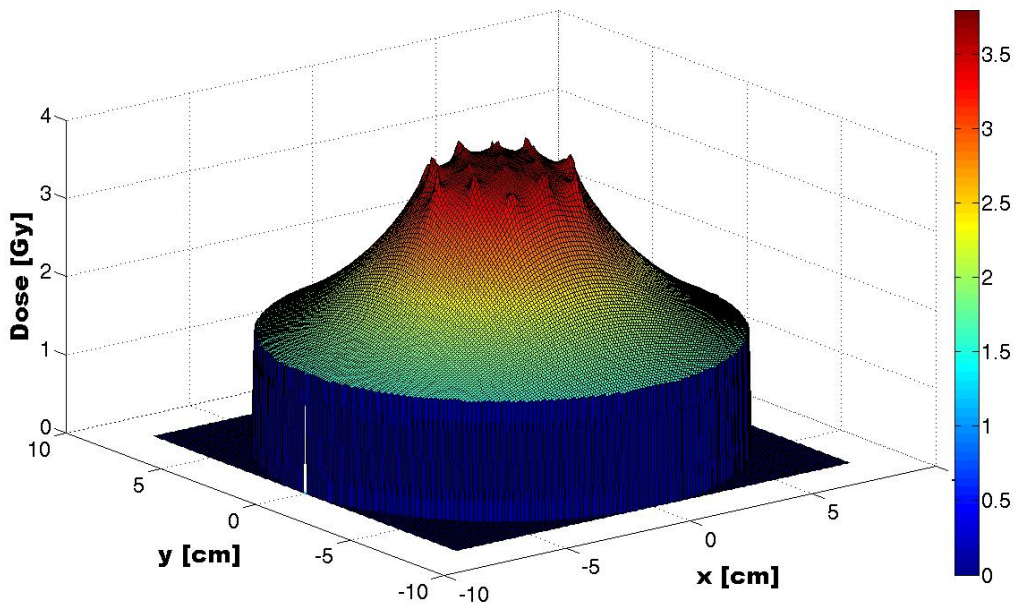


Figure 5.10: Dose Distribution from LP3 for Nineteen 10-curie Infinite Catheters in 2-D

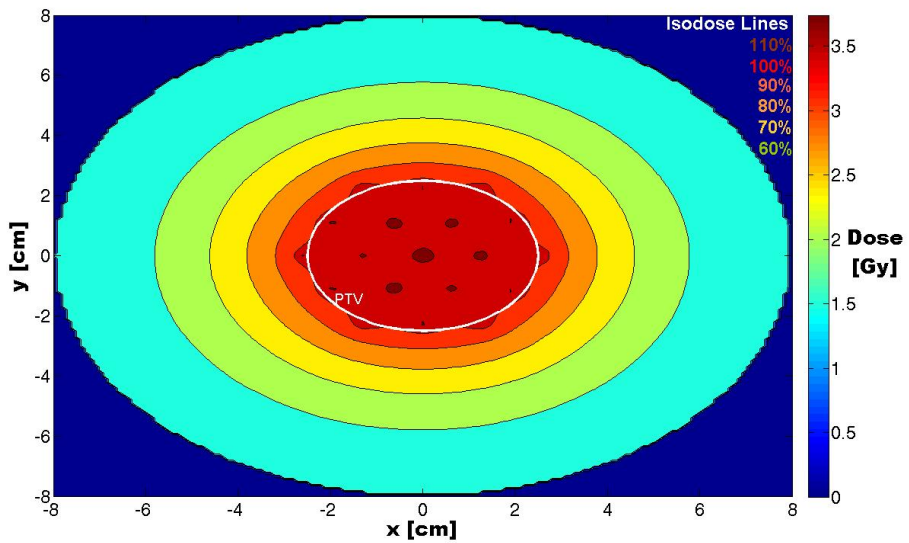


Figure 5.11: Isodose Plot from LP3 for Nineteen 10-curie Infinite Catheters in 2-D

$$\begin{aligned}
& \min && \max_{(k,l) \in PTV} |D_{kl} - D_p|, \\
& \text{subject to} && D_{xy} = \sum_{n=1}^N T_n \dot{D}_{xy}^n \quad \forall(x, y), \\
& && \alpha_L \leq D_{kl} \leq \alpha_U \quad \forall(k, l) \in PTV, \\
& && T_p \leq \frac{\beta}{N} \sum_{n=1}^N T_n \quad q = 1, 2, \dots, N, \\
& && T_n \geq 0 \quad \forall n.
\end{aligned} \tag{5.4}$$

As shown in Figures 5.12 and 5.13, the dose is flattened across the PTV with this model, which is highly desirable. Clearly, the hot spots that resulted from LP3 have been greatly reduced throughout the PTV, even in the center. Although the conformity is not precisely in a circular shape, the parts that extend beyond the PTV cover little area. It is safe to say that LP4 has generated the best dose uniformity and conformity, as well as over all treatment plan. The dwell times associated with LP4 are shown in Table 5.2. GAMS's execution time for LP4 was 0.453 seconds.

Much like the dwell times shown from LP3, those of LP4 consist of the same symmetric pattern. One characteristic common of all four linear programs is that they placed a very small amount of time in the dwell position in the center of the PTV, position ten. The second, third, and forth linear programs all emphasized longer dwell times on the outer dwell positions in the PTV.

For ease of comparison, the isodose plots for each linear program are displayed in one plot in Figure 5.14. Note the dose color bar in Figure 5.14 are on different scales for each linear program. From this figure, it is clear how each linear program becomes progressively better at removing hot spots and therefore gaining uniformity, with the forth linear program proving superior.

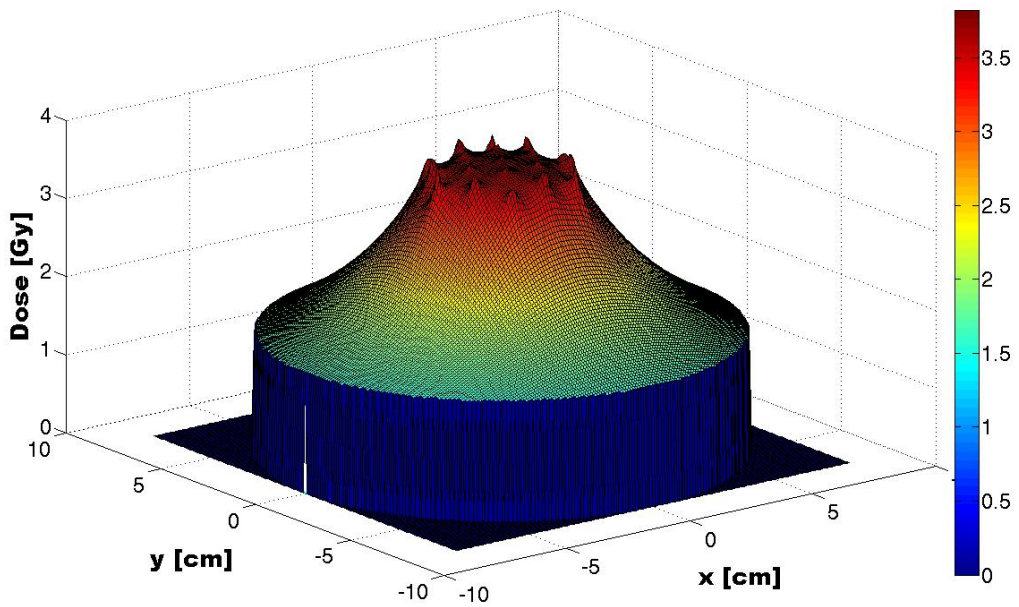


Figure 5.12: Dose Distribution from LP4 for Nineteen 10-curie Infinite Catheters in 2-D

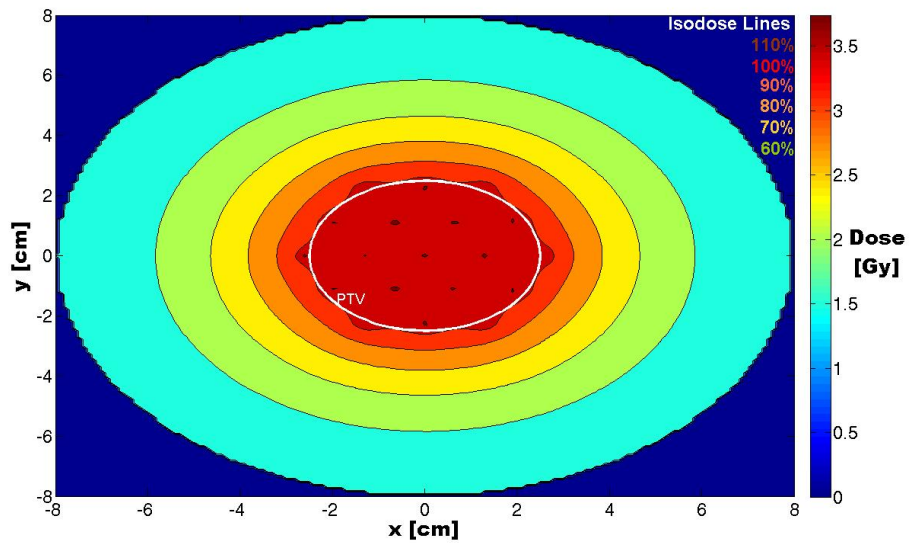


Figure 5.13: Isodose Plot from LP4 for Nineteen 10-curie Infinite Catheters in 2-D

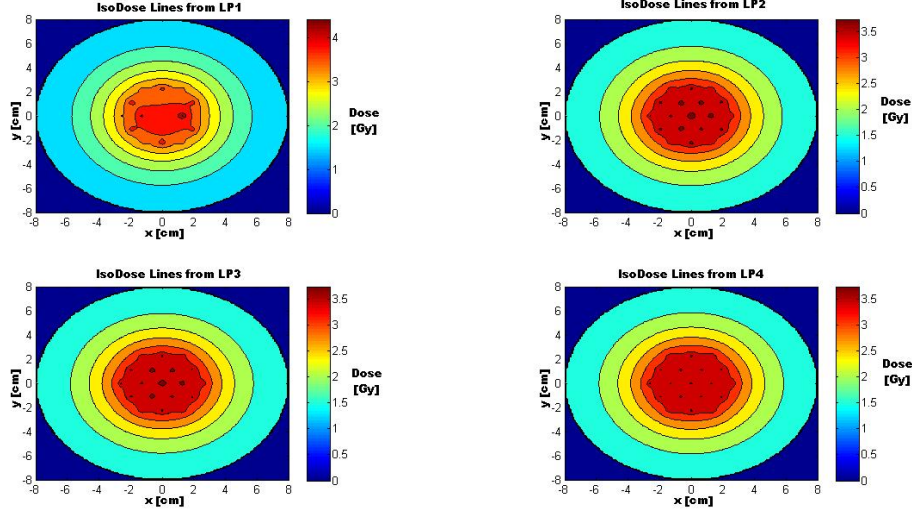


Figure 5.14: Isodose Plots for all Four Linear Programs

Previous high dose-rate brachytherapy treatment plans optimized following the SSDS have demonstrated that longer dwell times at the outer target volume positions and less time at the inner positions will result in a dose distribution with greater uniformity. Clearly this result has been confirmed by optimizing a source distribution generated using the Green's function kernel. We now aim to compare the results of the dose distribution to those resulting from the radiation transport equation using a Monte Carlo N-Particle (MCNP) code.

5.3 Comparison to the Transport Equation via MCNP

In order to perform verification with MCNP, the most ideal linear model, LP4, was chosen to do the comparison of the transport equation to the diffusion equation results. The geometry discussed in Figure 5.1 was implemented in MCNP via the surface and cell cards. An importance of one was set for all cells of the geometry except for outside all cells (the boundary), where an importance of zero was defined. The materials used for all cells with an importance of one were deemed water. As ^{192}Ir is a pure gamma emitter, the mode for MCNP was set to tracking photons and electrons.

The relevant source definition inputs included the energy, particle type, and spatial distribution. As expected, the particle energy was set to 0.380 MeV for photons. The spatial distribution permitted a point source allocation. All of the spatial positions were defined for the 19 dwell positions. The dwell times for each point source, or dwell position, were implemented via source probability.

A *F4 tally, which is an energy cell fluence, was recorded for one million particle histories. This number of particle histories was sufficient according to the statistical results of the simulation. The *F4 tallies were multiplied by a table of mass energy absorption coefficients acquired from the National Institute of Standards and Technology (NIST) website. The resulting units for fluence values were $\frac{\text{MeV}}{\text{g}}$, which was simply converted to units of gray. *FMESH4 tallies were used in order to generate two and three-dimensional plots for ease of comparison to the diffusion results.

The dwell times from Table 5.1 optimized with LP4 were implemented into an MCNP input file as the source probabilities at each dwell position. The MCNP code was run for one million particle histories and mesh tally results were converted to gray. Clearly, the MCNP plots portray completely different results than do the diffusion results. The peaks for each point source are very well defined and narrow in the MCNP plots. There are many reasons for this difference. First, diffusion theory assumes that the medium has a much greater probability of scattering compared to absorbing. For photons of 380 keV, the mass absorption coefficient is 0.0326 $\frac{\text{cm}^2}{\text{g}}$, whereas the mass scattering coefficient is 0.1084 $\frac{\text{cm}^2}{\text{g}}$. Hence, the scattering probability is about 3.3-times greater than that of absorption. Unfortunately, there exists no solid definition on how much greater the scattering probability must be for validation of diffusion theory. However, the fact that scattering occurs over three times more often than absorption leans in favor of diffusion validity.

A second reason for inconsistent results is that the Green's function solution yielding these results was solved strictly as a one-energy-group problem. The MCNP solution is exactly opposite. Although both solutions use the initial, average photon energy of 380 keV, the MCNP code accounts for down-scatter of photons to lower energy groups at which they are absorbed.

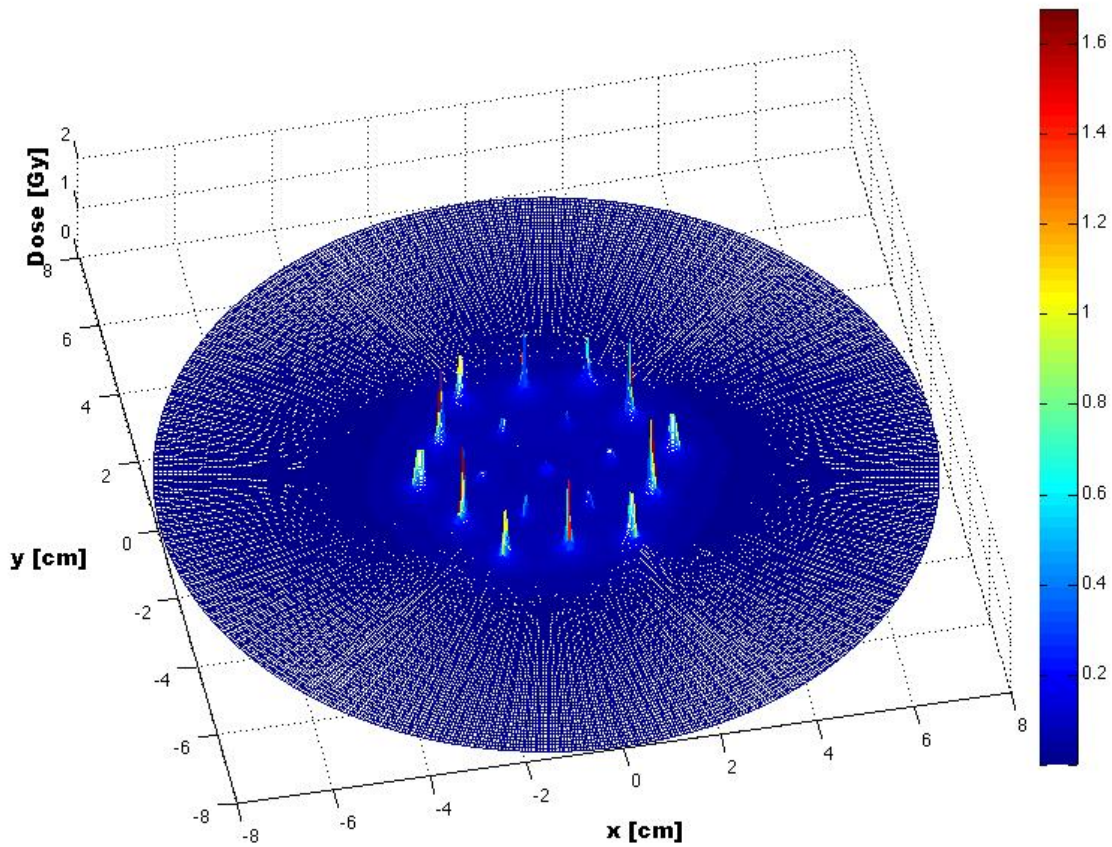


Figure 5.15: MCNP Dose Distribution from the LP4 Optimized Dwell Times

The diffusion solution assumes that all photons absorbed are at the same energy 380 keV. Since the absorption probability goes up with decreasing photon energy, the diffusion solution results in all photons (even after being scattered) to be absorbed with low probability when compared to that of lower energy photons. A one energy group solution will also cause the dose to appear larger than in actuality because energy is a term in the dose calculation of charged particle equilibrium. Hence, this could be why the dose is so much smaller in the results of the MCNP simulation.

A third reason for difference in results is because the Green's function solution is for two dimensions and the MCNP results are for three dimensions. The ^{192}Ir has gamma source emissions of 380 keV with a mean-free path of about 9 centimeters. Hence, dose is likely to be

distributed from the source in the z-direction, of which we can only see one slice. For a valid comparison, a three-dimensional Green's function would be required for the optimization routine with an objective to distribute a uniform dose to a volume as opposed to a surface in two dimensions. Of course in order to make a valid comparison with MCNP, we would need to develop a three-dimensional, multi-energy group dose kernel.

5.4 2-D Dose Optimization for the Current Density Condition: Offset PTV

In most situations a PTV will not actually be centered in a geometry as simulated in the previous optimization routine. Therefore, the next simulation will offset the PTV by four centimeters in the y-direction, making it closer to the boundary. The boundary and PTV radius will be the same as the previous and a five-plane triangular geometry will again be used for the catheters. The catheters will be shifted along with the PTV in the same orientation. The new setup is shown below in Figure 5.16.

Again the catheters are marked by the green x's, while the boundary for the PTV and breast are in blue and red, respectively. The catheter spacing is the same at 1.3 centimeters and the five-plane geometry has labeled the dwell positions (catheters) in the same order. It is required that all dwell positions must be at least 1.5 centimeters from the skin surface, as noted in the chapter on HDRBT procedure. Keeping that in mind, the distance between position 1 and the surface (and hence position 3 and the surface) has been verified as 1.615 cm.

5.4.1 Unoptimized Dose Distribution: Offset PTV

With the shift toward the boundary, each position's dose kernel will be substantially different than it was with the PTV centered at the origin. Since the PTV will be closer to the edge of the boundary in this geometry, a significant loss of radiation will escape the domain from the dwell positions in the upper planes. To account for this, longer dwell times will need to be assigned at these positions. Hence, another consequence of the offset geometry is that the dwell time symmetry pattern will not exist across the $y = 4$ plane. However, symmetry will maintain across the $x = 0$ plane since the geometry was shifted only along the y-axis.

The simulation with the offset geometry will be used to explore which linear program is most effective for dose uniformity and conformity. This point was exemplified with the previous geometry. By using an offset PTV, we can determine the most optimal linear program when the sources are near a boundary. With some minor modifications to the previous GAMS model, the shifted target volume voxels can be implemented into a new model. After each new dose kernel has been generated based on its new dwell position, the matrices can be output into GAMS for dwell time optimization.

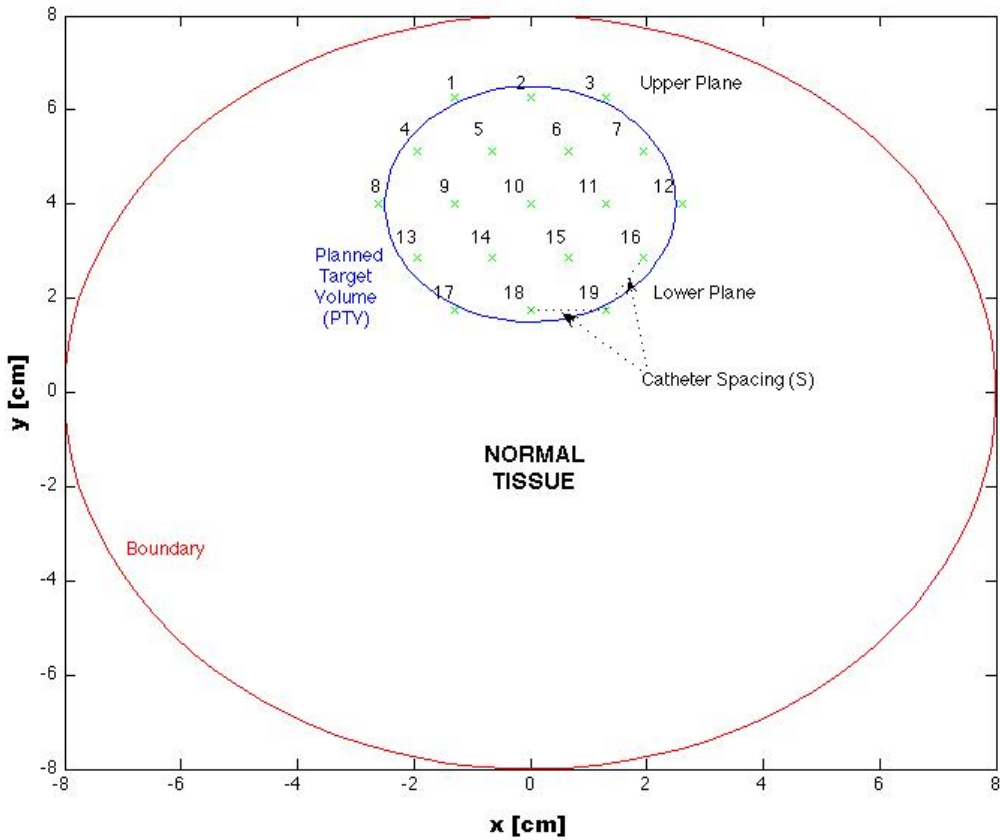


Figure 5.16: Five-Plane Triangular Geometry for Offset PTV

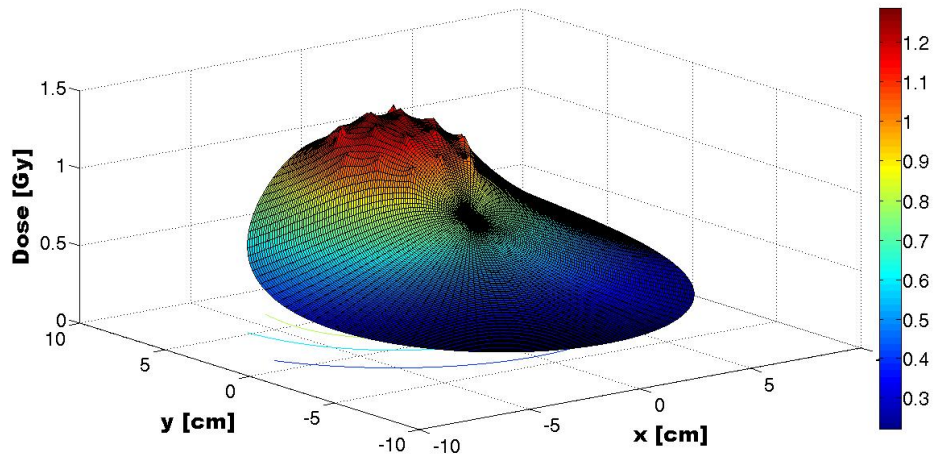


Figure 5.17: Unoptimized Dose Distribution for the Offset PTV in 5-Plane Geometry

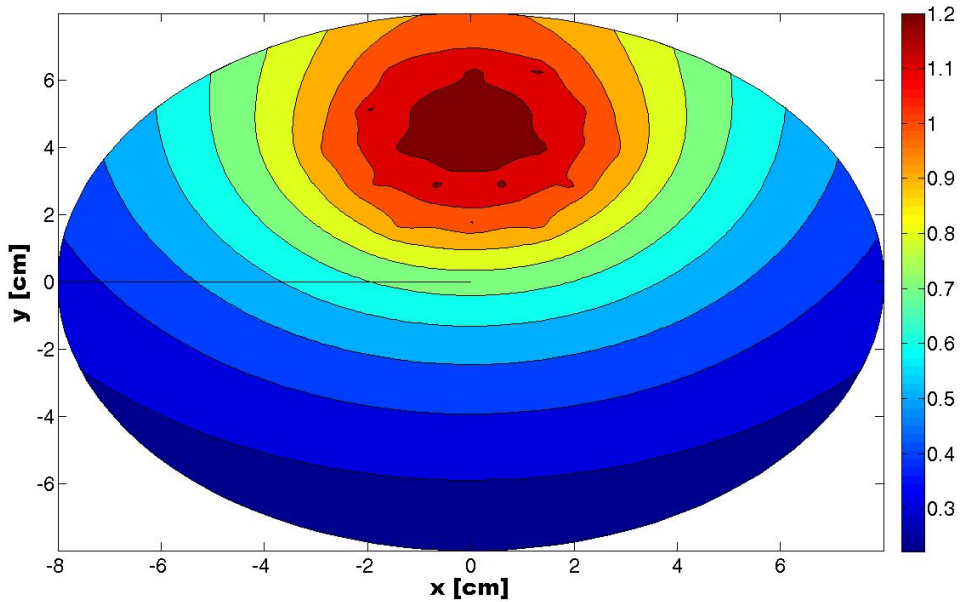


Figure 5.18: Unoptimized Isodose Plot for the Offset PTV in 5-Plane Geometry

5.4.2 LP#1: Offset PTV

The model for LP1 uses the same objective function and constraints as with the centered PTV geometry. The dose distribution for LP1 is shown in Figure 5.19 and the isodose plot is displayed in Figure 5.20. A large hot spot region is apparent in the lower part of the PTV, making the dose uniformity of LP1 very poor. The poor dose uniformity is consistent with the results found for LP1 with the centered PTV. The dwell times for LP1, shown in Table 5.3, do not possess a great deal of symmetry across the y-axis and are zero seconds for five out of the nineteen positions. With this many dwell times set to zero, several of the nonzero positions are chosen to be mildly large, leading to non-uniformity. Although LP1's dose uniformity is poor, the dose conformity to the PTV region is good. However, we would like to increase the dose uniformity by exploring the other three linear programs. Note the execution times for GAMS are shown in Figure 5.4 at the end of the chapter for the offset geometry and that they are of the same order of magnitude as those of the centered geometry.

5.4.3 LP#2: Offset PTV

LP2 places an upper bound on the dose to the PTV region. The model is shown in Equation 5.2 and as before, the upper bound on the dose to the PTV region is 3.8 gray. Figures 5.21 and 5.22 show that this upper bound has increased the y-axis symmetry of the dose distribution. The distribution from LP2 generates fairly good dose conformity to the PTV. Still, because the dose uniformity within the PTV is not ideal, we seek to reduce the hot-spot regions by placing an upper limit on the dwell times.

5.4.4 LP#3: Offset PTV

Since the dwell times for the offset geometry are vastly different for positions in the center compared to positions near the edge of the boundary, we must modify our constraint parameters in LP3 and LP4. Namely, the value that sets an upper limit on the dwell time must allow for a greater deviation from the mean because the dwell times in the upper plan will be much longer than others. Hence the parameter β given in models LP3 and LP4 by Equations 5.3 and 5.4,

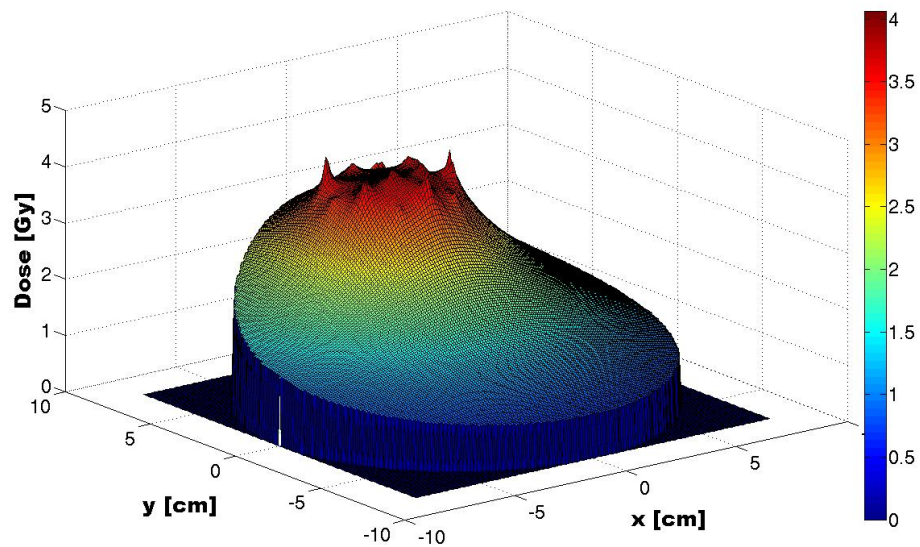


Figure 5.19: LP1 Dose Distribution for the Offset PTV in 5-Plane Geometry

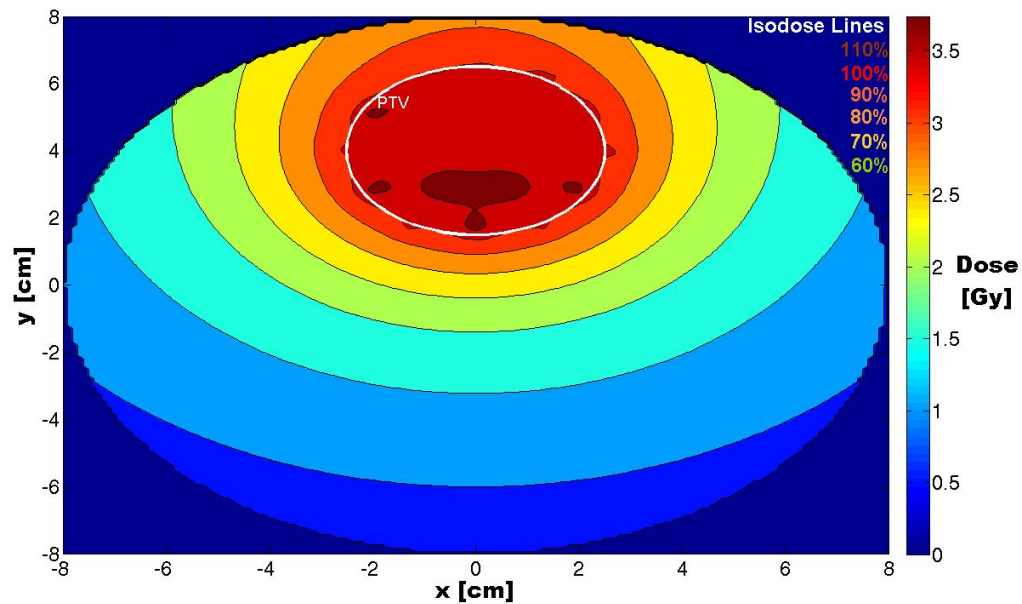


Figure 5.20: LP1 Isodose Plot for the Offset PTV in 5-Plane Geometry

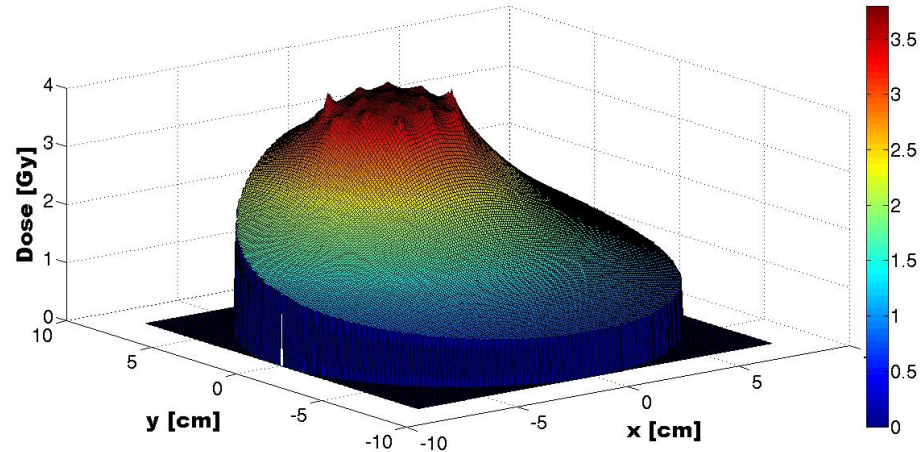


Figure 5.21: LP2 Dose Distribution for the Offset PTV in 5-Plane Geometry

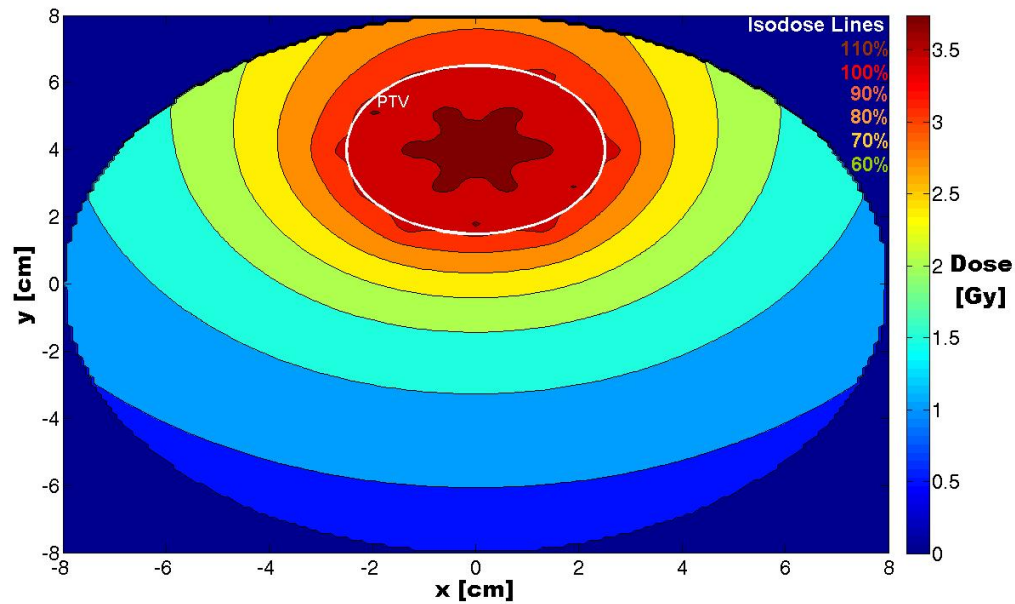


Figure 5.22: LP2 Isodose Plot for the Offset PTV in 5-Plane Geometry

respectively, must be increased from 1.4 to 1.6 for LP3 and to 1.8 for LP4 in order to avoid an infeasible model.

Unfortunately as seen in Figures 5.23 and 5.24, the hot spot regions did not diminish from the upper bound on the dwell times. In fact, the dose distribution from LP3 is nearly identical to that of LP2. However, when comparing the dwell times between the two linear programs, as seen in Table 5.3, LP2 and LP3 do not yield the same dwell time distribution. Again the dose distribution conforms well to the PTV and is symmetric about the y-axis. Our next attempt to remove the hot spot region from the PTV is by modification of the objective function.

5.4.5 LP#4: Offset PTV

By minimizing the maximum deviation from the prescribed dose in the PTV as an objective, the hot spot region of LP2 and LP3 has been greatly reduced. However, the increase in dose uniformity in the PTV has sacrificed the normal tissue surrounding the PTV. The area of great concern is the dose to the boundary region, which represents the skin. Since the objective function of LP4 no longer is concerned with minimizing the dose to the normal tissue region, the isodose reaching the boundary is now at 90% of the prescribed dose, whereas with LP2 and LP3 it was at 80%. Also the prescribed isodose line (100%) now extends beyond the target volume, yielding poor conformity to the tumor.

5.4.6 Concluding Remarks on the Offset and Centered PTV Optimization

The four linear programs outlined for a centered PTV with five-plane triangular geometry were put to the test by offsetting the PTV four inches in the y-direction. For ease of comparison, the isodose plots from each LP are juxtapose in Figure 5.27. Striving to achieve good dose uniformity and conformity, it was determined that the objective functions explored in the former linear programs did not allow for both goals simultaneously. LP2 and LP3 provided good dose conformity by minimizing the dose to the normal tissue, which yielded a low dose to the boundary or skin region. However, the uniformity of the dose was not as remarkable

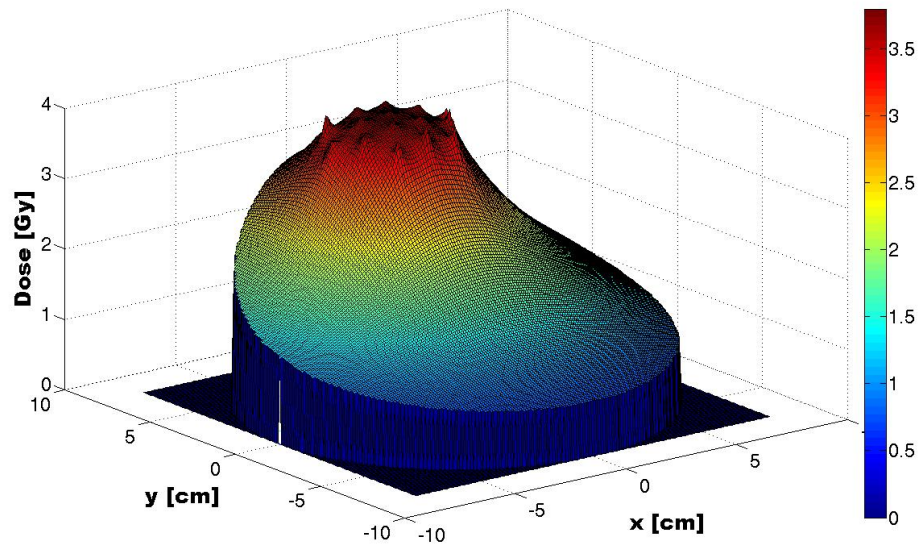


Figure 5.23: LP3 Dose Distribution for the Offset PTV in 5-Plane Geometry

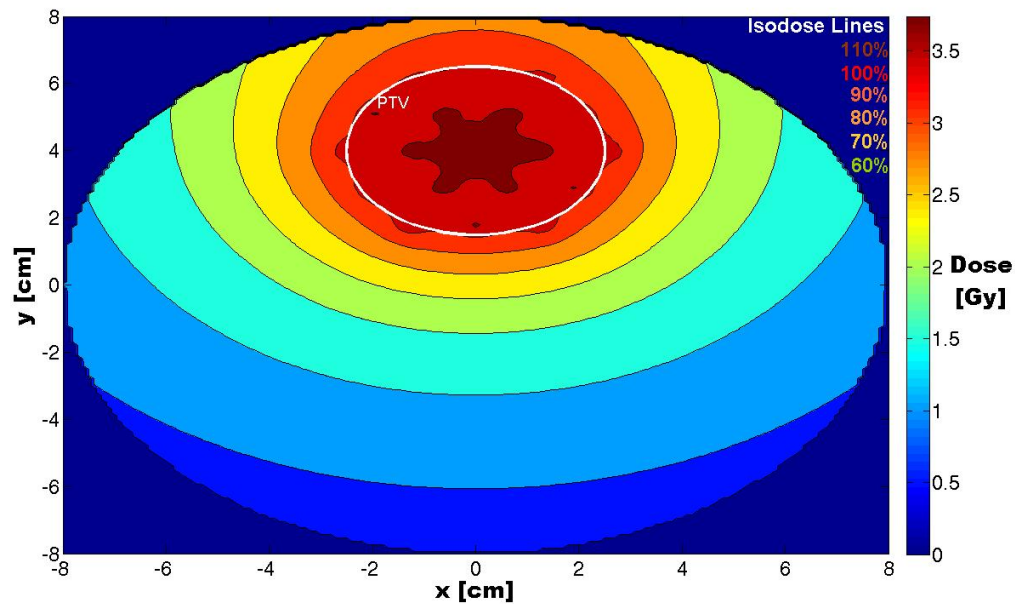


Figure 5.24: LP3 Isodose Plot for the Offset PTV in 5-Plane Geometry

Table 5.3: Optimized Dwell Times for each Linear Program: Offset PTV

Dwell Position	Dwell Time [seconds]			
	LP1	LP2	LP3	LP4
1	1.82	1.84	1.95	5.23
2	3.79	2.04	1.99	2.39
3	2.10	2.11	2.02	4.40
4	6.83	4.19	4.03	2.62
5	0.00	2.56	2.57	0.82
6	0.00	2.65	2.65	0.73
7	6.44	3.63	3.54	4.14
8	2.74	4.03	4.20	5.99
9	0.00	2.01	2.02	1.13
10	0.00	0.95	0.95	0.59
11	0.00	2.43	2.33	1.34
12	3.00	4.63	5.18	5.99
13	7.63	5.42	5.24	5.06
14	3.87	1.87	1.86	1.34
15	3.88	1.87	1.86	1.49
16	7.51	4.42	4.34	3.63
17	2.45	5.09	5.24	5.99
18	7.22	5.00	4.99	4.34
19	2.46	5.38	5.24	5.99

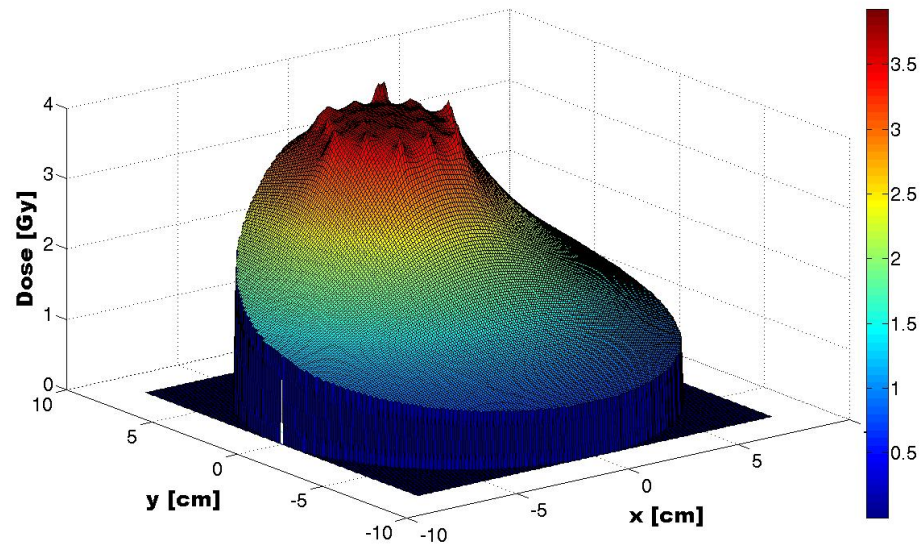


Figure 5.25: LP4 Dose Distribution for the Offset PTV in 5-Plane Geometry

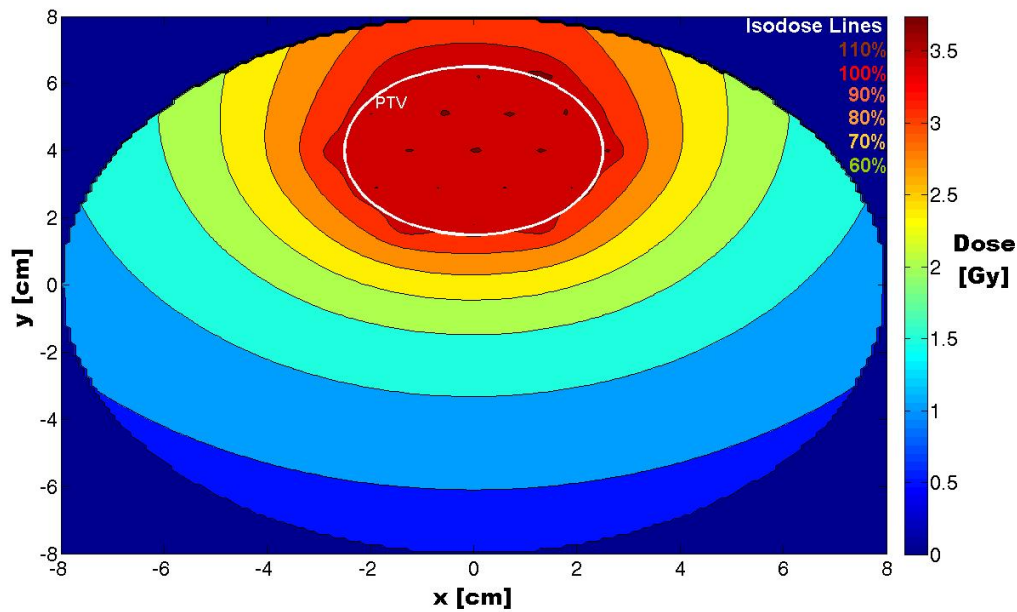


Figure 5.26: LP4 Isodose Plot for the Offset PTV in 5-Plane Geometry

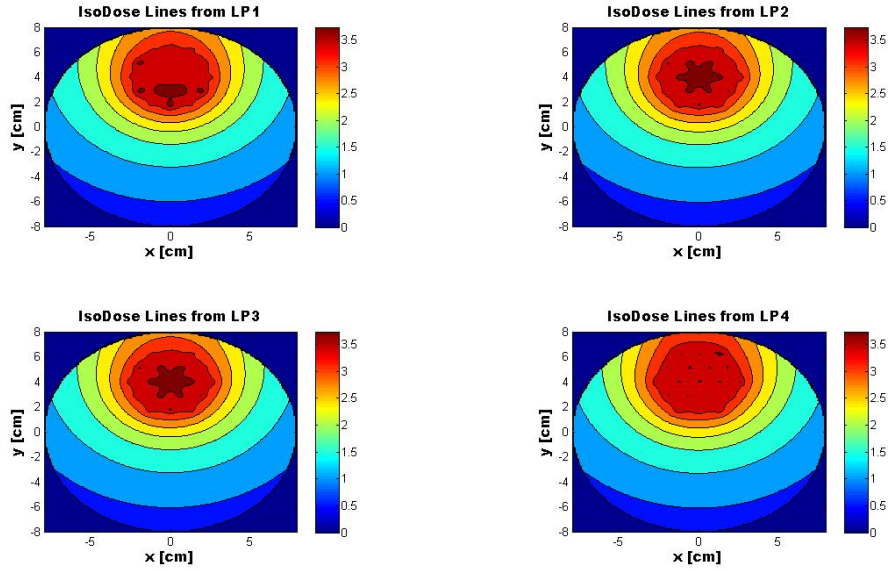


Figure 5.27: Isodose Plot of all 4 Linear Programs for the Offset PTV in 5-Plane Geometry

since a hot spot in the center of the PTV reached the 110% isodose line. Modifying the objective function, the deviation from the prescribed dose was minimized in LP4, but only leading to a larger dose in the normal tissue, namely to the skin. Model LP4 essentially sacrificed dose conformity to gain uniformity, as its objective was no longer concerned with the dose to the normal tissue. Since the skin is such a sensitive area to receiving radiation burns, the dose distribution from LP4 is not the ideal optimization model for a PTV in close proximity to the epithelium. For this geometry of a PTV, our results show that LP3 is the best candidate for dwell time optimization. LP3's results are nearly identical to LP2, but since the LP3 model contains an additional, upper-bound constraint on dwell times that disallows them from being greater than β times the average dwell time, LP3 will hold the advantage in the case when more dwell positions are introduced into the geometry. Although a hot spot region exists for LP3, it is not an extreme overdose of the PTV, as it only reaches 3.74 gray. Moreover, it is not uncommon that isodose lines for HDR brachytherapy reach the 150% to 200% level in very small regions of the PTV surrounding the catheters [3]. Of course more linear programs could

Table 5.4: Offset PTV: GAMS Execution Time for each Linear Program

Linear Program	Execution Time [seconds]
LP1	0.422
LP2	0.437
LP3	0.437
LP4	0.453

be explored in addition to the four described here, but if a potential treatment planning software would summon a optimization model among these four linear programs, it would use choose LP3 for an offset PTV and LP4 for a PTV centered in a geometry.

The next logical question would be whether these linear programs could compete with the efficiency of current treatment planning systems. Considering the usage of GAMS to optimize the dwell times for the four linear models presented here, using the presented linear models would be very efficient as an optimization package, since it solved each LP in about one half of a second. Although a more realistic dose optimization package would require a three dimensional dose kernel with hundreds of dwell positions (variables), GAMS is very capable of solving large linear programs in a few minutes or less. With the dose matrices pre-stored in a database so that could be called upon for a given set of dwell positions, the efficiency of a system interfacing Green's function kernels with GAMS's optimization software would be very competitive with today's treatment planning software.

Chapter 6

Conclusions

The time-independent diffusion equation has been solved via the Green's function technique for several types of boundary conditions. Solutions were generated for the Dirichlet, Neumann, and Robin conditions, with the case of the Robin condition being of interest. The Robin condition forced the flux solution to have no particles entering the domain from beyond the boundary and is called the partial current density solution. The current density Green's function kernel for the flux is converted to dose by assuming charged particle equilibrium. Using this solution, dose kernels can be generated for a source distribution (i.e. several dwell positions) with each position having a unique dose kernel. Due to the small size of a HDR brachytherapy source, the seed has been approximated by a point source and a distribution of dwell positions maps out the source locations. Performed in two dimensions, an optimization routine using several sets of objective functions and constraints has been applied to the dose matrices of each dwell position, allowing for output of optimal dwell times at each dwell position. An interface between MATLAB and GAMS has been made use of in order to complete this task.

6.1 PTV Centered at the Origin

For a geometry with a planned target volume centered at the origin of an eight centimeter in radius circle, a five-plane triangular setup consisting of nineteen catheters yields our source distribution of dwell positions. Four different linear programs were used to optimize dose distribution within the PTV. Looking for both dose uniformity and conformity to the target,

the linear programs were compared based on their ability to accomplish this goal. The first linear program, LP1, that minimized the integral dose to the entire domain resulted in poor dose uniformity, but fairly good conformity. The second linear model, LP2, placed a lower and upper limit on the dose within the PTV while minimizing the dose to the normal tissue region. Hoping to reduce hot spot regions of the first linear program, LP2 succeeded at increasing the dose uniformity, while still maintaining the prescribed dose conformity to the PTV. However, the uniformity of LP2 could still be improved, since there were still hot spot regions. LP3 strived to further reduce the overdosed regions by placing an upper limit on the dwell time deviation from the average dwell time. With the same objective function as LP2, the additional constraint helped to reduce the hot spots on the outer regions of the PTV, yet the ones in the center remained. In hope to gain more uniformity, LP4 modified the objective function by minimizing the maximum deviation from the prescribed dose in the PTV. LP4 was successful at greatly reducing all of the hot spot regions, while maintaining conformity of the prescribed isodose line around the PTV. Indeed, the forth linear model was deemed most effective at achieving both dose uniformity and conformity for a PTV centered at the origin of a circular boundary.

The resulting dwell times from LP4 applied to the centered PTV were input into a Monte Carlo N-particle simulation in order to compare the diffusion approximation results to the actual radiation transport equation. The diffusion results differed from the MCNP results for three major reasons. First, the assumptions behind diffusion theory make it valid only for a highly scattering medium. Second, the Green's function solution was solved as a one-group model, whereas MCNP uses multiple energy groups for its analysis. This caused the peaks of the point sources from diffusion theory to spread out and distribute their dose to a greater distance because it did not account for photon down-scattering. Finally, the Greens function was developed for a two dimensional analysis and optimization. In the three-dimensional MCNP model, the dose distribution was volumetric. In order to make a better comparison between diffusion and transport results, a three-dimensional Green's function would need to be used

and optimized for a geometry. Only then could a more accurate comparison be made between the two models.

6.2 PTV Offset from the Origin

Since in most cases the PTV will not be centered within a volume, a geometry was explored for a PTV offset in the y-direction by four centimeters. Again the same four linear programs were applied to the geometry to seek the the most optimal model. This time, LP3 generated the best results. This was mainly due to LP4's objective function being unconcerned with the dose to the normal tissue and strictly with the dose to the PTV. The consequence for LP4 was that too much dose (90% of the prescribed dose) reached the boundary, which represents the skin. However, the dose uniformity within the PTV for LP4 was the best out of the four models. With that, the large dose to the boundary and the prescribed dose stretching outside the PTV deemed LP4 to result in poor conformity. On the other hand, LP3 had excellent conformity to the PTV with its prescribed isodose line. Although a hot spot existed in the center of the PTV for LP3, the region was not excessively large and the dose value only reached 110% of the prescribed dose. Good dose conformity and fair uniformity essentially deemed LP3 the best of the four linear models explored in this work for a PTV near a boundary.

6.3 Future Work

The research here has shown that dose optimization can be performed for a two-dimensional Green's function solution to the time-independent diffusion equation. Although the two-dimensional solution may not be accurate in the dose distribution that it yields as hinted by the MCNP comparison, it is a start in the direction of a more complex and more accurate solution. Future work could involve developing a three-dimensional Green's function dose kernel and eventually using a multi-energy group method. This would compare to a much greater extent with the results from a MCNP simulation. Using the three-dimensional, multi-group Green's function solution and applying a source distribution, the dose kernels could be

output into GAMS or some other optimization software for dose optimization in a similar fashion that was performed here in two-dimensions. In addition, if a step function was used in the z-direction for each source, the brachytherapy seeds could be modeled by a line source, which better approximates the HDR source than a point source. Research being performed on directional brachytherapy sources could also find an application of the Green's function dose method, by generating a kernel that emits anisotropically. However, since the diffusion equation handles only isotropic sources, it would need to be coupled with the first collided source method in order to handle a directional source.

Another extension to the Green's function solution could be the implementation of an albedo or reflection coefficient. In math terms, the definition of the albedo, α , is given below in Equation 6.1 [9]:

$$\alpha = \frac{J_-}{J_+} . \quad (6.1)$$

This work has assumed a zero albedo since no photon current from beyond the boundary was allowed to re-enter (i.e. $J_- = 0$). However, in reality the chest wall sits below the PTV for breast brachytherapy, introducing a non-homogeneity that would cause scattering and some quantity of reflected photons. To account for the re-entering photons, an albedo could be generated based off of the definition given above. If the albedo is known for the boundary along the chest wall, then a multi-region problem would not be required to get the solution of the flux (and hence the dose) profile. The albedo would essentially provide a boundary condition for the region bordering the chest wall and therefore accounting for the dose contribution from the reflected photons.

A final modification to this work's approach could be to use the actual decay scheme spectrum for ^{192}Ir . Here, we have used only the average energy (380 keV) of photons emitted by the isotope ^{192}Ir , but in reality there are several emissions with energies ranging from 136 to 1060 keV [1]. It has been shown that using the average energy yields a dose distribution that compares well with the absolute spectrum up to a certain distance away from the source [24]. This is because the actual spectra will see higher-energy photons reaching distances further from the source before interaction.

If the three-dimensional Green's function solution were generated, then a treatment planning software could be based off of it. As suggested before, a database could store all of the dose kernels for several types of HDR brachytherapy setups (i.e. n-plane catheters) and boundary dimensions. Since the solution for the dose kernel is the most time consuming part of using this technique for dwell time optimization, having the dose kernels pre-saved will make the process very efficient. The very efficient optimization software could then easily compete with today's treatment planning software.

LIST OF REFERENCES

- [1] E. J. Hall, *Radiobiology for the Radiologist*. Philadelphia, PA: J. B. Lippincott Company, 4th ed., 1994.
- [2] L. L. Kestin, D. A. Jaffray, G. K. Edmundson, A. A. Martinez, J. W. Wong, V. R. Kini, P. Y. Chen, and F. A. Vicini, “Improving the dosimetric coverage of interstitial high-dose-rate breast implants,” *International Journal of Radiation Oncology*Biology*Physics*, vol. 46, pp. 35–43, 2000.
- [3] M. R. Arnfield, L. Peck-Sun, M. A. Manning, D. W. Arthur, B. D. Kavanagh, R. D. Zwicker, and R. K. Schmidt-Ullrich, “The effect of high-dose-rate brachytherapy dwell sequence on cell survival,” *International Journal of Radiation Oncology*Biology*Physics*, vol. 52, pp. 850–857, 2002.
- [4] M. J. Stevens, S. G. Cooper, P. Cross, and Y. Wang, “Accelerated partial breast irradiation using interstitial high dose rate ^{192}Ir brachytherapy: Early australian experience and review of the literature,” *Australasian Radiology*, vol. 50, 2006.
- [5] J. J. Battermann and A. A. Martinez, *Brachytherapy from Radium to Optimization*. Nucletron International, 1994.
- [6] D. M. Shepard, M. C. Ferris, G. H. Olivera, and T. R. Mackie, “Optimizing the delivery of radiation therapy to cancer patients,” *SIAM Rev*, vol. 41, pp. 721–744, 1999.
- [7] M. J. Cazeca, D. C. Medich, and J. J. Munro III, “Effects of breast-air and breast-lung interfaces on the dose rate at the planning target volume of a MammoSite catheter for Yb-169 and Ir-192 HDR sources,” *AAPM*, pp. 4038–4045, 2010.
- [8] F. H. Attix, *Introduction to Radiological Physics and Radiation Dosimetry*. John Wiley & Sons, Inc., 1986.
- [9] J. Duderstadt, *Nuclear Reactor Analysis*. John Wiley & Sons, Inc., 1st ed., 1976.
- [10] P. M. Morse and H. Feshbach, *Methods of Theoretical Physics*. McGraw-Hill, 1953.
- [11] D. G. Duffy, *Green’s Functions with Applications*. Chapman and Hall/CRC, 1st ed., 2001.

- [12] M. D. Greenburg, *Application of Green's functions in science and engineering*. Prentice-Hall, 1971.
- [13] T. Myint-U and L. Debnath, *Linear Partial Differential Equations for Scientists and Engineers*. Birkhauser Boston, 4th ed., 2007.
- [14] J. R. Lamarsh and A. J. Baratta, *Introduction to Nuclear Engineering*. Prentice Hall, 3rd ed., 2001.
- [15] R. D. Evans, *Atomic Nucleus*. Krieger Publishing Company, 1982.
- [16] M. A. Pinsky, *Partial Differential Equations and Boundary-Value Problems with Applications*. Waveland Press, Inc., 3rd ed., 1998.
- [17] M. Itagaki, “Higher order three-dimensional fundamental solutions to the helmholtz and the modified helmholtz equations,” *Engineering Analysis and Boundary Elements*, vol. 15, pp. 289–293, 1995.
- [18] E. N. Economou, *Green's Functions in Quantum Physics*. Springer Berlin Heidelberg, 3rd ed., 2009.
- [19] C. M. Linton, “The green's function for the two-dimensional helmholtz equation in periodic domains,” *Journal of Engineering Mathematics*, pp. 377–402, 1998.
- [20] J. R. Lamarsh, *Introduction to Nuclear Reactor Theory*. American Nuclear Society, 1st ed., 2002.
- [21] M. C. Ferris, “MATLAB and GAMS: Interfacing optimization and visualization software,” Mathematical Programming Technical Report 98-19, Computer Sciences Department, University of Wisconsin-Madison, 1998.
- [22] GAMS Development Corporation, Washington DC, USA, *GAMS-The Solver Manuals*, 2009.
- [23] G. H. Hurlbert, *Linear Optimization: A Simplex Workbook*. Springer, 1st ed., 2009.
- [24] A. A. Mowlavi, F. Cupardo, and M. Severgnini, “Monte Carlo and experimental relative dose determination for iridium-192 source in water phantom,” *Iranian Journal of Radiation Research*, vol. 6, pp. 37–42, 2008.

Appendix A: Green's Functions Derivation

The Green's function solution was explicitly derived for the Dirichlet condition, but the details for the Neumann and Robin (current density) solutions were left out of the previous text. For completeness, the coefficients will be explicitly derived for these two boundary conditions. We will begin with the two-dimensional Neumann condition.

A.1 2-D Neumann Coefficients

Let us start where we left off in the 2-D Green's function chapter. The relationship on the boundary was previously displayed and we will now pursue with the extraction of the coefficients for the Neumann condition. The derivation is as follows:

$$\frac{dg}{dr} = -\frac{dF}{d\rho},$$

$$\frac{dg}{dr}|_{r=R} = \frac{k}{2\pi D} K_1(k\rho(R, \theta; r', \theta')) .$$

Noting that $\frac{dI_0(kr)}{dr} = kI_1(kr)$, A_0 will be the first coefficient to be extracted:

$$\frac{k}{2\pi D} \int_0^{2\pi} K_1(k\rho(R, \theta; r', \theta')) = kI_1(kR) \int_0^{2\pi} A_0 d\theta ,$$

$$\frac{k}{2\pi D} \int_0^{2\pi} K_1(k\rho(R, \theta; r', \theta')) = A_0(2\pi)I_1(kR) ,$$

$$A_0 = \frac{1}{4\pi^2 D I_1(kR)} \int_0^{2\pi} K_1(k\sqrt{R^2 + r'^2 - 2Rr' \cos(\theta - \theta')}) d\theta . \quad (\text{A.1})$$

Next the A_n coefficient is extracted from the boundary condition for $n = 1, 2, \dots, \infty$:

$$\frac{k}{2\pi D} K_1(k\rho(R, \theta; r', \theta')) = \frac{k}{2} [I_{n-1}(kR) + I_{n+1}(kR)] \cdot [A_n \cos n\theta + B_n \sin n\theta] ,$$

$$\frac{1}{\pi D} \int_0^{2\pi} K_1(k\rho(R, \theta; r', \theta')) \cos m\theta d\theta =$$

$$\int_0^{2\pi} [I_{n-1}(kR) + I_{n+1}(kR)] \cdot [A_n \cos n\theta + B_n \sin n\theta] \cos m\theta d\theta ,$$

the above integral $\neq 0$ iff $m = n$,

$$\begin{aligned} \frac{1}{\pi D} \int_0^{2\pi} K_1(k\rho(R, \theta; r', \theta')) \cos m\theta d\theta &= \int_0^{2\pi} [I_{m-1}(kR) + I_{m+1}(kR)] \cdot A_m \cos^2 m\theta d\theta , \\ \frac{1}{\pi D} \int_0^{2\pi} K_1(k\rho(R, \theta; r', \theta')) \cos m\theta d\theta &= A_m \pi [I_{m-1}(kR) + I_{m+1}(kR)] , \\ A_n &= \frac{1}{\pi^2 D [I_{n-1}(kR) + I_{n+1}(kR)]} \int_0^{2\pi} K_1(k\sqrt{R^2 + r'^2 - 2Rr' \cos(\theta - \theta')}) \cos n\theta d\theta . \end{aligned} \tag{A.2}$$

The B_n term will now be solved in a similar fashion. Again, for $n = 1, 2, \dots, \infty$,

$$\begin{aligned} \frac{k}{2\pi D} K_1(k\rho(R, \theta; r', \theta')) &= \frac{k}{2} [I_{n-1}(kR) + I_{n+1}(kR)] \cdot [A_n \cos n\theta + B_n \sin n\theta] , \\ \frac{1}{\pi D} \int_0^{2\pi} K_1(k\rho(R, \theta; r', \theta')) \sin m\theta d\theta &= \\ \int_0^{2\pi} [I_{n-1}(kR) + I_{n+1}(kR)] \cdot [A_n \cos n\theta + B_n \sin n\theta] \sin m\theta d\theta , \end{aligned}$$

the above integral $\neq 0$ iff $m = n$,

$$\begin{aligned} \frac{1}{\pi D} \int_0^{2\pi} K_1(k\rho(R, \theta; r', \theta')) \sin m\theta d\theta &= \int_0^{2\pi} [I_{m-1}(kR) + I_{m+1}(kR)] \cdot B_m \sin^2 m\theta d\theta , \\ \frac{1}{\pi D} \int_0^{2\pi} K_1(k\rho(R, \theta; r', \theta')) \sin m\theta d\theta &= B_m \pi [I_{m-1}(kR) + I_{m+1}(kR)] , \\ B_n &= \frac{1}{\pi^2 D [I_{n-1}(kR) + I_{n+1}(kR)]} \int_0^{2\pi} K_1(k\sqrt{R^2 + r'^2 - 2Rr' \cos(\theta - \theta')}) \sin n\theta d\theta . \end{aligned} \tag{A.3}$$

A.2 2-D Current Density Coefficients

As with the Neumann boundary condition, the coefficients for the current density Green's function solution were not fully derived in the previous text. Here we will pursue a more thorough derivation of these coefficients beginning with the A_0 term. Looking back at the

relationship between the homogeneous and particular solution on the boundary, we have:

$$\begin{aligned}
g + 2D \frac{\partial g}{\partial r} &= \frac{1}{2\pi D} [2Dk K_1(k\rho(R, \theta; r', \theta')) - K_0(k\rho(R, \theta; r', \theta'))] , \\
\frac{1}{2\pi D} \int_0^{2\pi} [2Dk K_1(k\rho(R, \theta; r', \theta')) - K_0(k\rho(R, \theta; r', \theta'))] d\theta &= \\
\int_0^{2\pi} [I_0(kR) + kI_1(kR)] d\theta , \\
A_0 &= \frac{1}{4\pi^2 D [I_0(kR) + k I_1(kR)]} \times \\
\int_0^{2\pi} [2Dk K_1(k\sqrt{R^2 + r'^2 - 2Rr' \cos(\theta - \theta')}) \\
&\quad + K_0(k\sqrt{R^2 + r'^2 - 2Rr' \cos(\theta - \theta')})] d\theta . \tag{A.4}
\end{aligned}$$

Next, we will derive the A_n coefficient for the current density boundary condition:

$$\begin{aligned}
\frac{1}{2\pi D} [2Dk K_1(k\rho(R, \theta; r', \theta')) - K_0(k\rho(R, \theta; r', \theta'))] &= \\
\left\{ I_n(kR) + \frac{k}{2} [I_{n-1}(kR) + I_{n+1}] \right\} [A_n \cos n\theta + B_n \sin n\theta] , \\
\frac{1}{2\pi D} \int_0^{2\pi} [2Dk K_1(k\rho(R, \theta; r', \theta')) - K_0(k\rho(R, \theta; r', \theta'))] \cos m\theta d\theta &= \\
\left\{ I_n(kR) + \frac{k}{2} [I_{n-1}(kR) + I_{n+1}] \right\} \int_0^{2\pi} [A_n \cos n\theta + B_n \sin n\theta] \cos m\theta d\theta ,
\end{aligned}$$

the above integral $\neq 0$ iff $m = n$,

$$\begin{aligned}
\frac{1}{2\pi D} \int_0^{2\pi} [2Dk K_1(k\rho(R, \theta; r', \theta')) - K_0(k\rho(R, \theta; r', \theta'))] \cos m\theta d\theta &= \\
\left\{ I_m(kR) + \frac{k}{2} [I_{m-1}(kR) + I_{m+1}] \right\} \int_0^{2\pi} A_m \cos^2 m\theta d\theta , \\
\frac{1}{2\pi D} \int_0^{2\pi} [2Dk K_1(k\rho(R, \theta; r', \theta')) - K_0(k\rho(R, \theta; r', \theta'))] \cos m\theta d\theta &= \\
\left\{ I_m(kR) + \frac{k}{2} [I_{m-1}(kR) + I_{m+1}] \right\} \int_0^{2\pi} A_m \frac{1}{2} [1 + \cos(2m\theta)] d\theta ,
\end{aligned}$$

$$\begin{aligned}
& \frac{1}{2\pi D} \int_0^{2\pi} [2Dk K_1(k\rho(R, \theta; r', \theta')) - K_0(k\rho(R, \theta; r', \theta'))] \cos m\theta d\theta = \\
& \quad \left\{ I_m(kR) + \frac{k}{2} [I_{m-1}(kR) + I_{m+1}] \right\} A_m \frac{1}{2} \left[\theta + \frac{1}{2m} \sin(2m\theta) \right]_0^{2\pi}, \\
& \frac{1}{2\pi D} \int_0^{2\pi} [2Dk K_1(k\rho(R, \theta; r', \theta')) - K_0(k\rho(R, \theta; r', \theta'))] \cos m\theta d\theta = \\
& \quad \left\{ I_m(kR) + \frac{k}{2} [I_{m-1}(kR) + I_{m+1}] \right\} A_m \frac{1}{2} (2\pi), \\
A_n &= \frac{1}{2\pi^2 D \{ I_n(kR) + \frac{k}{2} [I_{n-1}(kR) + I_{n+1}(kR)] \}} \times \\
&\quad \int_0^{2\pi} [2Dk K_1(k\sqrt{R^2 + r'^2 - 2Rr' \cos(\theta - \theta')}) \\
&\quad + K_0(k\sqrt{R^2 + r'^2 - 2Rr' \cos(\theta - \theta')})] \cos n\theta d\theta. \tag{A.5}
\end{aligned}$$

Similarly for B_n , the derivation uses orthogonality to extract the sine function coefficient:

$$\begin{aligned}
& \frac{1}{2\pi D} \int_0^{2\pi} [2Dk K_1(k\rho(R, \theta; r', \theta')) - K_0(k\rho(R, \theta; r', \theta'))] \cos m\theta d\theta = \\
& \quad \left\{ I_n(kR) + \frac{k}{2} [I_{n-1}(kR) + I_{n+1}] \right\} \int_0^{2\pi} [A_n \cos n\theta + B_n \sin n\theta] \sin m\theta d\theta,
\end{aligned}$$

the above integral $\neq 0$ iff $m = n$,

$$\begin{aligned}
& \frac{1}{2\pi D} \int_0^{2\pi} [2Dk K_1(k\rho(R, \theta; r', \theta')) - K_0(k\rho(R, \theta; r', \theta'))] \cos m\theta d\theta = \\
& \quad \left\{ I_m(kR) + \frac{k}{2} [I_{m-1}(kR) + I_{m+1}] \right\} \int_0^{2\pi} A_m \sin^2 m\theta d\theta,
\end{aligned}$$

and this integral evaluates to the same value as in the A_n derivation yielding:

$$\begin{aligned}
B_n &= \frac{1}{2\pi^2 D \{ I_n(kR) + \frac{k}{2} [I_{n-1}(kR) + I_{n+1}(kR)] \}} \times \\
&\quad \int_0^{2\pi} [2Dk K_1(k\sqrt{R^2 + r'^2 - 2Rr' \cos(\theta - \theta')}) \\
&\quad + K_0(k\sqrt{R^2 + r'^2 - 2Rr' \cos(\theta - \theta')})] \sin n\theta d\theta. \tag{A.6}
\end{aligned}$$

Appendix B: Matlab Code

A Matlab m-file is included to show how MATLAB was used to generate the Green's function solution with numerical integration techniques. Another m-file shows how this data was manipulated to generate the dose matrices and communicate with GAMS optimization models.

B.1 Sample Routine to Get a Flux and Dose Matrix for a Point Source at (r_p, θ_p)

```

clear all;
clc

theta_p =(2*pi)/3; % theta_p is the angle of the point
% source location (radians)
r_p = 2.6; % r_p is the radius of the point source location (cm)
k = 1/11.27; % k=(1/L) where L is the diffusion length (cm)
% for 380 keV photons
D = 4.139; % D is the diffusion coeff (cm)
R = 8; % R is the Outer Radius of the Boundary (cm)

```

```
%-----%
% The Green's Function involves Coefficients A0, An
% and Bn, which need to be solved for using numerical
% integration. This is performed below.
%-----%
```

%----- AO Coefficient -----%

$$c_0 = 1/(4\pi^2 D \cdot (\text{bessel}_0(0, kR) + k \cdot \text{bessel}_1(1, kR)));$$

```
A0 = quadl(@(theta)c_0*(2*D*k*besselk(1,k*...
```

```

sqrt(R^2+r_p^2-2*R*r_p*cos(theta - theta_p)))-...
besselk(0,k*sqrt(R^2+r_p^2-2*R*r_p*cos(theta - theta_p))), 0, 2*pi);

fprintf('A0 is (%d):\n \n', A0)

%----- An & Bn for source @ r_0 and Theta_0 -----%

Q = 15; %quantity for the upper limit of the summation

Integrand_an = zeros(1,Q);
Integrand_bn = zeros(1,Q);

An = zeros(1,Q);
Bn = zeros(1,Q);

for m = 1:Q

c_n = 1/(2*pi^2*D*(besseli(m,k*R)+...
(k/2)*(besseli(m-1,k*R)+besseli(m+1,k*R))));

Integrand_an = @(theta)c_n*cos(m*theta).*(2*D*k*besselk(1,k*...
sqrt(R^2+r_p^2-2*R*r_p*cos(theta - theta_p)))-...
besselk(0,k*sqrt(R^2+r_p^2-2*R*r_p*cos(theta - theta_p))));

Integrand_bn = @(theta)c_n*sin(m*theta).*(2*D*k*besselk(1,k*...
sqrt(R^2+r_p^2-2*R*r_p*cos(theta - theta_p)))-...
besselk(0,k*sqrt(R^2+r_p^2-2*R*r_p*cos(theta - theta_p))));

An(m) = quadgk(Integrand_an, 0, 2*pi, 'MaxIntervalCount', 600000);
Bn(m) = quadgk(Integrand_bn, 0, 2*pi, 'MaxIntervalCount', 600000);

%     fprintf(['A',num2str(m), ' is (%d):\n', num2str(An(m))])
%     fprintf(['B',num2str(m), ' is (%d):\n', num2str(Bn(m))])
end

%-----%
%-----THE FLUX-----%
%-----%
% The integration of the Green's Function times the source distribution

```

```
% yields the flux. For point sources, the source distribution involves
% Dirac delta functions. Using the definition of a delta function, the
% anonymous r_p has been replaced by a specific point source at r_0.
%-----%
r_0 = r_p;
theta_0 = theta_p;

N = 100; % The number of points used for R and Theta
r = linspace(0,R,N);
theta = linspace(-pi,pi,N);

%%%%%%%%%%%%%
%##### The following Loop generates a matrix of
%##### the Flux data for plotting.
%%%%%%%%%%%%%
J_flux1 = zeros(length(theta), length(r));

for i = 1:length(r)
    j = 1;
    while j <= length(theta)
        H=0;
        for m = 1:Q %This allows a series summation with upper limit Q
            H = H + besseli(m, k*r(i))*(A(m)*cos(m*theta(j))+ ...
                B(m)*sin(m*theta(j)));
        end
        J_flux1(j,i) = (1/(2*pi)).*...
            besselk(0,k.*sqrt(r(i).^2+r_0.^2-2.*r(i).*r_0.*...
            cos(theta(j)-theta_0)))+ A0.*besseli(0,k.*r(i))+ H;
        j = j+1;
    end
end
```

```

j = j+1;

end

end

% figure;
% surf(r,theta,flux1)
% fprintf('Flux Matrix is (%d):\n', flux1(:, :))

save J_flux1

[R,TH] = meshgrid(r,theta);
[X,Y] = pol2cart(TH,R);
figure; surf(X,Y,J_flux1);
title(['J_ Flux Distribution from a 10 Ci Point Source Located at'...
'r =' ,num2str(r_p), 'cm and Theta =' ,num2str(theta_p)])
xlabel('x [cm]')
ylabel('y [cm]')
zlabel('Flux [particles*cm^-^2*s^-^1]')

figure;
contourf(X,Y,J_flux1)%[0.02 0.05 0.08]
title(['J_ Isoflux Lines from a 10 Ci Point Source Located at'...
'r =' ,num2str(r_p), 'cm and Theta =' ,num2str(theta_p)])
xlabel('x [cm]')
ylabel('y [cm]')
display(colorbar)

%%%%%%%%%%%%% FLUX CONVERSION TO DOSE DATA %%%%%%%%%%%%%

muen = 0.0326;      %cm^2/g
E = 0.380;          %MeV
C = 1.6022E-10;    %Gy/MeV/g
S_0 = 10*3.7E10;   %s^-1 decays per second for a 10 Ci source

C_tot = muen*E*C*S_0;

T1= 1;    %Dwell time for position 1 in seconds

```

```

J_Dose1= C_tot.*J_flux1.*T1;

figure;
surf(X,Y,J_Dose1)
% title(['J_ Dose Distribution from a 10 Ci Point Source Located at'...
%       'r =' ,num2str(r_p), 'cm and Theta =' ,num2str(theta_p)])
xlabel('x [cm]')
ylabel('y [cm]')
zlabel('Dose [Gy]')
display(colorbar);

figure; contourf(X,Y,J_Dose1)
% title(['J_ IsoDose Lines from a 10 Ci Point Source Located at'...
%       'r =' ,num2str(r_p), 'cm and Theta =' ,num2str(theta_p)])
xlabel('x [cm]')
ylabel('y [cm]')
hcb=colorbar;

```

B.2 Routine to Output Dose Matrices into GAMS Optimization Models

```

%%%%%%%%%%%%%%%
%%%%%%%%%%%%%%%
%%%%%%%%%%%%%%%
%%%%%%%%%%%%%%%
%%%%%%%%%%%%%%%
5-Plane Geometry %%%%%%
%%%%%%%%%%%%%%%
%%%%%%%%%%%%%%%
%%%%%%%%%%%%%%%
%%%%%%%%%%%%%%%
MASTER ROUTINE FOR DWELL TIME OPTIMIZATION %%%%%%
%%%%%%%%%%%%%%%
AND GENERATION OF GDX FILES TO INTERFACE WITH GAMS %
%%%%%%%%%%%%%%%
%%%%%%%%%%%%%%%
BY: JASON HOLZMANN %% MAY 2, 2010 %%%%%%
%%%%%%%%%%%%%%%
%%%%%%%%%%%%%%%
Infinite Catheters: 19 Source Positions %%%%%%

```

```

clc
tic

load J_flux1
load J_flux2
load J_flux3
load J_flux4
load J_flux5

```

```

load J_flux6
load J_flux7
load J_flux8
load J_flux9
load J_flux10
load J_flux11
load J_flux12
load J_flux13
load J_flux14
load J_flux15
load J_flux16
load J_flux17
load J_flux18
load J_flux19

J_flux10(:,1)= 0.2595;

R = 8;
N = 100;
r = linspace(0,R,N);
theta = linspace(-pi,pi,N);

%%%%%%%%%%%%% DATA FOR CONVERSION TO DOSE %%%%%%%%%%%%%%
% muen = 0.190;
muen = 0.0326;    %cm^2/g
E = 0.380;          %MeV
C = 1.6022E-10;    %Gy/MeV/g
S_0 = 10*3.7E10;   %10 Ci and 3.7E10 Bq/Ci

C_tot = muen*E*C*S_0;

%%%%%%%%%%%%% Dwell Times %%%%%%%%%%%%%%
%%%%%%%%%%%%% Optimized Dwell Times %%%%%%%%%%%%%%
%
% T1 = 1;
% T2 = 1;
% T3 = 1;
% T4 = 1;
% T5 = 1;

```

```
% T6 = 1;  
% T7 = 1;  
% T8 = 1;  
% T9 = 1;  
% T10 = 1;  
% T11 = 1;  
% T12 = 1;  
% T13 = 1;  
% T14 = 1;  
% T15 = 1;  
% T16 = 1;  
% T17 = 1;  
% T18 = 1;  
% T19 = 1;
```

```
%%%%%%%%%%%%%% Uniform Dwell Times %%%%%%%%%%%%%%
```

```
T1 = 1;  
T2 = 1;  
T3 = 1;  
T4 = 1;  
T5 = 1;  
T6 = 1;  
T7 = 1;  
T8 = 1;  
T9 = 1;  
T10 = 1;  
T11 = 1;  
T12 = 1;  
T13 = 1;  
T14 = 1;  
T15 = 1;  
T16 = 1;  
T17 = 1;  
T18 = 1;  
T19 = 1;
```

```
%%%%%%%%%%%%% Dose Matrix for Each Infinite Catheter %%%%%%%%%%%%%%
```

```
Dose1 = C_tot.*J_flux1.*T1;  
Dose2 = C_tot.*J_flux2.*T2;  
Dose3 = C_tot.*J_flux3.*T3;
```

```

Dose4 = C_tot.*J_flux4.*T4;
Dose5 = C_tot.*J_flux5.*T5;
Dose6 = C_tot.*J_flux6.*T6;
Dose7 = C_tot.*J_flux7.*T7;
Dose8 = C_tot.*J_flux8.*T8;
Dose9 = C_tot.*J_flux9.*T9;
Dose10 = C_tot.*J_flux10.*T10;
Dose11 = C_tot.*J_flux11.*T11;
Dose12 = C_tot.*J_flux12.*T12;
Dose13 = C_tot.*J_flux13.*T13;
Dose14 = C_tot.*J_flux14.*T14;
Dose15 = C_tot.*J_flux15.*T15;
Dose16 = C_tot.*J_flux16.*T16;
Dose17 = C_tot.*J_flux17.*T17;
Dose18 = C_tot.*J_flux18.*T18;
Dose19 = C_tot.*J_flux19.*T19;

Dose = Dose1 + Dose2 + Dose3 + Dose4 + Dose5 + ...
       Dose6 + Dose7 + Dose8 + Dose9 + Dose10 +...
       Dose11 + Dose12 + Dose13 + Dose14 + Dose15 + ...
       Dose16 + Dose17 + Dose18 + Dose19;

% surf(r,theta,Flux_tot)

[R,TH] = meshgrid(r,theta);
[X,Y] = pol2cart(TH,R);
% figure; surf(X,Y,Flux_tot);
figure; surf(X,Y,Dose);
title('Unoptimized Dose Distribution in Water',...
      'from 19 10-Ci Ir-192 Sources');
xlabel('x [cm]')
ylabel('y [cm]')
zlabel('Dose [Gy]')
display(colorbar);

% figure; contour(X,Y,Flux_tot,[0.35 0.34 0.32 0.30 0.28...
%           0.25 0.22 0.20 0.18 0.16 0.14 0.10 0.02 0.04]);

figure; contourf(X,Y,Dose)
% [0.5 0.75 1 1.25 1.5 1.75 2 2.25 2.5 2.75...
%   3 3.1 3.15 3.2 3.25 3.3 3.35 3.4 3.45 3.5 3.55 3.6]);

```

```
title('Unoptimized Isodose Lines for a Z Axial Slice through Catheters')
xlabel('x [cm]')
ylabel('y [cm]')
hcb = colorbar;

%%%%% GENERATE DOSE MATRICES THAT ARE CAPATIBLE W/ GAMS AND GDX %%%%
F1 = TriScatteredInterp(X(:,Y(:,Dose1(:));
xNew = -8:0.1:8;
yNew = xNew;
[XNEW,YNEW] = meshgrid(xNew,yNew);
DoseNew1 = F1(XNEW,YNEW);

% figure; surf(xNew,yNew,DoseNew1);

F2 = TriScatteredInterp(X(:,Y(:,Dose2(:));
DoseNew2 = F2(XNEW,YNEW);

F3 = TriScatteredInterp(X(:,Y(:,Dose3(:));
DoseNew3 = F3(XNEW,YNEW);

F4 = TriScatteredInterp(X(:,Y(:,Dose4(:));
DoseNew4 = F4(XNEW,YNEW);

F5 = TriScatteredInterp(X(:,Y(:,Dose5(:));
DoseNew5 = F5(XNEW,YNEW);

F6 = TriScatteredInterp(X(:,Y(:,Dose6(:));
DoseNew6 = F6(XNEW,YNEW);

F7 = TriScatteredInterp(X(:,Y(:,Dose7(:));
DoseNew7 = F7(XNEW,YNEW);

F8 = TriScatteredInterp(X(:,Y(:,Dose8(:));
DoseNew8 = F8(XNEW,YNEW);

F9 = TriScatteredInterp(X(:,Y(:,Dose9(:));
DoseNew9 = F9(XNEW,YNEW);

F10 = TriScatteredInterp(X(:,Y(:,Dose10(:));
DoseNew10 = F10(XNEW,YNEW);
```

```

F11 = TriScatteredInterp(X(:,Y(:,Dose11(:));
DoseNew11 = F11(XNEW,YNEW);

F12 = TriScatteredInterp(X(:,Y(:,Dose12(:));
DoseNew12 = F12(XNEW,YNEW);

F13 = TriScatteredInterp(X(:,Y(:,Dose13(:));
DoseNew13 = F13(XNEW,YNEW);

F14 = TriScatteredInterp(X(:,Y(:,Dose14(:));
DoseNew14 = F14(XNEW,YNEW);

F15 = TriScatteredInterp(X(:,Y(:,Dose15(:));
DoseNew15 = F15(XNEW,YNEW);

F16 = TriScatteredInterp(X(:,Y(:,Dose16(:));
DoseNew16 = F16(XNEW,YNEW);

F17 = TriScatteredInterp(X(:,Y(:,Dose17(:));
DoseNew17 = F17(XNEW,YNEW);

F18 = TriScatteredInterp(X(:,Y(:,Dose18(:));
DoseNew18 = F18(XNEW,YNEW);

F19 = TriScatteredInterp(X(:,Y(:,Dose19(:));
DoseNew19 = F19(XNEW,YNEW);

%%%%%% Remove NaN values and replace them with 0 %%%%%%
%%%%%% GAMS doesn't like NaN or undefined values! %%%%
for i=1:161
    for j=1:161
        if isnan(DoseNew1(i,j))
            DoseNew1(i,j) = 0;
        elseif DoseNew1(i,j) < 0;
            DoseNew1(i,j) = 0;
        end
    end
end

for i=1:161
    for j=1:161

```

```
if isnan(DoseNew2(i,j))
    DoseNew2(i,j) = 0;
elseif DoseNew2(i,j) < 0;
    DoseNew2(i,j) = 0;

end
end
end

for i=1:161
    for j=1:161
        if isnan(DoseNew3(i,j))
            DoseNew3(i,j) = 0;
        elseif DoseNew3(i,j) < 0;
            DoseNew3(i,j) = 0;
        end
    end
end

for i=1:161
    for j=1:161
        if isnan(DoseNew4(i,j))
            DoseNew4(i,j) = 0;
        elseif DoseNew4(i,j) < 0;
            DoseNew4(i,j) = 0;
        end
    end
end

for i=1:161
    for j=1:161
        if isnan(DoseNew5(i,j))
            DoseNew5(i,j) = 0;
        elseif DoseNew5(i,j) < 0;
            DoseNew5(i,j) = 0;
        end
    end
end
```

```
for i=1:161
    for j=1:161
        if isnan(DoseNew6(i,j))
            DoseNew6(i,j) = 0;
        elseif DoseNew6(i,j) < 0;
            DoseNew6(i,j) = 0;
        end
    end
end

for i=1:161
    for j=1:161
        if isnan(DoseNew7(i,j))
            DoseNew7(i,j) = 0;
        elseif DoseNew7(i,j) < 0;
            DoseNew7(i,j) = 0;
        end
    end
end

for i=1:161
    for j=1:161
        if isnan(DoseNew8(i,j))
            DoseNew8(i,j) = 0;
        elseif DoseNew8(i,j) < 0;
            DoseNew8(i,j) = 0;
        end
    end
end

for i=1:161
    for j=1:161
        if isnan(DoseNew9(i,j))
            DoseNew9(i,j) = 0;
        elseif DoseNew9(i,j) < 0;
            DoseNew9(i,j) = 0;
        end
    end
end
```

```
end

for i=1:161
    for j=1:161
        if isnan(DoseNew10(i,j))
            DoseNew10(i,j) = 0;
        elseif DoseNew10(i,j) < 0;
            DoseNew10(i,j) = 0;
        end
    end
end

for i=1:161
    for j=1:161
        if isnan(DoseNew11(i,j))
            DoseNew11(i,j) = 0;
        elseif DoseNew11(i,j) < 0;
            DoseNew11(i,j) = 0;
        end
    end
end

for i=1:161
    for j=1:161
        if isnan(DoseNew12(i,j))
            DoseNew12(i,j) = 0;
        elseif DoseNew12(i,j) < 0;
            DoseNew12(i,j) = 0;
        end
    end
end

for i=1:161
    for j=1:161
        if isnan(DoseNew13(i,j))
            DoseNew13(i,j) = 0;
        elseif DoseNew13(i,j) < 0;
            DoseNew13(i,j) = 0;
        end
    end
end
```

```
end

for i=1:161
    for j=1:161
        if isnan(DoseNew14(i,j))
            DoseNew14(i,j) = 0;
        elseif DoseNew14(i,j) < 0;
            DoseNew14(i,j) = 0;
        end
    end
end

for i=1:161
    for j=1:161
        if isnan(DoseNew15(i,j))
            DoseNew15(i,j) = 0;
        elseif DoseNew15(i,j) < 0;
            DoseNew15(i,j) = 0;
        end
    end
end

for i=1:161
    for j=1:161
        if isnan(DoseNew16(i,j))
            DoseNew16(i,j) = 0;
        elseif DoseNew16(i,j) < 0;
            DoseNew16(i,j) = 0;
        end
    end
end

for i=1:161
    for j=1:161
        if isnan(DoseNew17(i,j))
            DoseNew17(i,j) = 0;
        elseif DoseNew17(i,j) < 0;
            DoseNew17(i,j) = 0;
```

```

        end
    end
end

for i=1:161
    for j=1:161
        if isnan(DoseNew18(i,j))
            DoseNew18(i,j) = 0;
        elseif DoseNew18(i,j) < 0;
            DoseNew18(i,j) = 0;
        end
    end
end

for i=1:161
    for j=1:161
        if isnan(DoseNew19(i,j))
            DoseNew19(i,j) = 0;
        elseif DoseNew19(i,j) < 0;
            DoseNew19(i,j) = 0;
        end
    end
end

```

%%%%% GENERATE GDX FILES FOR EACH DOSE DISTRIBUTION FROM EACH SEED %%%%

```

UD1 = full2sp(DoseNew1,'par');
writegdx('dose1.gdx','par','D1',UD1)

```

```

UD2 = full2sp(DoseNew2,'par');
writegdx('dose2.gdx','par','D2',UD2)

```

```

UD3 = full2sp(DoseNew3,'par');
writegdx('dose3.gdx','par','D3',UD3)

```

```

UD4 = full2sp(DoseNew4,'par');
writegdx('dose4.gdx','par','D4',UD4)

```

```
UD5 = full2sp(DoseNew5,'par');
write.gdx('dose5.gdx','par','D5',UD5)

UD6 = full2sp(DoseNew6,'par');
write.gdx('dose6.gdx','par','D6',UD6)

UD7 = full2sp(DoseNew7,'par');
write.gdx('dose7.gdx','par','D7',UD7)

UD8 = full2sp(DoseNew8,'par');
write.gdx('dose8.gdx','par','D8',UD8)

UD9 = full2sp(DoseNew9,'par');
write.gdx('dose9.gdx','par','D9',UD9)

UD10 = full2sp(DoseNew10,'par');
write.gdx('dose10.gdx','par','D10',UD10)

UD11 = full2sp(DoseNew11,'par');
write.gdx('dose11.gdx','par','D11',UD11)

UD12 = full2sp(DoseNew12,'par');
write.gdx('dose12.gdx','par','D12',UD12)

UD13 = full2sp(DoseNew13,'par');
write.gdx('dose13.gdx','par','D13',UD13)

UD14 = full2sp(DoseNew14,'par');
write.gdx('dose14.gdx','par','D14',UD14)

UD15 = full2sp(DoseNew15,'par');
write.gdx('dose15.gdx','par','D15',UD15)

UD16 = full2sp(DoseNew16,'par');
write.gdx('dose16.gdx','par','D16',UD16)

UD17 = full2sp(DoseNew17,'par');
write.gdx('dose17.gdx','par','D17',UD17)

UD18 = full2sp(DoseNew18,'par');
write.gdx('dose18.gdx','par','D18',UD18)
```

```

UD19 = full2sp(DoseNew19,'par');
writedex('dose19.gdx','par','D19',UD19)

%
% [Dt]=gams('DwellV3.gms');
% Dt.val;
% surf(xNew,yNew,Dt.val)

%%%%%%%%%%%%% GENERATE GDX FILE FOR PRESCRIBED DOSE %%%%%%%%
PrescrDose = 3.4.*ones(161,161);
DoseP = full2sp(PrescrDose,'par');
writedex('DoseP.gdx','par','Dp',DoseP)

%%%%%%%%%%% Create circle to outline PTV %%%%%%%%
rho = 2.5;    %Radius of PTV
xPTV = rho.*cos(theta);  %x values for circle
yPTV = rho.*sin(theta);  %y values for circle

%%%%%%%%%%% Generate Plots for each Linear Program Model 1 thru 4 %%%%%%%
##### LP #1#####
%Dose Distribution
[PTV1, TPTV1]=gams('Five_Plane_PTV_LP1.gms');
figure; surf(xNew,yNew,PTV1.val);
title('Dose Distribution Optimized by LP1 for 19 Catheters',...
      'with 10 Ci Ir-192 Brachytherapy Sources');
xlabel('x [cm]')
ylabel('y [cm]')
zlabel('Dose [Gy]')
display(colorbar);

%IsoDose Plot
figure;
contourf(xNew,yNew,PTV1.val,...)
[0,0.5,1,1.5,2,2.38,2.72,3.06,3.4,3.74,4.08,4.42,4.76,5.1,6.8])
hold on
plot(xPTV,yPTV,'w-', 'LineWidth', 2.5)

```

```

annotation('textbox',[.40,.4,0.09,0.065],'String','PTV','color','w',...
    , 'FontSize',14,'LineStyle','none')
title('IsoDose Lines from LP1');
xlabel('x [cm]')
ylabel('y [cm]')
zlabel('Dose [Gy]')
display(colorbar);
hold off

#####
##### LP #2
#####
%Dose Distribution
[PTV2, TPTV2]=gams('Five_Plane_PTV_LP2.gms');
figure; surf(xNew,yNew,PTV2.val);
title('Dose Distribution Optimized by LP2 for 19 Catheters',...
    'with 10 Ci Ir-192 Brachytherapy Sources');
xlabel('x [cm]')
ylabel('y [cm]')
zlabel('Dose [Gy]')
display(colorbar);

%IsoDose Plot
figure;
contourf(xNew,yNew,PTV2.val,...)
    [0,0.5,1,1.5,2,2.38,2.72,3.06,3.4,3.74,4.08,4.42,4.76,5.1,6.8])
hold on
plot(xPTV,yPTV,'w-','LineWidth', 2.5)
annotation('textbox',[.40,.4,0.09,0.065],'String','PTV','color','w',...
    , 'FontSize',14,'LineStyle','none')
title('IsoDose Lines from LP2');
xlabel('x [cm]')
ylabel('y [cm]')
zlabel('Dose [Gy]')
display(colorbar);
hold off

#####
##### LP #3
#####
%Dose Distribution
[PTV3, TPTV3]=gams('Five_Plane_PTV_LP3.gms');

```

```

figure; surf(xNew,yNew,PTV3.val);
title('Dose Distribution Optimized by LP3 for 19 Catheters',...
      'with 10 Ci Ir-192 Brachytherapy Sources');
xlabel('x [cm]')
ylabel('y [cm]')
zlabel('Dose [Gy]')
display(colorbar);

%IsoDose Plot
figure;
contourf(xNew,yNew,PTV3.val,...[0,0.5,1,1.5,2,2.38,2.72,3.06,3.4,3.74,4.08,4.42,4.76,5.1,6.8])
hold on
plot(xPTV,yPTV,'w-','LineWidth', 2.5)
annotation('textbox',[.40,.4,0.09,0.065],'String','PTV','color','w',...
           'FontSize',14,'LineStyle','none')
title('IsoDose Lines from LP3');
xlabel('x [cm]')
ylabel('y [cm]')
zlabel('Dose [Gy]')
display(colorbar);
hold off

#####
##### LP #4
#####
%Dose Distribution
[PTV4, TPTV4]=gams('Five_Plane_PTV_LP4.gms');
figure; surf(xNew,yNew,PTV4.val);
title('Dose Distribution Optimized by LP4 for 19 Catheters',...
      'with 10 Ci Ir-192 Brachytherapy Sources');
xlabel('x [cm]')
ylabel('y [cm]')
zlabel('Dose [Gy]')
display(colorbar);

%IsoDose Plot
figure;
contourf(xNew,yNew,PTV4.val,...[0,0.5,1,1.5,2,2.38,2.72,3.06,3.4,3.74,4.08,4.42,4.76,5.1,6.8])
hold on
plot(xPTV,yPTV,'w-','LineWidth', 2.5)

```



```
xlabel('x [cm]')
ylabel('y [cm]')
zlabel('Dose [Gy]')
display(colorbar);
```

```
toc
```